Concepts and Technology Development for the Autonomous Assembly and Reconfiguration of Modular Space Systems

by

Lennon Patrick Rodgers

B.S. Mechanical Engineering
University of Illinois at Urbana-Champaign, 2003

Submitted to the Department of Mechanical Engineering
in partial fulfillment of the requirements for the degree of

Master of Science in Mechanical Engineering
at the
Massachusetts Institute of Technology

February 2006

Signature of Author: _____
Department of Mechanical Engineering
December 20, 2005

Certified by: _____
David W. Miller
Professor of Aeronautics and Astronautics
Thesis Advisor

Accepted by: _____
Warren Seering
Professor of Mechanical Engineering
Thesis Reader

Accepted by: _____
Lallit Anand
Professor of Mechanical Engineering
Chairman, Committee on Graduate Students

Concepts and Technology Development for the Autonomous Assembly and Reconfiguration of Modular Space Systems

by

Lennon Patrick Rodgers

Submitted to the Department of Mechanical Engineering on December 20, 2005, in partial fulfillment of the requirements for the degree of Master of Science

Abstract:

This thesis will present concepts of modular space systems, including definitions and specific examples of how modularity has been incorporated into past and present space missions. In addition, it will present two architectures that utilize modularity in more detail to serve as examples of possible applications.

The first example is a fully modular spacecraft design, which has standardized and reconfigurable components with multiple decoupled subsystems. This concept was developed into a testbed called Self-assembling Wireless Autonomous and Reconfigurable Modules (SWARM). This project sought to demonstrate the use of modular spacecraft in a laboratory environment, and to investigate the "cost," or penalty, of modularity.

The second example investigates the on-orbit assembly of a segmented primary mirror, which is part of a large space-based telescope. The objective is to compare two methods for assembling the mirror. The first method uses a propellant-based spacecraft to move the segments from a central stowage stack to the mirror assembly. The second is an electromagnetic-based method that uses superconducting electromagnetic coils as a means of applying force and torque between two assembling vehicles to produce the same results as the propellant-based system.

Fully modular systems could have the ability to autonomously assemble and reconfigure in space. This ability will certainly involve very complex rendezvous and docking maneuvers that will require advanced docking ports and sensors. To this end, this thesis investigates the history of docking ports, and presents a comprehensive list of functional requirements. It then describes the design and implementation of the Universal Docking Port (UDP). Lastly, it explores the development of an optical docking sensor called the Miniature Video Docking Sensor (MVDS), which uses a set of infrared LED's, a miniature CCD-based video camera, and an Extended Kalman Filter to determine the six relative degrees of freedom of two docking vehicles. It uses the Synchronized Position Hold Engage and Reorient Experimental Satellites (SPHERES) to demonstrate this fully integrated docking system.

Thesis Advisor: David W. Miller
Title: Associate Professor of Aeronautics and Astronautics, MIT

Acknowledgments

This work was supported by Lockheed Martin (Advanced Technology Center) under the Autonomous Assembly and Reconfiguration Contract 8100000177, and by the Jet Propulsion Laboratory under Contract NNG05GB23G.

There were many individuals who heavily contributed to this body of work. Umair Ahsun (MIT) developed the EMFF optimization routine mentioned in Section 2.3.4. Fredrik Rehnmark (Lockheed Martin) helped greatly with the docking port capabilities discussed in Section 3.2, and also provided a valuable list of docking port references. Nick Hoff, Elizabeth Jordan, James Modisette, Amy Brzezinksi and Todd Billings (all from MIT) were instrumental in the UDP design and fabrication as discussed in Section 3.4. Paul Bauer (MIT) provided an unlimited amount of time and expertise for the development of the UDP and MVDS. Simon Nolet (MIT) helped with the Extended Kalman Filter derived in Section 4.3.2, and also with the UDP and MVDS tests. He also designed and built the UDP circuit boards. Simon deserves a lot of credit for his many contributions. Warren Seering has served as my departmental advisor, and I am grateful for his flexibility and help with this thesis. Lastly, David Miller (MIT) has been a loyal and supportive primary advisor, and has provided technical direction for this entire thesis. I am grateful to these individuals for both their friendship and technical support.

I would like to thank the engineering managers and mentors I have had over the years: Dirk Rodgers (PCC), Don Gnaedinger (Eagle Automation), Tim Clemens (GE), Phil Beauchamp (GE), Dave Henderson (GE), Mark Swain (JPL), Mark Colavita (JPL), Leon Gefert (NASA), Les Balkanyi (NASA), Ray Sedwick (MIT) and Marc Lane (JPL).

Lastly, I am extremely grateful to my family for providing encouragement and inspiration: Rick, Teri, Charity, Carolyn, Joanna, Thomas, Keenan, Ela and Seth.

Table of Contents

List of Figures

List of Tables

Nomenclature

AAR	Autonomous Assembly and Reconfiguration
EKF	Extended Kalman Filter
EM	Electromagnet
EMFF	Electromagnetic Formation Flight
ISS	International Space Station
MIT	Massachusetts Institute of Technology
MVDS	Miniature Video Docking Sensor
SPHERES	Synchronized Position Hold Engage and Reorient Experimental Satellites
SPHERE	Same as SPHERES
SSL	Space Systems Laboratory
SWARM	Self Assembling Wireless Autonomously Reconfigurable Modules
UDP	Universal Docking Port

Mathematical Notation

Vectors and matrices are represented in bold italic (e.g. $\boldsymbol{x}$)

Scalars are represented in italics (e.g. x)

${}^{A}\boldsymbol{X}$ is a vector X in the A coordinate frame.

X_b is the scalar component of a vector **X** in the b-coordinate direction.

$\boldsymbol{X}^t$ is the transpose of **X.**

Chapter 1. Introduction

1.1. Motivation

The exploration of space has continually demanded larger and more complex space systems. The size of such space systems, however, is significantly limited by launch vehicle costs and payload carrying capabilities, while risk management and allowable development time greatly limit the complexity of their design. Thus, it is critical to focus on size and complexity when considering new methods for designing advanced space systems. A modular design methodology would be achieved if a space system were physically divided by separate functions. For instance, a conventional spacecraft consists of multiple subsystems such as propulsion, thermal, attitude control and payload, which are all integrated to form a monolithic system. A modular spacecraft performs the same functions, but each subsystem forms a separate module, which acts independently except through the connections available through one or more standardized interfaces. Using multiple launches, each of these modules could be autonomously assembled with previously launched modules to form a very large system once in space.

A modular space system with the ability to autonomously assemble and reconfigure itself while in space would increase the lifetime of the spacecraft by providing the option of replacing only particular failed subsystems after years of operation. Also, certain system architectures could benefit from the ability to reconfigure. Finally, since each separate module could be designed and tested independently, modularity could reduce the amount of time required for design, manufacturing, integration and testing. Thus, a modular design could be used to increase the size and complexity of a space system.

1.2. Overview

Chapter 2 presents concepts of modular space systems, and includes definitions and specific examples of how modularity has been incorporated into past and present space missions. In addition, two space system architectures that utilize modularity are presented in more detail to serve as examples of possible applications. Analyses are performed to investigate a few of the first order complexities involved with these particular modular concepts. The first example is a fully modular spacecraft design, which has standardized and reconfigurable components with multiple decoupled subsystems. This concept was developed into a testbed called Self-assembling Wireless Autonomous and Reconfigurable Modules (SWARM), which sought to demonstrate the use of modular spacecraft in a laboratory environment, and to investigate the "cost," or penalty of modularity.

The second example investigates the on-orbit assembly of a large segmented primary mirror, which is part of a space-based telescope. The objective is to compare two methods for assembling the mirror. The first method uses a propellant-based spacecraft to move the segments from a central stowage stack to a mirror assembly. The second is an electromagnetic-based method that uses superconducting electromagnetic coils as a means of applying force and torque between two assembling vehicles to produce the same results as the propellant-based system. This system is termed Electromagnetic Formation Flight (EMFF). Since only electrical energy, which is abundant through the use of solar panels, is required, the number of maneuvers necessary to assemble the mirror becomes less limited by fuel availability. Moreover, optical contamination due to the exhausts of the thruster-based systems is not an issue with EMFF. Although this telescope is not a completely modular system, it demonstrates the concept of assembling and possibly reconfiguring a large number of modules in space.

The autonomous assembly and reconfiguration (AAR) of any modular space system will involve very complex rendezvous and docking maneuvers, which will certainly require advancements in docking port and sensor technology. To this end, the history of docking ports is presented in Chapter 3, and a comprehensive list of functional requirements is developed. Also, the design and implementation of a universal docking

port is shown. This docking port has an androgynous design capable of passing mechanical and electrical loads between the connected modules. It is also universal, since any two identical ports can be connected together. Supporting electronics allow for both local and remote computer control of the docking port.

Lastly, Chapter 4 discusses the development of a docking sensor. This optical sensor is called the Miniature Video Docking Sensor (MVDS), and uses a set of infrared LED's, a miniature CCD-based video camera, and an Extended Kalman Filter to determine the six relative degrees of freedom of two docking vehicles. The Synchronized Position Hold Engage and Reorient Experimental Satellites (SPHERES), which were also developed by the MIT Space Systems Laboratory, were used to demonstrate the fully integrated docking port and sensor system. Thus, one of the major objectives of this thesis is to present the general requirements for autonomous docking ports and sensing systems, the design of such systems, and the results from 2-D laboratory experiments.

1.3. Outline

- Section 2.1 discusses general concepts of modularity, and offers examples of how modularity has been incorporated into past and present space missions.

- Section 2.2 presents the development of a ground-based testbed, which sought to demonstrate the use of modular spacecraft in a laboratory environment and to investigate the "cost" of modularity.

- Section 2.3 analyzes two different methods for assembling a large segmented mirror in space as an example of how modularity could be incorporated into spacecraft design.

- Section 3.1 briefly describes the history of docking ports and lists docking port capabilities for unmanned missions where docking is needed to assemble modular space systems.

- Section 3.4 uses the previously defined docking port capabilities to explain the design and development of a miniature universal docking port.

- Chapter 4 discusses the development of an optical sensor that provides the relative state estimation of two vehicles during docking. It discusses the results from ground-based tests, which demonstrated an autonomous docking maneuver using a micro-satellite and the fully integrated docking port and sensing system.

- Chapter 5 summarizes the results from this thesis and offers suggestions for future work.

Chapter 2. Concepts of Modularity in Spacecraft Design

A module is defined as an encapsulation of highly interconnected parts, whose external connections are minimized and simple. This chapter will discuss some general concepts of modularity currently being considered and used in spacecraft design. It will also present a brief history of past and present work in the area of modular spacecraft including technology that was developed as part of MIT's modular spacecraft testbed. Lastly, a trade model comparing two different methods for autonomously assembling a modular telescope will be presented.

2.1. Past and Present Work

A modular spacecraft design (MSD) has standardized and reconfigurable components with multiple decoupled subsystems. It also has the ability to reuse these common modules across separate missions. This is in contrast with a common spacecraft design (CSD), which involves using identical but non-reconfigurable designs, or a heritage spacecraft design (HSD), which is heavily based upon previous designs. A modular spacecraft design holds promise for reducing the amount of time required for design, manufacturing, integration and testing.

The commercial, military and science communities would directly benefit from modular designs by having the option of replacing only particular subsystems of a spacecraft. For example, a failed propulsion subsystem could be replaced on orbit instead of the entire spacecraft. Another benefit of a modular design is the ability to launch large spacecraft using one or more launches. Once in space, the modules could be autonomously deployed and assembled. The spacecraft could then be reconfigured to accommodate various mission objectives. Lastly, standardization gives rise to compatibility across

organizations and allows for more domestic and international collaboration. As space technology advances, there is a need for standardization and modularity if space technology is to follow a similar path as other successfully advanced technologies such as automobiles, aircraft and electronics.

However, the major drawback with a modular spacecraft design is the need for each subsystem to function independently except through the connections available through one or more interfaces (docking ports). Because of this, the modular design will most likely be sub-optimal and performance may be sacrificed.

Past Work

An early pioneer of a common and heritage spacecraft designs was the Multi-mission Modular Spacecraft (MMS), which was developed by NASA's Goddard Space Flight Center [1]. The MMS was established in the 1970s, and consisted of the following *earth-orbiting* missions:

- Landsat 4 and 5
- The Ocean Topography Experiment (TOPEX/Poseidon)
- Upper Atmospheric Research Satellite (UARS)
- Extreme Ultraviolet Explorer (EUVE)
- Solar Maximum Mission (SMM)

The MMS was part of NASA's pre-Challenger-disaster vision for satellite servicing. The MMS had the following modules:

- Propulsion
- Power
- Attitude control
- Command and data handling
- Other sub-modules to provide signal conditioning and support for an Earth horizon sensor

Mariner Mark II was NASA's planned family of unmanned spacecraft for the exploration of the outer solar system that were to be developed and operated by NASA's Jet Propulsion Laboratory between 1990 and 2010. Mariner Mark II was intended to be the deep space version of the MMS, which was proven to be very successful for earth orbital missions. Using the same concepts of a standard bus and modular equipment, JPL hoped to cut mission costs in half [2].

The first two Mariner Mark II applications were to be a mission to Saturn and its moon Titan, the Saturn Orbiter/Titan Probe, or SOTP (later called Cassini) and the Comet Rendezvous Asteroid Flyby, or CRAF. Congress approved both of these missions in 1990. Other planned Mariner Mark II based spacecraft included the European mission called the Comet Nucleus Sample Return or CNSR (later Rosetta). However, Congressionally imposed budget cuts forced NASA to terminate the CRAF mission and to delay the Cassini launch. They were also forced to significantly redesign Cassini to reduce the total program cost, mass and power requirements. In essence, the spirit of Mariner Mark II, and the use of modular spacecraft for deep space were terminated due to budget cuts. This shows that the upfront cost of modularity makes it very susceptible to budget cuts when short-term savings drives decisions.

Present Work

Much of the present work focuses on defining the capabilities and major complexities with designing modular spacecraft. The complexity of modular designs largely depends on the capabilities and quantity of docking ports required for a particular mission. A trade was done by Moynahan and Touhy [3], which concluded that the docking port for a modular spacecraft should provide the following connections between modules:

- Data/communication
- Mechanical
- Electrical

They also concluded that the thermal system should be left as a function for each individual module to manage, and thus should not be part of the docking port. This issue of

defining the actual interface between modules is difficult, and would likely be reconsidered for each mission.

More recent effort to develop concepts of modularity in spacecraft design include the following projects and missions:

Name: Small, Smart Spacecraft for Observation and Utility Tasks (SCOUT)
Collaborators: DARPA, Aero/Astro Inc.
Description: A multi-mission, rapidly configurable micro-satellite to enable responsive deployment of tactical capability to orbit [4].

Name: The Flexible and Extensible Bus for Small Satellite (FEBSS)
Collaborators: Air Force Research Laboratory, Aero/Astro Inc.
Description: A low-cost, modular bus for small satellites [4].

Name: Panel Extension Satellite (PESAT)
Collaborators: University of Tokyo
Description: A satellite made of several functional panels, including a computer, battery, communication, attitude control and thruster panels. Panels are connected in a "plug-in" fashion, and the total integrated system acts as a conventional satellite. The panels will be stowed during launch within a small volume and then extended on orbit with hinge and latch mechanisms [5].

To summarize, modular technology was successfully demonstrated in MMS missions, though it has been removed from some subsequent missions due to budget cuts. Most of the present work focuses on the interfaces between modules, and how the modules should be integrated to form a complete system. The next section will discuss the modular spacecraft technology that was developed as part of the SWARM project.

2.2. Modular Technology Development with SWARM

SWARM stands for Self-assembling Wireless Autonomous and Reconfigurable Modules (Figure 2-1). The project sought to demonstrate the use of modular spacecraft in a laboratory environment, and to investigate the "cost," or penalty of modularity. While the lab prototypes closely resemble an actual space system, they were not designed for the space environment. The SWARM system consists of the following separate modules (the quantity is in parenthesis):

- Computer (1)
- Attitude Control System (ACS) (1)
- Propulsion (2)
- Mothership (1)

Each module performs a set of subsystem functions and is supported by the following common components (the quantity is in parenthesis):

- Structural package/containment (1)
- Power supply and distribution bus (1)
- Bluetooth chip for wireless command and data handling (1)
- Field programmable gate array (computer) (1)
- Metrology sensors (4 sets)
- Docking port (up to 4)

The computer module is the central processor, and gives commands wirelessly to the local computer on each module using the standard Bluetooth® protocol. A laptop is currently used as the computer module. By using wireless communication, the modules are able to communicate in both docked and formation flown architectures. The ACS module provides rotational torque and is capable of storing angular momentum for the entire spacecraft. This module is essentially a motorized flywheel with a gyro and

microprocessor that are used to perform all local sensing and low-level commands. The ACS module receives a commanded change in angle from the computer module, and by integrating the on-board rate gyro, executes the command by applying torque against the flywheel. The propulsion module provides the thrust for rotation and translation. Each propulsion module has a firing circuit and six thrusters, which use a supply tank of liquid CO_2 and a pressure regulator. This module converts thrust commands into a series of firing circuit on-times via a pulse width modulation scheme. The Mothership module acts as a much larger vehicle that provides electrical power for charging. It is essentially a rigid post with all of the common components previously mentioned except for the structural packaging. The Mothership is connected to a wall outlet, which provides a continual supply of electrical power for charging once the modules are docked.

The ACS and propulsion modules are mounted on air-carriages and float on a flat surface (Figure 2-2). For simplicity, the Mothership and computer modules are stationary and not contained within the standard module packaging.

As previously stated, a module is defined as an encapsulation of highly interconnected parts, whose external connections are minimized and simple. For SWARM, the structural packaging is the encapsulation, while the docking port and Bluetooth provide the simple external connections.

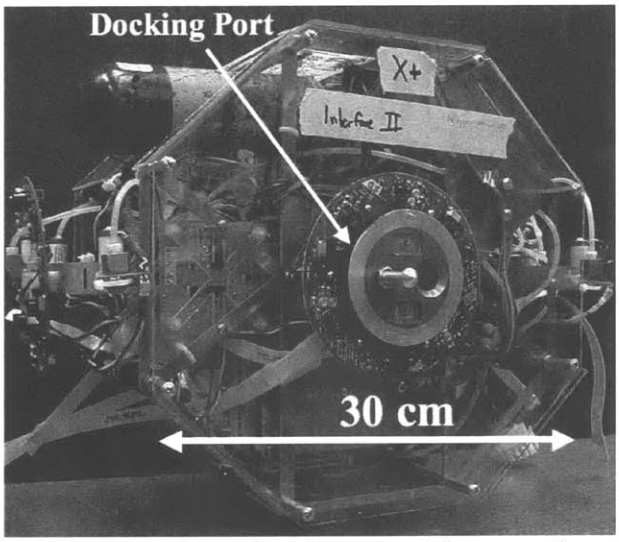

Figure 2-1: A SWARM Module with a docking port. The metrology sensors are mounted around the docking port.

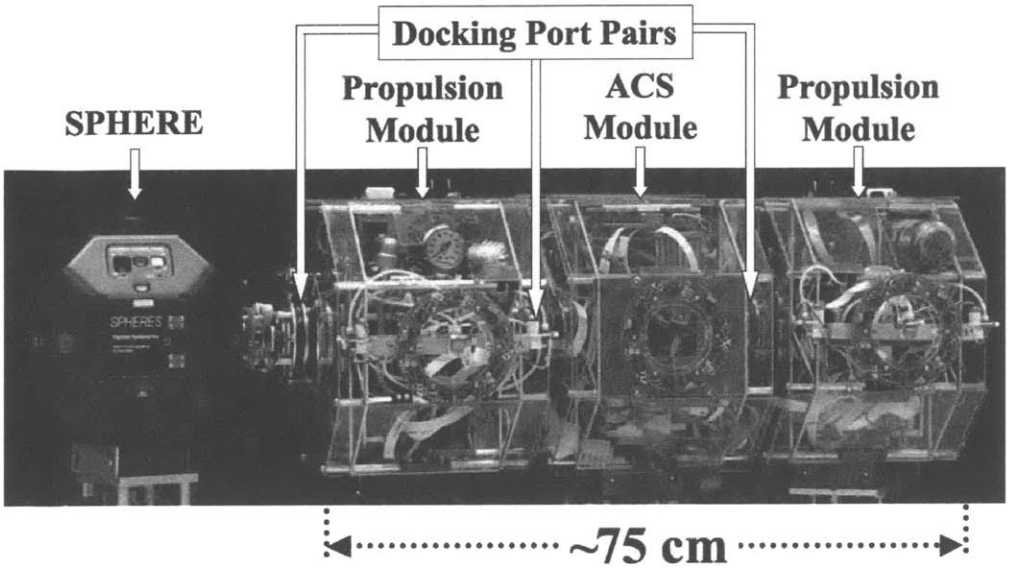

Figure 2-2: A SPHERE [6], two propulsion modules and an ACS module, sitting on air-carriages and rigidly connected using the docking port.

2.2.1. Overview of the docking port

The docking port is a critical piece of the SWARM design. Each module must function independently except through the connections available through this interface and the Bluetooth communication. The SWARM docking port must be capable of performing the following functions between each module:

- **Autonomously Dock/Undock:** This provides the ability for the modules to be assembled and reconfigured without human intervention.

- **Transfer Mechanical Loads:** By mechanically connecting the modules, separate propulsion and ACS modules are able to control the translation and rotation of the entire module cluster.

- **Transfer Electrical Power:** This allows the modules to share electrical power. For example, the Mothership can charge the other modules.

- **Provide a Connection for Data and Communication:** Communication between modules is necessary for docking/undocking, transferring range data, and general system control.

Section 3.4 will give a detailed description of the SWARM docking port.

2.2.2. Wireless communication using Bluetooth

SWARM uses wireless communication because it offers many practical advantages when compared to a wired system [7]. Wireless communication is inherently complementary to a modular system, since it provides a communication link between separated modules. System-level integration and reconfiguration of the modules will be easier by eliminating the need for a wired connection between docking ports. Also, wireless communication removes mass while increasing the available volumetric space by eliminating the presence of physical wiring. Lastly, it provides real-time communication, and reduces electromagnetic interference (EMI) by eliminating some of the EMI-producing components. However, wireless technology is still under development for space applications, and there are clear disadvantages to choosing this option. For example, radiation in the space environment could cause interference with wireless data transmission. Also, wireless communication generates electromagnetic radiation (EMR). This could be a potential problem for sensitive payloads that are susceptible to this form of radiation. There is also a chance that wireless communication will produce higher development costs due to the complexity of the hardware and software.

Bluetooth is the wireless communications system chosen for SWARM, mainly because of its low cost and standardized architecture. A Bluetooth chip is on the common circuit board, of which every module has identical copies. This chip is the BR-SC11A 18-pin STAMP module from Blueradios [8]. This was chosen because of its low cost ($50 per chip) as well as low power consumption (0.35W). The main computer uses a Bluetooth USB dongle to communicate on the SWARM network. The dongle contains the same basic chip but with a modified enclosure and connection interface.

All of the communication is routed through the main computer module, which forms a master-slave architecture. This takes advantage of the piconet structure of Bluetooth. A piconet is defined as a single master and up to 7 slaves, which is sufficient for the initial SWARM testing. However, future modular systems will likely require more slave modules, and thus Bluetooth's scatternets structure will be required. Scatternets are combinations of piconets joined through one or more slave modules existing in both networks. This would allow additional "parked" slaves to exist in a low-power consumption mode for increased overall network size. According to Bluetooth specifications, up to 255 "parked" slaves could be on the scatternet [9].

One of the biggest challenges in implementing a wireless network is the error checking and correction. The difficulty is caused by bit corruption in the wireless network, which is mainly caused by radio interference. Bluetooth minimizes this interference by using a built-in spread-spectrum frequency error checking technique. This technique synchronizes up to 1600 hops per second between communicating master and slave modules. This significantly reduces the amount of interference encountered by the transmissions. Bluetooth also employs a variable system of data packet checking and reception acknowledgement to ensure accurate data transmission. Depending on the configuration used for a transmission as well as the level of outside interference, the error-checking system could influence the maximum achievable bandwidth. There are three kinds of error correction schemes used in the baseband protocol of Bluetooth: 1/3-rate Forward Error Correction (FEC), 2/3-rate FEC and Acknowledgement Request Repeat (ARQ) configuration. In 1/3-rate FEC, every bit is repeated three times for redundancy. In 2/3-rate FEC, a generator polynomial is used to encode 10-bit code to a 15-bit code. In the ARQ configuration, DM (Medium-Rate Data) and DH (High-Rate Data) packets are retransmitted until an acknowledgement is received (or timeout is exceeded). Automatic Repeat reQuest Numbers (AQRN) are used as a 1-bit acknowledgement indication to inform the source of a successful transfer of payload data with cyclic redundancy checking. Bluetooth uses fast, unnumbered acknowledgement in which it uses positive and negative acknowledgements by setting appropriate ARQ values. If the timeout value is exceeded, Bluetooth flushes the packet and proceeds with the next.

A very important component of the wireless system is the protocol used for communication between the computer and any other module. This protocol must include all necessary commands for system operation as well as the data structure that will contain the relevant information. Each transmission to or from the computer module will have both header and data bytes. This form only includes the information being sent to or from the computer. All the error checking is part of the internal header structure and is handled entirely by Bluetooth. Each of the present headers contains three bytes of information consisting of the following items:

- 3-bit Origin ID: Source of the transmission
- 3-bit Destination ID: Desired destination of the transmission
- 4-bit Command: Value of the command being sent to the destination module
- 10-bit Data Length: Number of bytes contained in the data portion of the transmission

The data portion of the transmission will contain the information for the actual command. Currently, each communications packet can contain up to 1023 bytes of information. Table 2-1 contains a few examples of commands from the computer to the modules.

Table 2-1: Some sample commands from the computer to the modules.

Origin ID	Destination ID	Command	Description	Explanation	Data Bytes
000	010	001	Thrusters On	Turns on the desired thruster for a propulsion module.	Each thruster command can have 3-18 bytes, depending on the number of thrusters
000	010	0010	Constant speed rotation	Rotates the ACS module at a specified speed in a specified amount of time.	2 bytes to input the speed and time.
000	010	0011	Smooth trajectory	Rotates the ACS a specified angle.	2 bytes to input the angle and time.

Most of this information on wireless communication was taken from the SWARM design document [7].

2.2.3. Determining the cost of modularity

If the actual "cost" of modularity is well understood in terms of metrics such as mass and development costs, then a modular design could be successfully implemented for missions that would benefit from such a design. However, determining the absolute cost of modularity is very difficult. Enright, Jilla and Miller [10] sought to determine mission scenarios for when a modular design might be appropriate based on possible cost savings, when compared with an equivalent non-modular design. They concluded that modularity could offer cost savings for missions involving a small number of satellites when the design is driving the mission cost. However, as the mission size increases, the mass and launch costs increase greatly. Thus a lighter custom (non-modular) design may yield better price performance. They also concluded that modular designs in two ranges of mission size offer large savings when production costs are dominant. The first region covers very small missions (few satellites), where the initial learning curve savings are dominant. The second includes modest sized missions (about a dozen spacecraft), where the design and secondary learning curves savings allow large savings (regions with high learning curve factors). Thus, they concluded that the size and complexity of the mission largely dictate the cost savings of modularity.

Instead of determining whether or not modularity is appropriate for a given mission, SWARM was analyzed to determine the relative cost of modularity. This is a qualitative measure of the penalty induced by having a modular design. The relative cost determines which components most heavily penalized the design by adding size, mass and complexity. The common components in SWARM were grouped together and rated based on a set of penalty metrics. The following groups of components were considered:

1. **Structural packaging:** The additional packaging that is required to separate the various subsystems into their own structurally rigid containment. It is the "encapsulation," which is part of the definition of a module as previously stated. In the case of SWARM, this is the metal structure used to enclose the propulsion and ACS modules.

2. **Docking port and sensors:** The docking port is the only physical connection between modules. The sensors allow the modules to dock and undock for reconfiguration maneuvers.

3. **Electronics/cabling:** All the electronic components that are common among modules. This includes the FPGA, power distribution card and Bluetooth chip, and all the necessary cables.

The following penalty metrics were used to rate each of the groups:

1. **Volume:** Measures the volumetric space occupied by the component. Components that occupy a large volume are penalized with a high rating.

2. **Mass:** Measures the significance of the mass added by this group. If the mass is relatively significant, then it is penalized with a high rating.

3. **Complexity:** Measures the added complexity in the spacecraft design by having this component. If the component was very complex to design, then it is penalized with a high rating.

4. **Non-scalability:** Measures the scalability of the group. Can it be shrunk in size for smaller modules and increased in size for larger modules? If the component cannot be easily scaled, this is bad for modularity and thus is penalized with a high non-scalability rating.

Each group is given a relative metric rating from 1 to 3 (1 = low, 3 = high). Each metric has a "weight" based on its significance to the overall design. The results of this analysis can be found in Table 2-2.

Table 2-2: The metrics used to determine the relative costs of modularity.

SWARM Component	*Metrics*				
	Volume	**Mass**	**Complexity**	**Non-scalability**	**Total**
Structural Packaging	1	1	1	1	**0.49**
Docking Port/Sensors	2	3	3	1	**1.41**
Electronics /Cabling	3	2	2	3	**1.56**
Metric Weight	***0.2***	***0.3***	***0.3***	***0.2***	

The key result from this analysis is that the electronics were the most costly component. This result can be confirmed by viewing the inside of the module; most of the complexity and volumetric space constraints are caused by the electronics. The electronics were given a high non-scalability score because it is difficult to shrink the electronics for small modules like SWARM. However, it should be noted that the size of the electronics would remain approximately the same size for a module three to four times the size of SWARM. Thus, for large modules the electronics may be less of an issue, while the larger docking port may become more significant.

2.3. A Trade Model for Assembling a Large Space Telescope

There is current interest in the ability to assemble large systems in space. An example is DARPA's LASSO program, which will examine the feasibility of manufacturing a large optical structure in space. The proposed LASSO system is a 150-meter optical system in geosynchronous orbit [11]. This section investigates the on-orbit assembly of a large segmented primary mirror, which is part of a space-based telescope. The concepts developed in this section are very general, and could be applied to other scenarios such as the proposed LASSO system. It has been assumed that large mirrors (~20 meters) will be assembled in space using a stack of hexagon-shaped mirror segments. The

objective is to compare two methods for assembling the mirror. The first method uses a propellant-based tug spacecraft to move the segments from a central stowage stack to the mirror assembly. The second is an electromagnetic-based method that uses superconducting electromagnetic coils as a means of applying force and torque between two assembling vehicles to produce the same results as the propellant-based system. This system is termed Electromagnetic Formation Flight (EMFF) [12].

Metrics are required to compare these two methods. Usually cost is the metric chosen to make this type of comparison; the configuration that achieves the same level of performance for a lower cost is chosen. However, cost is directly proportional to mass for many space systems, thus mass is the metric analyzed in this report.

2.3.1. Problem definition and scope

Each segment is stowed in a vertical stack as shown in Figure 2-3-a. The tug begins at the top of the stack, and delivers each segment to the predetermined location in the primary mirror and then returns to the next segment in the stack. The mirror is assembled according to the numbering sequence shown in Figure 2-4. The size of the mirror and number of segments is a parameter that can be varied. The following items are not considered in this study:

- **Space effects:** Orbital dynamics and solar pressure.
- **Removal and installation processes:** Rotation and reorientation of the mirror while taking it from the stack and then just before attaching it to the mirror assembly. Also, the time to dock and connect the mirrors together.
- **Optimal trajectory planning / collision avoidance:** Certain delivery and return paths of the tug may be suboptimal, and alternative trajectories may be required to avoid collision with other segments. Also, issues such as optical contamination due to propellant plumes are not considered.
- **Optimal stacking configurations:** It may be more optimal to assemble the mirror using a horizontal stack rather than the vertical stack used for this study.

- **Imperfections in the control system:** The thrusters and EMFF subsystems may not perform perfectly at all times.
- **Optimal fuel usage:** There may be more globally optimal solutions for managing the propellant.
- **Larger trade space:** Only 20 and 30-meter diameter telescopes are considered. Large diameters could be explored.

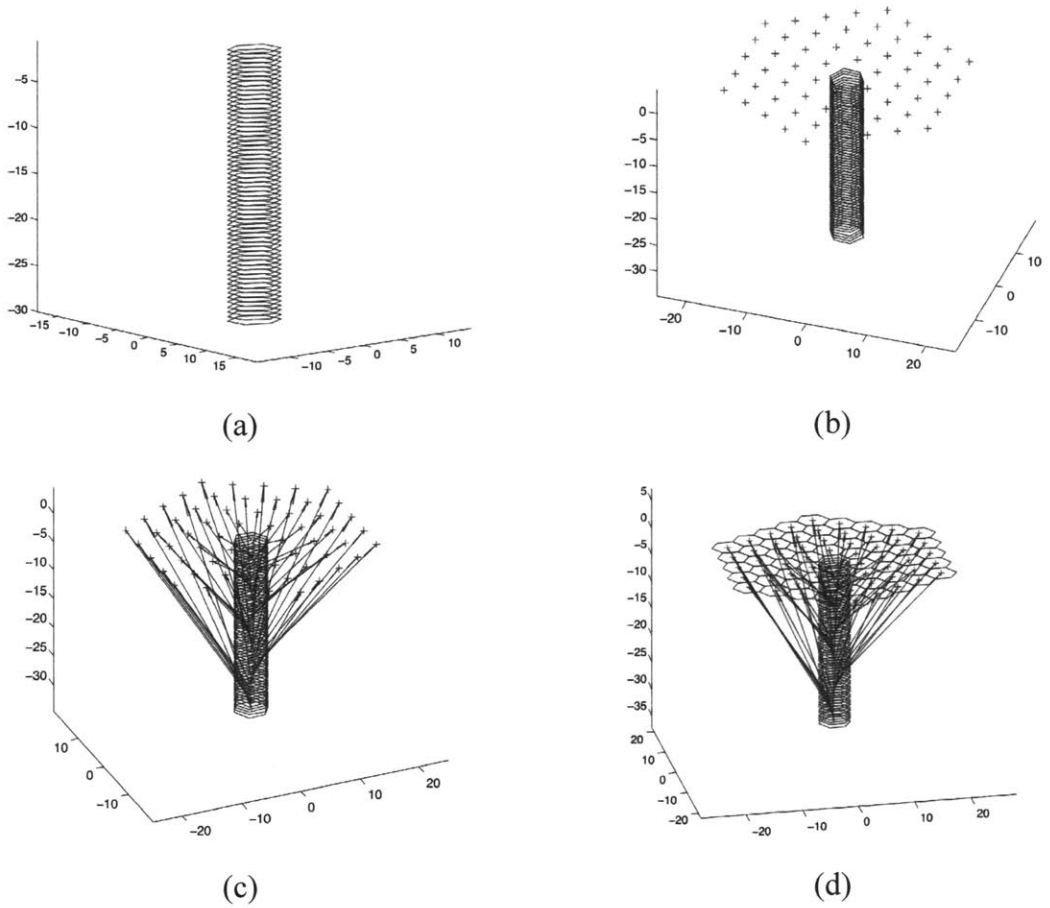

Figure 2-3: The segments start in a stack (a). The delivery point for each segment is predetermined and is represented as points (b). An optimal trajectory is chosen (c) and then the segment is delivered (d).

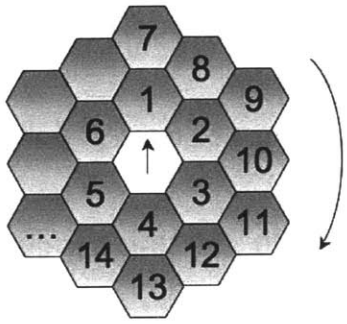

Figure 2-4: The assembling starts with number one and continues clockwise following the numbering sequence shown above.

2.3.2. Sizing the mirror segments and tug vehicle

The diameter of the mirror, D, and the number of segments, n, must be initially specified. The effective area of the mirror, A, can be determined using:

$$A_e = \frac{\pi D^2}{4} \qquad 2\text{-}1$$

Thus the area of an individual segment, A_s, is:

$$A_s = \frac{A_e}{n} \qquad 2\text{-}2$$

Where n is the number of segments. The side length of the hexagon can be determined using the known segment area (Figure 2-5):

$$s = \sqrt{\frac{2}{3\sqrt{3}} A_s} \qquad 2\text{-}3$$

Now that s is known, the center of the hexagon for each segment can be determined as shown in Figure 2-3-b.

The mass of an individual segment can be determined by assuming a known areal density of the mirror (ρ_{areal}). It will be assumed that the areal density includes the glass, coating, structural supports, and docking ports (Figure 2-5). Thus the mass of a single segment, $m_{segment}$, is then:

$$m_{segment} = \rho_{areal} A_s \qquad 2\text{-}4$$

The hexagonal mirror segments currently being used on the Keck telescopes will be used to approximate the size and mass of the mirror segments used in this study. The areal density for the Keck mirrors is approximately 190 kg/m^2, which includes the mass of the glass, supporting structures and actuators. Since much less mass would be required in a zero-g environment, it will be assumed that an advanced space version would be approximately 90% lighter. A 20 and 30-meter telescope with 60 segments and another with 90 segments will be considered in this study. A complete list of the baseline values for the 20-meter telescope is shown in Table 2-3.

Table 2-3: Baseline values for the mirror segments.

	Keck (approx. values)	**Space Telescope (assumed values)**
Effective diameter of the primary mirror	10 m	20 m
Effective area of the primary mirror	78 m^2	314 m^2
Number of segments	36	60/90
Area of a single segment	2.11 m^2	5.24/3.5 m^2
Size of a hexagon segment (*s*)	0.9 m	1.42/1.16 m
Areal density	190 kg/m^2	20 kg/m^2
Mass of a single segment	400 kg	104/70 kg
Mass of all segments	14400 kg	6300 kg
Length of stack	NA	15/22.5 m

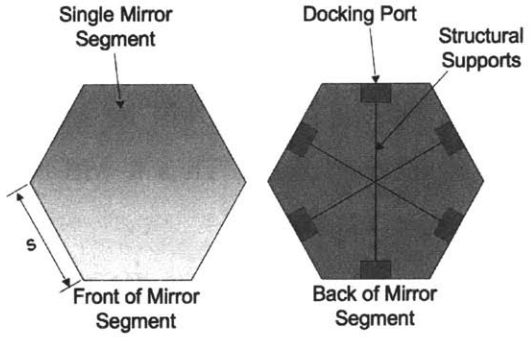

Figure 2-5: An individual mirror segment.

The mass of the tug, m_{tug} can be determined by assuming that:

$$m_{tug} = 2m_{segment} \tag{2-5}$$

This would put the center of mass for the combined system inside the volumetric space of the tug vehicle, which may be desirable for control purposes. The mass of the tug is a dry mass and does not include the propellant or EMFF components. The propellant components are the thrusters, tanks and fuel. The EMFF components are the electromagnet coils and reaction wheels. The cargo mass, m_{cargo}, is defined as:

$$m_{cargo} = m_{segment} + m_{tug} \tag{2-6}$$

It should be noted that the segment mass is only included in m_{cargo} when the tug is delivering a segment to be assembled. On the return trip to the stack the segment mass is not included. Also, the total mass, m_{total}, is defined as:

$$m_{total} = m_{cargo} + m_{subsystem} \tag{2-7}$$

where the subsystem mass, $m_{subsystem}$, is a summation of the propellant and EMFF-specific components such as thrusters, tanks, coils and reaction wheels. The next two sections discuss the individual propellant and EMFF subsystems. It will be shown that the total time to assemble, t_{total}, can be determined for a specified amount of subsystem mass.

2.3.3. Propellant-based subsystem

The objective of this section is to determine the total time required to assemble the mirror assembly when the propellant-based subsystem is used. It will be shown that the total time to assemble the mirror can be determined if the subsystem mass, msubsystem, is specified. The propellant-based tug was modeled as a spacecraft with eight sets of 3-axis thrusters (Figure 2-6). A "blowdown system" will be assumed, which uses the initial pressure inside its tanks to expel propellants. Thus it will be assumed that no electrical power is needed to generate thrust [13].

Besides the expelled propellant mass, there are many other components that add mass to the propellant-based system. Typically the tank mass, m_{tank}, can be estimated as

15% of the propellant mass, and the mounting hardware and propellant management devices, $m_{H/W}$, are an additional 30% of the tank mass [13]. Also, each thruster has a mass, m_{th}. These assumptions can be used to determine the subsystem mass:

$$m_{subsystem} = m_{pt} + m_{tank} + N_{th}m_{th} + m_{H/W} \quad 2\text{-}8$$

$$= m_{pt} + 0.15m_{pt} + N_{th}m_{th} + 0.3m_{tank} \quad 2\text{-}9$$

$$= m_{pt} + 0.15m_{pt} + N_{th}m_{th} + 0.3(0.15)m_{pt} \quad 2\text{-}10$$

Thus, the total subsystem mass for the propellant components can be estimated using:

$$m_{subsystem} \approx 1.2m_{pt} + N_{th}m_{th} \quad 2\text{-}11$$

where m_{pt} is the total mass of the propellant and N_{th} is the number of thrusters. The dry mass of the propellant system, $m_{pt,dry}$, is defined as:

$$m_{pt,dry} \equiv m_{subsystem} - m_{pt} \quad 2\text{-}12$$

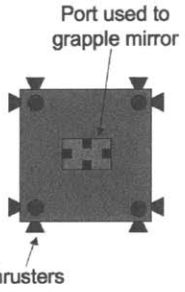

Figure 2-6: The "tug" used to assemble the mirror for the propellant-based subsystem.

The temporal profiles for the thrusters are shown in Figure 2-7, and can be used to determine the mass of the propellant.

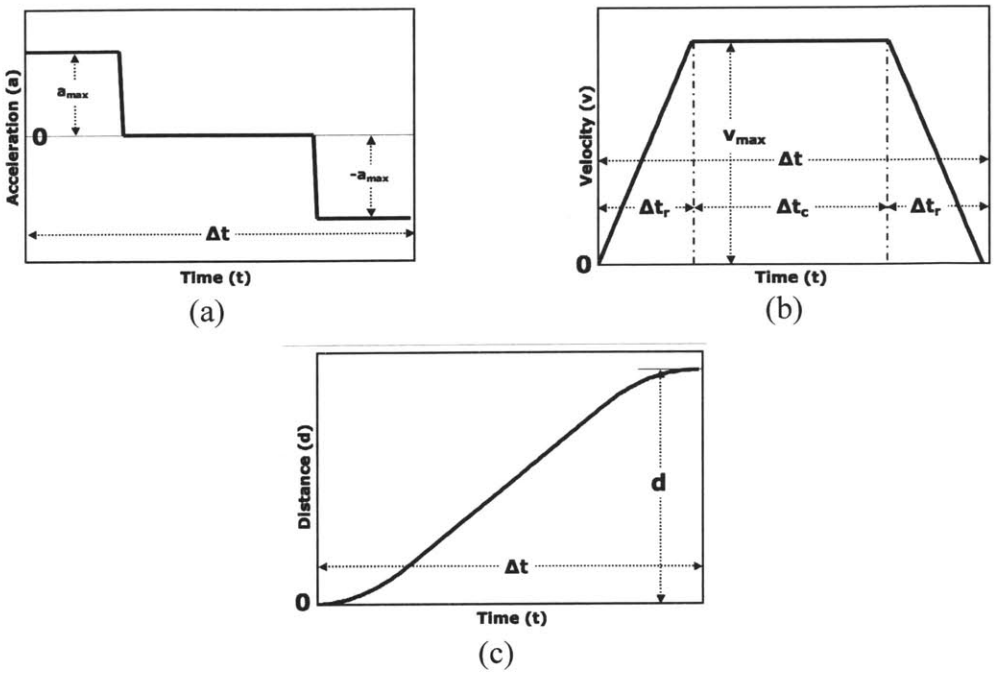

Figure 2-7: Temporal profiles for a single maneuver.

From Figure 2-7, it can be shown that the total change in velocity for a single maneuver is:

$$\Delta V_i = 2v_{\max,i} = \frac{4d_i}{\Delta t_i(1+c_i)} \qquad 2\text{-}13$$

where $v_{max,i}$ is the maximum velocity (Figure 2-7-c), d_i and Δt_i are the distance and time respectively for the i^{th} maneuver, and c_i is defined below. A maneuver is defined as either a single delivery of a segment, or a return trip of the tug to the stack. Thus, two maneuvers are required to assemble a single segment. The distance traveled during each maneuver (d_i) is predefined for each maneuver based on the known geometry and predetermined path. For the propellant case, the optimal path is a straight line between the starting and ending point of each maneuver (Figure 2-3-c). The variable c_i in Equation 2-13 is defined as:

$$c_i = \frac{\Delta t_{c,i}}{\Delta t_i} \qquad 2\text{-}14$$

where $\Delta t_{c,i}$ is the amount of time the tug coasts without firing the thrusters (Figure 2-7-b). Thus, the value of c_i is the fraction of time the vehicle coasts during each maneuver, and can be varied from zero to one. It can be seen from Equation 2-13 that ΔV_i is minimum

when c_i equals unity, for a fixed distance and time. However, as c_i approaches unity the acceleration becomes infinite, and as it approaches zero the thrusters near a "bang-bang" firing profile. Thus, a reasonable value of c_i can be chosen based on the limitations of the thrusters.

The "Rocket Equation" relates the ΔV_i to the propellant fuel required for each maneuver, $\Delta m_{pt,i}$ (Appendix B):

$$\Delta m_{pt,i} = m_{total,i} \cdot \left(e^{\frac{\Delta V_i}{I_{sp} \cdot g}} - 1 \right) \qquad 2\text{-}15$$

where

$$I_{sp} = \frac{v_e}{g} \qquad 2\text{-}16$$

where v_e is the exhaust velocity of the propellant and g is the gravitational constant at sea level. The total mass, $m_{total,i}$, is the mass being moved by the tug during the i^{th} maneuver, which includes the cargo mass, the fuel mass required to complete all of the $2n$-1 future maneuvers, and the dry mass of the thrusters and tanks:

$$m_{total,i} = m_{cargo,i} + \sum_{j=2n}^{i} m_{pt,j} + m_{pt,dry} \qquad 2\text{-}17$$

Note that in Equation 2-17 the summation starts at the very last ($j = 2n$) maneuver, and sums backwards to the present (i^{th}) maneuver. This is because the total mass must also include the propellant required for all of the future maneuvers. Thus, the first maneuver has to carry all the fuel required to perform the single maneuver plus all the remaining maneuvers. The algorithm for determining the total assembly time for the propellant subsystem is summarized in Figure 2-8. By combining Equations 2-13 and 2-15, the time required for each maneuver can be determined:

$$\Delta t_i = \frac{4d_i}{(1+c_i) I_{sp} g \log_e \left(\frac{\Delta m_{pt,i}}{m_{total,i}} + 1 \right)} \qquad 2\text{-}18$$

Thus, the total time to assemble the entire mirror can be determined by summing the time required for each maneuver:

$$t_{total} = \sum_{i=2n}^{1} \Delta t_i \qquad 2\text{-}19$$

As shown in Figure 2-8, the total propellant mass, m_{pt}, is determined using Equation 2-11 by knowing the total subsystem mass ($m_{subsystem}$). However, the allocation of m_{pt} for each of the maneuvers must be determined (Figure 2-9). More specifically, even though the total propellant mass is known, it is unknown how this fuel should be allocated to each maneuver. It is apparent that there is an optimal way to distribute this fuel, since each maneuver travels a different distance with a varying mass. Thus, it is suboptimal to allocate an equal amount of fuel to each maneuver. A more optimal method allocates the fuel according to the maneuver's order in the assembling process. The maneuvers that occur early in the assembly process get less fuel since they are going the shortest distances. To distribute the propellant in this way it can be assumed that the following relationship exists:

$$m_{used}(j) = \beta j^z \qquad 2\text{-}20$$

where m_{used} is the cumulative amount of fuel consumed during the total $2n$ maneuvers, β is a constant, and j represents the assembly order of the segment. The variable j can have integer values ranging from zero to $2n$, and the exponent z must be determined. Equation 2-20 can be rewritten using known values for the constants as shown in Figure 2-9:

$$m_{used}(j) = \frac{m_{pt}}{(2n)^z} j^z \qquad 2\text{-}21$$

A finite difference of $m_{used(j)}$ can be used to determine the amount of fuel allocated for each maneuver, $\Delta m_{pt,i}$:

$$\frac{\Delta m_{pt,i}}{\Delta j} = \frac{m_{pt}}{(2n)^z}\left(j^z - (j-1)^z\right)\Big|_{j=i,\Delta j=1} \qquad 2\text{-}22$$

Thus, if the mass of the subsystem ($m_{subystem}$) is specified, then the total time to assemble the telescope (t_{total}) can be determined using Equations 2-11, 2-18, 2-19 and 2-22. The exponent z is varied from 0.1 to 2, and the value that yields the minimum t_{total} is chosen. *A* list of the input parameters for this algorithm can be found in Table 2-4.

Table 2-4: The assumed properties and input parameters used for the propulsion subsystem.

Propulsion System Type	cold gas
Total Impulse	4-200 $\bullet 10^3$ N-s
I_{sp}	100 s
c (Equation 2-14)	0.7

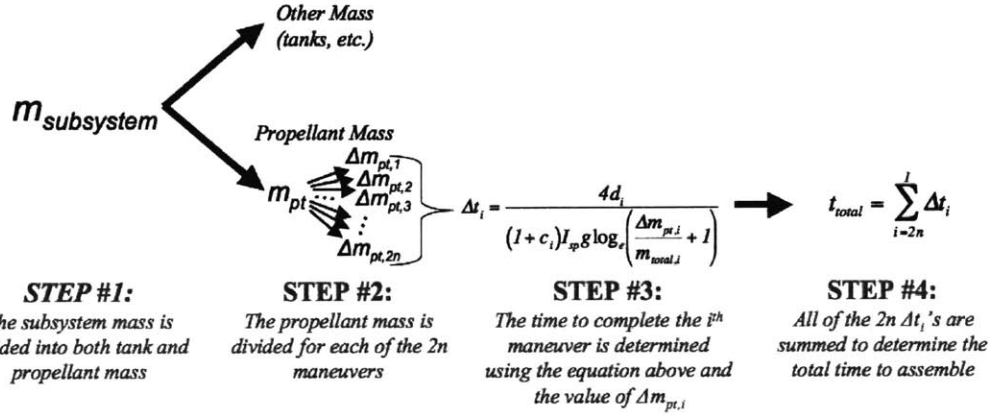

Figure 2-8: The algorithm for determining the total assembly time when using the propellant-based subsystem.

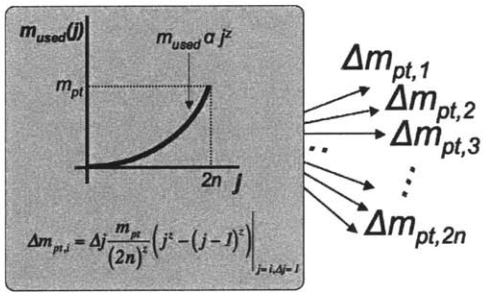

Figure 2-9: The total propellant mass is distributed amongst the maneuvers in the way shown above.

Since the assembly time decreases as the tug acceleration increases, the maximum allowable acceleration could set a lower bound on the assembly time. The acceleration for a single maneuver is:

$$a_i = \frac{4d_i}{\Delta t_i^2 (1 - c_i^2)} \tag{2-23}$$

The maximum acceleration can be determined by comparing all of the single maneuvers:

$$a_{\max} = \max\{a_i\} \tag{2-24}$$

Similarly, the total impulse could be used to set a lower bound on the assembly time by comparing the maximum total impulse values with those attainable from the actual thrusters. The total impulse for a single maneuver is:

$$I_i = m_{total,i} \frac{2d_i}{\Delta t_i (1 + c_i)} \tag{2-25}$$

The maximum total impulse can be determined by comparing all of the single maneuvers:

$$I_{\max} = \max\{I_i\} \tag{2-26}$$

Thus, the total time required to assemble the mirror using a propellant system can be calculated using Equations 2-18 and 2-19. The next section will follow a similar path to determine the total time required to assemble the mirror using the EMFF-based subsystem

2.3.4. EMFF-based subsystem

The objective of this section is to determine the total time required to assemble the mirror using the EMFF-based subsystem. Screenshots from a video animation, which demonstrates EMFF assembling a large space structure, are shown in Figure 2-10. Also, pictures of the EMFF testbed can be found in Figure 2-11. It will be shown that the total time to assemble the mirror can be determined if the subsystem mass is specified. A schematic of the EMFF-based assembly can be found in Figure 2-12. Two EM coils are fixed atop of the "stack" of mirrors, and a single coil is on the tug. A reaction wheel is used for each set of coils to counteract the torque produced by the electromagnetic forces. Though assembling the mirror segments is a three-dimensional problem, it can be

simplified to two-dimensions by assuming that the EM coils on the stack can rotate as shown in Figure 2-12. Thus the movement of the tug always lies within a plane and can be specified by a set of two-dimensional starting and ending points.

The total subsystem mass for EMFF is divided between the EM coils and reaction wheels:

$$m_{subsystem} = m_{coils} + m_{RW} \qquad 2\text{-}27$$

where m_{coils} is the mass of all three coils, and m_{RW} is the mass of both sets of reaction wheels. A summary of how the coil and reaction wheel mass is divided among the stack and tug is shown in Table 2-5. These values were chosen based on initial iterations, since an exhaustive search for the optimal values was not considered in this study.

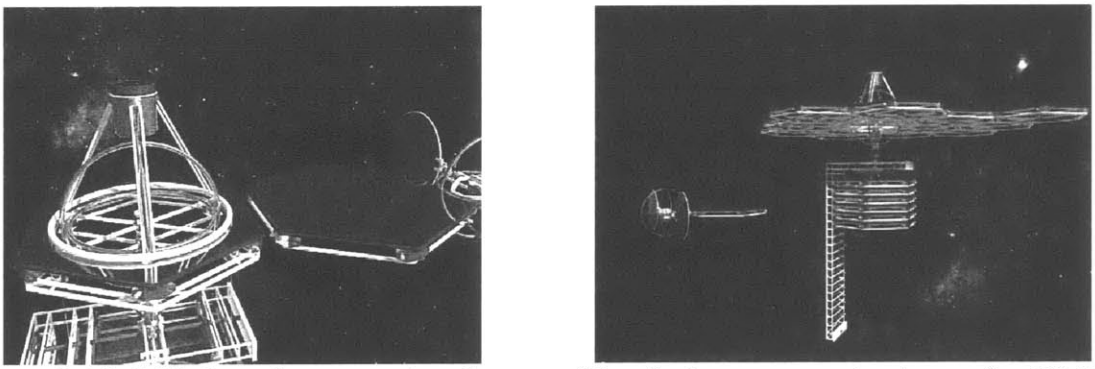

Figure 2-10: Still shots demonstrating the assembly of a large space structure using EMFF.

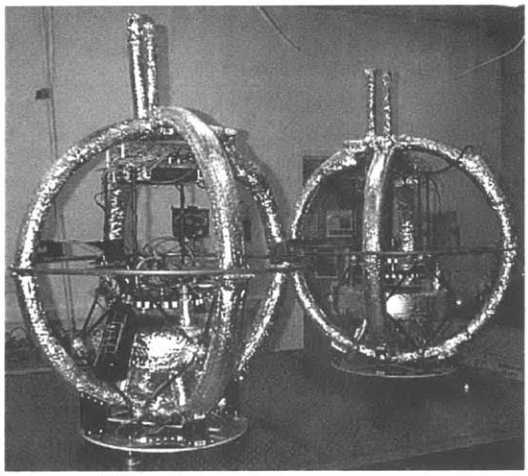

Figure 2-11: Two experimental EMFF vehicles.

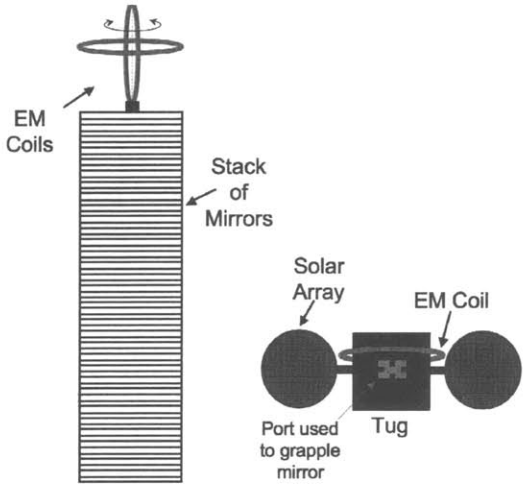

Figure 2-12: A schematic of the EMFF assembly with the stack of mirrors. This schematic is not to scale, and many components are not included (ex. reaction wheels).

Table 2-5: The masses of the reaction wheels and coils for the tug and stack.

Description	Value
Total reaction wheel mass	$m_{RW} = \frac{2}{5} m_{subsystem}$
Total EM coil mass	$m_{coils} = \frac{3}{5} m_{subsystem}$
Reaction wheel mass (tug)	$m_{RW,T} = \frac{1}{3} m_{RW}$
Reaction wheel mass (stack)	$m_{RW,S} = \frac{2}{3} m_{RW}$
EM coil mass (tug)	$m_{coil,T} = \frac{2}{5} m_{coils}$
EM coil mass (stack)	$m_{coils,S} = \frac{3}{5} m_{coils}$

At the core of the EMFF analysis is an algorithm that determines the optimal time to complete a single maneuver, Δt_i, based on a set of inputs [14]. These inputs are listed in Table 2-7, and they specify the starting and ending points of the maneuver along with the general design of the EMFF subsystem (maximum electrical current, size and mass). An important input parameter is NA_{coil}, which is the number of EM wrappings of superconductive wire (N) times the area of the coil (A_{coil}). It can be determined using:

$$NA_{coil} = \frac{I_c}{4\rho_{wire} i_{\max}} m_{coil} D_{coil} \qquad 2\text{-}28$$

where I_c is the critical coil current density (A/m^2), ρ_{wire} is the wire density (kg/m^3), i_{max} is the maximum amount of coil current, m_{coil} is the mass of a single coil and D_{coil} is the diameter of the coil (Table 2-6). The algorithm used to determine the total assembly time using the EMFF subsystem is summarized in Figure 2-13, and a list of the input parameters can be found in Table 2-7.

Table 2-6: Properties of the EM coil used to calculate NA_{coil} (Equation 2-28). The slash designates the different mirror diameters of 20 m and 30 m, respectively.

D_{coil}	2.58/2.11 m
$\rho_{current}$	13000 A/cm^2
ρ_{wire}	8000 kg/m^3

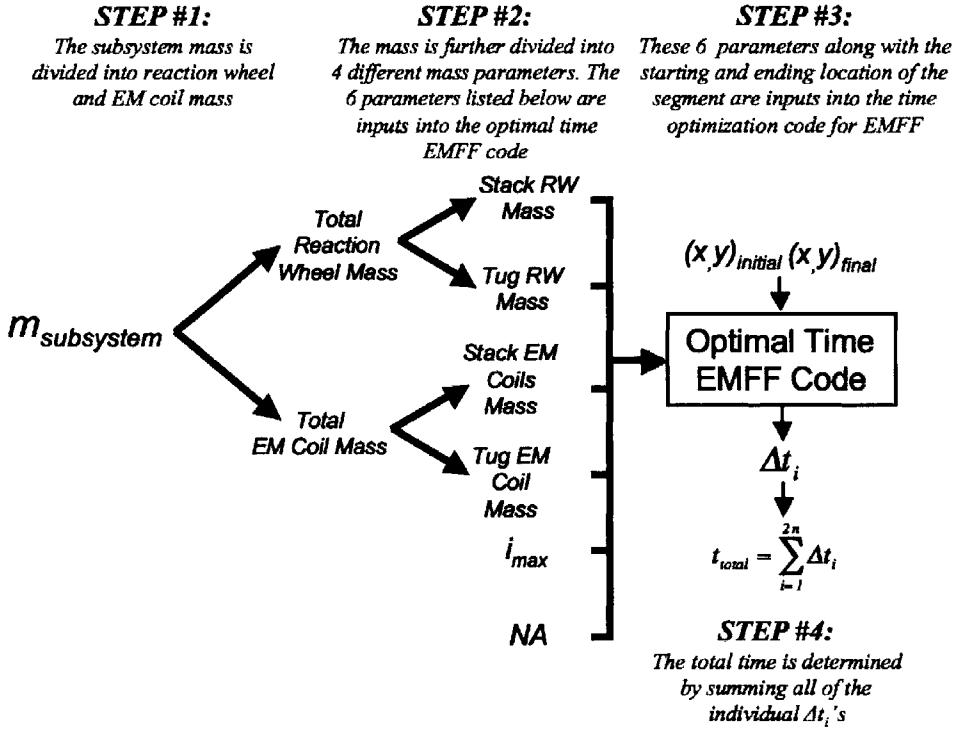

Figure 2-13: The algorithm to determine the total assembly time when using EMFF.

Table 2-7: Input to the EMFF optimal time algorithm.

Description	Symbol	Assumed Value
The starting and ending points for each maneuver	$(x,y)_{\text{initial}}$ and $(x,y)_{\text{final}}$	Variable
The maximum current in the EM coils.	i_{max}	100 A
The mass of the reaction wheel located on the stack.	$m_{RW,S}$	$\frac{2}{3}m_{RW}$
The mass of the reaction wheel located on the tug.	$m_{RW,T}$	$\frac{1}{3}m_{RW}$
The mass of the two EM coils located atop the stack of mirrors.	$m_{coils,S}$	$\frac{3}{5}m_{coils}$
The mass of the single EM coil located on the tug.	$m_{coils,T}$	$\frac{2}{5}m_{coils}$
An EM parameter, which equals the number of wire turns (N) times the area of the coil (A_{coil}).	NA_{coil}	$\frac{I_c}{4\rho_{wire}i_{\max}}m_{coil}D_{coil}$

2.3.5. Results

To compare the propellant and EMFF-based subsystems, the total time to assemble the primary mirror of a telescope was determined for a given amount of subsystem mass (Equations 2-11 and 2-27). These calculations were performed for 30 and 20-meter diameter telescopes with both 90 and 126-segments, and the subsystem mass was varied from 100 to 250 kg. Figure 2-14 summarizes the results by directly comparing the amount of time required to assemble the telescope for both systems. For these particular cases, the propellant-based system is able to assemble the telescope 2 to 3.5 times faster. However, as the telescope diameter increases, the difference between the two subsystems reduces. Figure 2-15 through Figure 2-18 show the actual assembly time. As expected, larger telescopes with more segments require more time to complete the assembly process. It should be noted that the telescope could be reconfigured without additional mass when using EMFF, though this is not the case with the propellant-based system. Thus, EMFF could offer substantial mass savings if reconfiguration is required.

Figure 2-19-a,b show the maximum acceleration and total impulse, respectively, for the propellant subsystem when assembling a 20-meter telescope with 90 segments. This case is considered because it contains the largest acceleration and total impulse values. It can be seen that the maximum acceleration varies from 0.15 to 0.45 m/s^2. As mentioned earlier, the acceleration could determine or limit the time required to assemble the telescope. For example, if the maximum allowable acceleration was 0.15 m/s^2, then the assembly time must be greater than 1.5 hours. Similarly, the total impulse could be used to set a lower bound on the assembly time by comparing the maximum total impulse values with those attainable from the actual thrusters. It can be seen that the total impulse varies from 150 to 400 N-s. These values fall within the range of typical thruster specifications, and thus the total impulse for this particular case is not a limiting factor (Table 2-3).

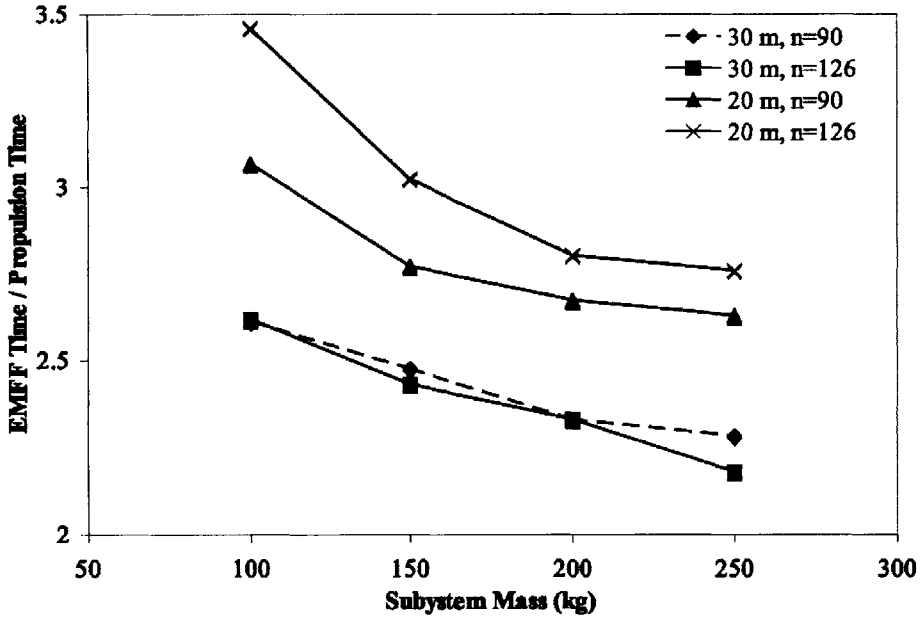

Figure 2-14: The ratio of the times to assemble the telescope for EMFF and propellant.

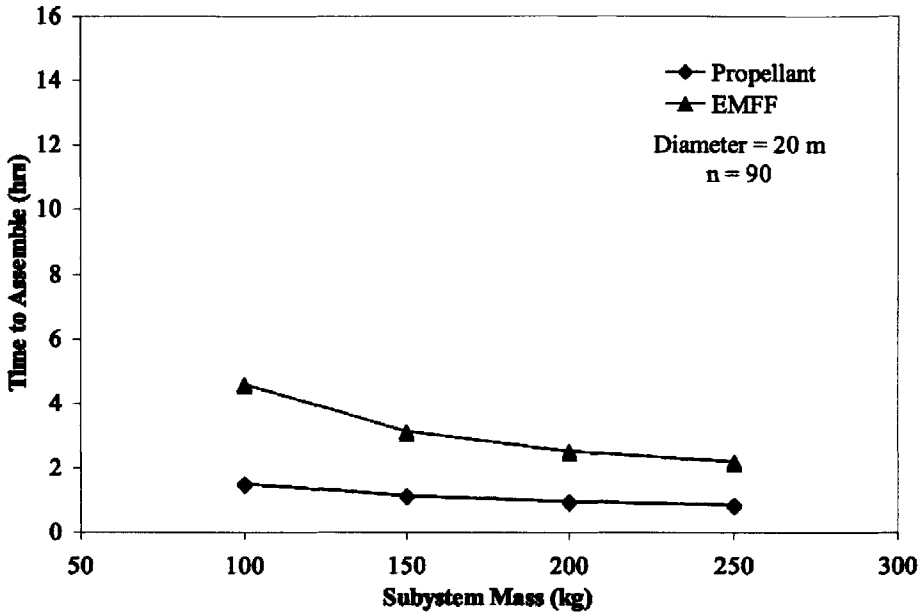

Figure 2-15: Comparing propellant and EMFF-based subsystems for a 20-meter telescope with 90 segments.

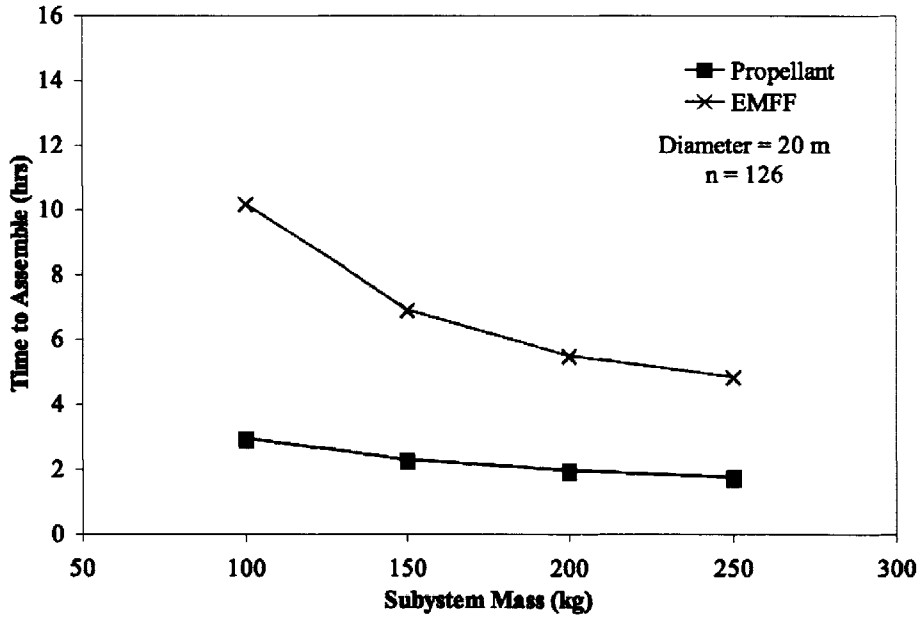

Figure 2-16: Comparing propellant and EMFF-based subsystems for a 20-meter telescope with 126 segments.

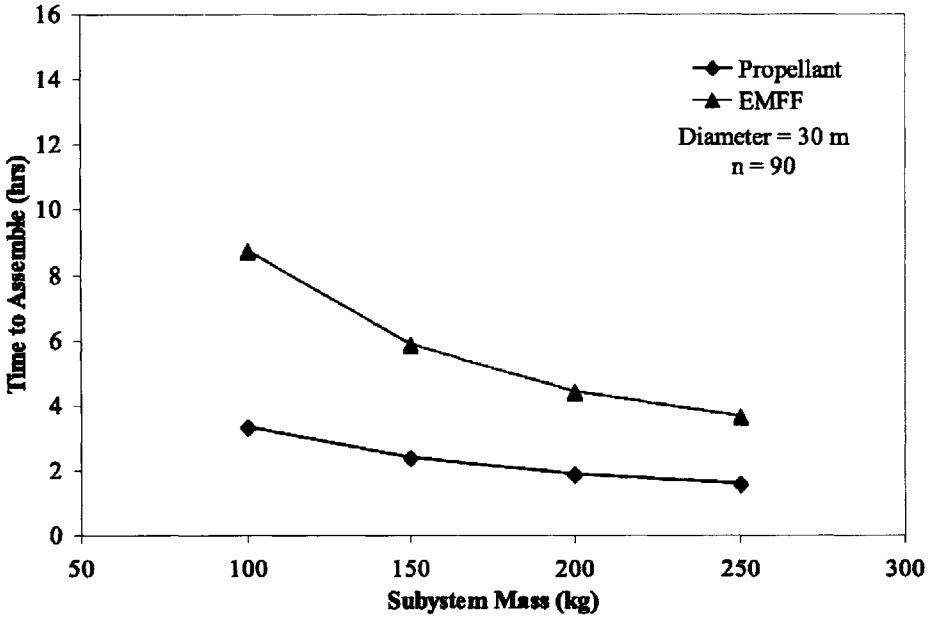

Figure 2-17: Comparing propellant and EMFF-based subsystems for a 30-meter telescope with 90 segments.

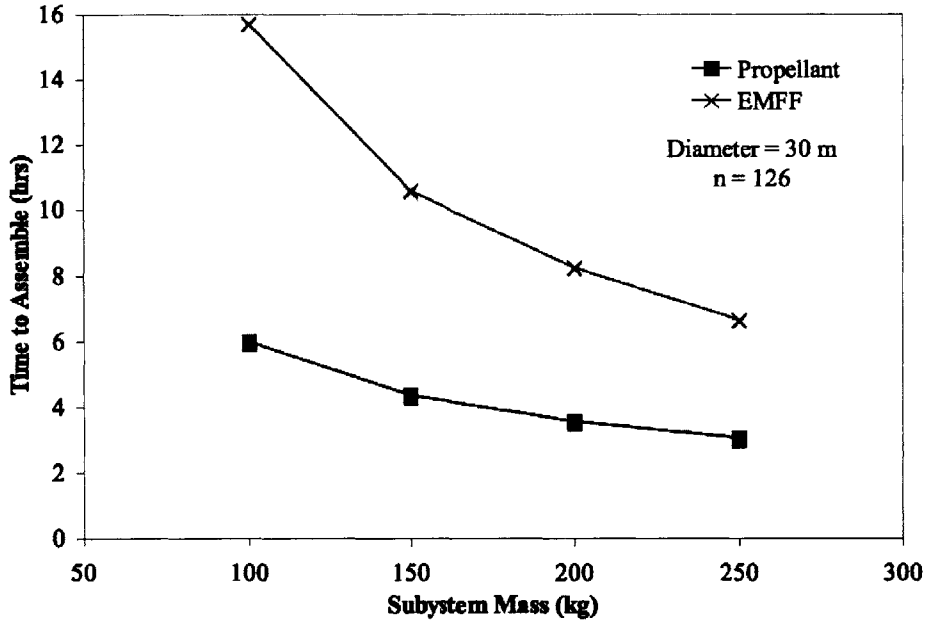

Figure 2-18: Comparing propellant and EMFF-based subsystems for a 30-meter telescope with 126 segments.

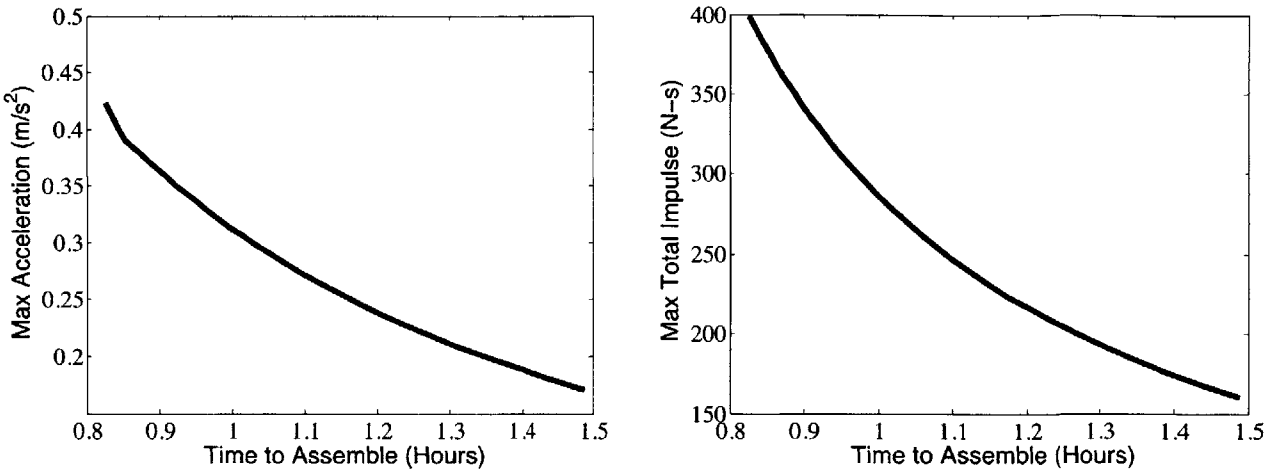

(a) (b)

Figure 2-19: (a) The maximum acceleration (Equation 2-24) of the segment and (b) the maximum total impulse (Equation 2-26) required by the thrusters for a 20-meter telescope with 90 segments.

2.4. Summary

This chapter presented concepts of modular space systems, which included defining a module as an encapsulation of highly interconnected parts, whose external connections are minimized and simple. An overview of SWARM was given to serve as an example of a modular system, and the definition of a module was directly applied to this system. Then EMFF and propellant-based architectures were compared to determine which is able to assemble a segmented mirror in less time for a given amount of mass. It was found that the propellant-based system is able to assemble the telescope 2 to 3.5 times faster; though EMFF could offer substantial mass savings if reconfiguration is required.

A module can be defined as a spacecraft module as described in Sections 2.1 and 2.2, or as a single mirror segment as described in Section 2.3. For both of these cases, the modules need to be connected together autonomously. The common component required to physically connect the modules is the docking port, which is the subject of the next chapter.

Chapter 3. Docking Ports for Autonomous Assembly and Reconfiguration

As discussed in the previous chapters, there are many applications for modular technology. A module could be defined as a spacecraft module as described in Section 2.1 and 2.2, or as a single mirror segment as described in Section 2.3. For a set of independent modules, there is the need to connect all of them together autonomously. The common component required to physically connect the modules is the docking port, which must be placed at each node where the modules are to be connected. This connection may be rigid or flexible depending on the mission. This chapter presents a brief history of docking ports, and then generalizes to form a comprehensive list of docking port capabilities for unmanned space missions where docking is needed to assemble a large number of modules. Classifications are developed for different types of docking ports based on the locking components and the overall geometry. This chapter concludes with an example of a universal docking port design.

3.1. Brief History of Docking Ports

Though a docking port can be generically thought of as a device used to connect multiple components in space, most of the past work with these devices has been focused on technology solely for manned spaceflight. The first docking in space took place on March 16th, 1966 during the United State's Gemini 8 mission. The docking port used during this historic mission had a cup and cone design as shown in Figure 3-1, and served to demonstrate the ability to rendezvous and dock to a separate orbiting spacecraft [15]. Docking technology was advanced and demonstrated as part of the following manned space programs:

- Apollo (USA) 1968-1972

- Skylab (USA) 1973-1974
- Salyut and Mir Space Station (Russia) 1971-1999
- Apollo-Soyuz (USA/Russia) 1975
- Space Shuttle (USA) 1984-present
- International Space Station (USA/Russia/Others) 1998-present

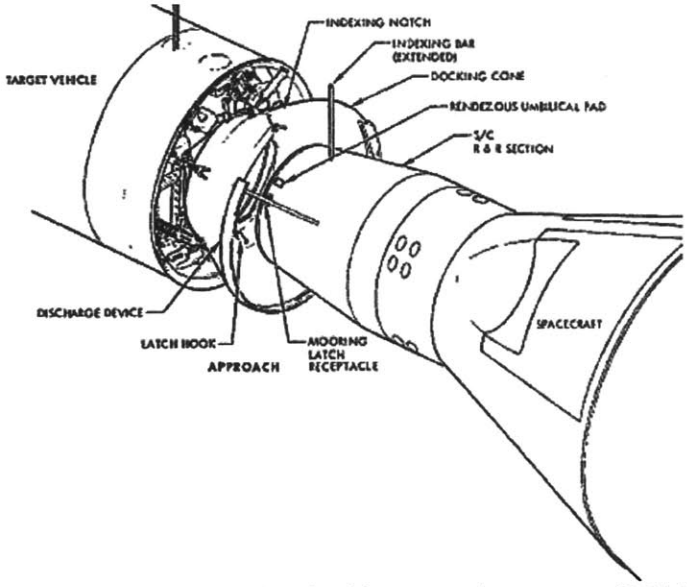

Figure 3-1: The Gemini 8 docking port (courtesy of NASA).

The docking mechanisms for human missions required the following operations in sequence [16]:

- **Reception:** The docking ports make physical contact with mechanical guides, which align the two vehicles.
- **Impact attenuation:** Any relative velocities are attenuated to zero to prevent elastic rebound of the vehicle. The attenuation is typically accomplished using a spring-damper device.
- **Capture:** This is the point where the two docking vehicles can no longer escape each other. This is typically accomplished through spring-loaded latches.

- **Retraction and structural alignment:** After capture, the two spacecraft are only loosely connected to each other, thus the lateral and angular misalignments must be removed before the structural connection is created. This generally involves additional mechanical guides, which improve the alignment during a retraction motion.
- **Structural connections:** The structural locking mechanism is engaged which rigidly connects the two vehicles.
- **Utilities connection:** Connections such as power and communication are made. If the human crew performs this manually, it does not occur until after pressurization.
- **Pressurization:** Pressurization of the volume between the two vehicles. Typically the pressure sensors in the tunnel and between the seals provide information to ensure successful pressurization.
- **Opening of hatches:** The hatches are opened which allow crew and/or cargo to pass between the two docked vehicles. There may be post-docking operations such as removing mechanical guides, etc.

Below is a list of docking port designs that have been developed for past or current space flight programs. A brief description and schematic are given for each design.

Apollo probe-drogue docking system [17]: Used for all of the Apollo Moon-landing and Skylab programs. It has an extendable and retractable probe that enters the drogue (Figure 3-2). A spring loaded latch mechanism is used to achieve capture. This mechanism is located on the end of the probe, and is effective once the probe has entered the back of the drogue (Figure 3-3). Shock attenuation is achieved through a rod damping mechanism located on the end of the probe (Figure 3-4). Twelve hook-type latches are used to form a rigid structural connection. After the hatches have been opened, the drogue and probe must be removed to allow for the passage of the crew and cargo.

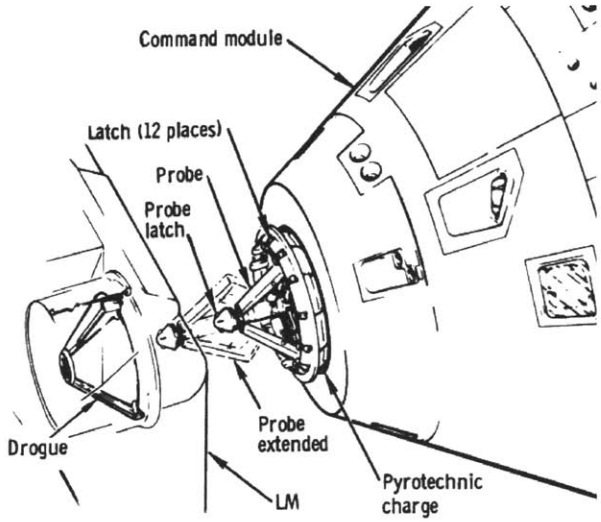

Figure 3-2: Apollo probe-drogue docking system (courtesy of NASA).

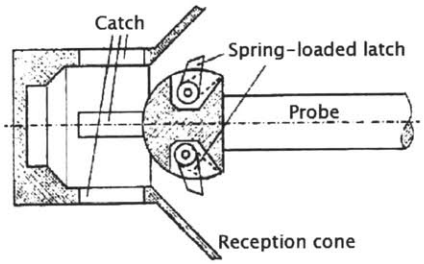

Figure 3-3: An example of a spring-loaded latch used with a probe and drogue docking port (courtesy of Wigbert Fehse).

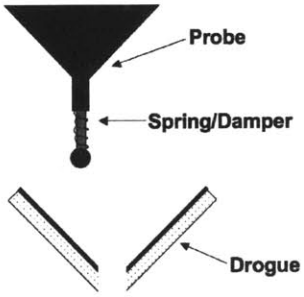

Figure 3-4: Spring and damper system used for the probe and drogue docking port.

Russian probe-drogue docking system: Used in the past during the Solyut and Mir Space Station programs (Figure 3-5). It is also currently being used for the manned Soyuz and unmanned Progress spacecraft. The European's Automated Transfer Vehicle (ATV) also

plans to use a similar design. The design is very similar to the Apollo probe-drogue system described above.

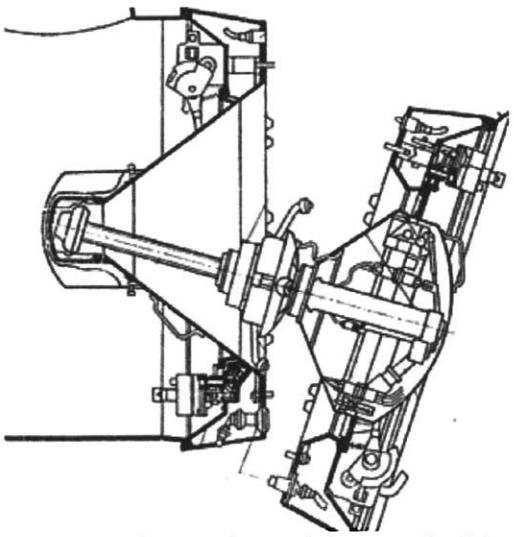

Figure 3-5: Russian probe and drogue docking port.

Apollo-Soyuz docking port [18][19]: The US and Russia each developed their own design, but worked together to produce standardized interface specifications so that both the Apollo and Soyuz spacecraft could dock together in space (Figure 3-6). This was the first attempt to develop a docking port design that could be docked to an identical copy of itself. Thus, it was the first *universal* docking port. During docking, one port is considered active and the other is passive. The guide ring on the active port extends outward from the structure ring and captures the passive system on the docking vehicle using latches located on each of the guide petals. The guide ring is attached to the structural ring by six shock absorbers, which are placed in a "Stewart platform" configuration (Figure 3-7). This configuration allows for alignment of the two guide rings before capture and also aids in the shock attenuation. After damping out any relative motion between the two spacecraft, the guide ring on the active port is retracted and 24 structural hooks are used to form a rigid connection.

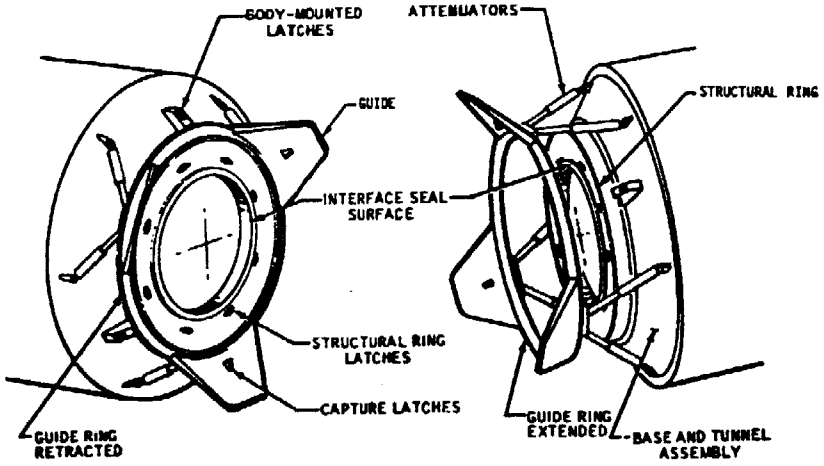

Figure 3-6: Apollo-Soyuz docking port (courtesy of NASA).

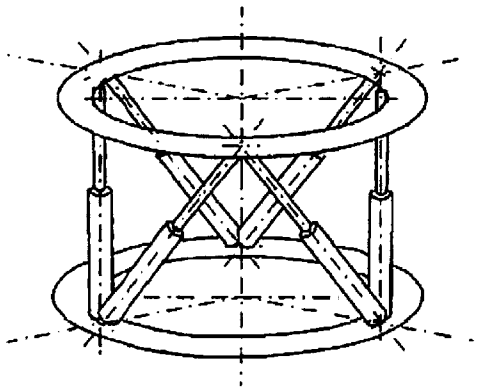
Figure 3-7: A "Stewart platform" is used for alignment and shock attenuation (courtesy of Wigbert Fehse).

Androgynous peripheral docking system (APDS) [20]: Initially developed for docking between the Russian Buran space shuttle and the Mir space station. It was later modified for docking between the US space shuttle and Mir. The design is very similar to the Apollo-Soyuz peripheral docking port described above. One visible difference is that the petals were modified to point inward (Figure 3-8).

Androgynous peripheral attach system (APAS): The docking port currently used to dock the US space shuttle to the International Space Station (ISS). It is very similar to the APDS described above (Figure 3-8).

Figure 3-8: The Androgynous Peripheral Docking System (APDS) (left). The Androgynous Peripheral Attach System (APAS) (right) (courtesy of RSC Energia)

ISS Common Berthing System [21]: For a berthing system, the docking vehicle (chaser) is delivered to a meeting point with zero nominal relative velocities and angular rates. A manipulator, grapple mechanism and fixture are used to transfer the captured vehicle to the corresponding attachment fixture on the target vehicle (Figure 2-9). This is essentially how the ISS has been assembled using the ISS Berthing System. The ring used to rigidly join the connecting components is shown in Figure 3-10. The Canadarm is used as the manipulator.

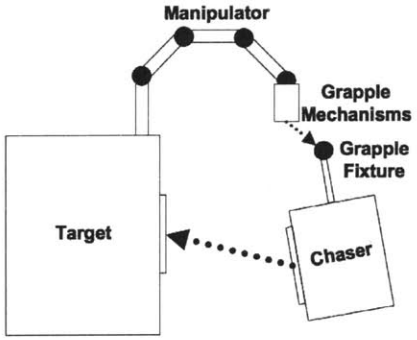

Figure 3-9: A schematic demonstrating a berthing. The grapple mechanism connects to the fixture on the chaser and then docks the two vehicles.

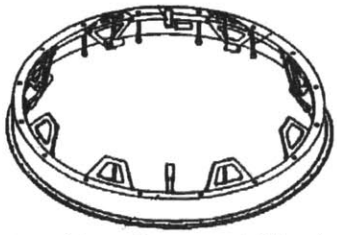

Figure 3-10: The ISS Common Berthing System. This ring is used to rigidly join the two connecting ISS components (courtesy of NASA).

DARPA's Orbital Express Grapple/Docking Mechanism [22]: This mission is scheduled to launch in September 2006 on the Air Force Space Test Program STP-1 mission. A manipulator will reach out and attach to the chaser's grapple mechanism (Figure 2-9). The two spacecraft (ASTRO and NextSat) will be connected using the docking mechanism (Figure 3-11).

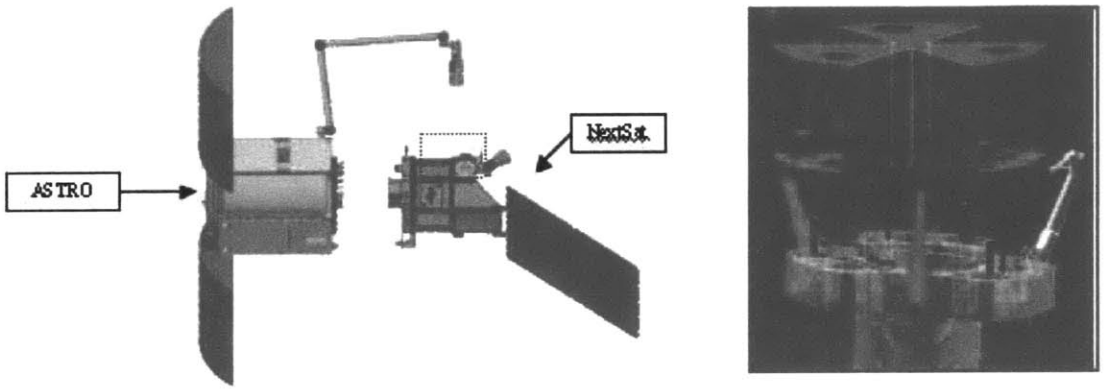

Figure 3-11: DARPA's Orbital Express mission. The two docking spacecraft (a) with a close-up of the grapple/docking mechanism (b) (courtesy of DARPA).

Low Impact Docking System (LIDS) [23]: This is very recent work done by NASA in developing docking port technology (Figure 3-12). The effort began as part of the X-38 project, and included demonstrating how the X-38 could be docked to the ISS. The prototype LIDS system only demonstrates the new or nontraditional subsystems, including an electromechanical actuated extension/retraction system (mini six degree-of-freedom platform), a load-sensing force-feedback compliant capture ring, electromagnets for soft-capture, passive alignment guides, and a control system with custom software and electronics. The prototype design does not address the tunnel structure, seals, structural latching system, pressurization system, and hatches since they are considered traditional proven subsystems. The project is now referred to as the Advanced Docking Berthing System (ADBS).

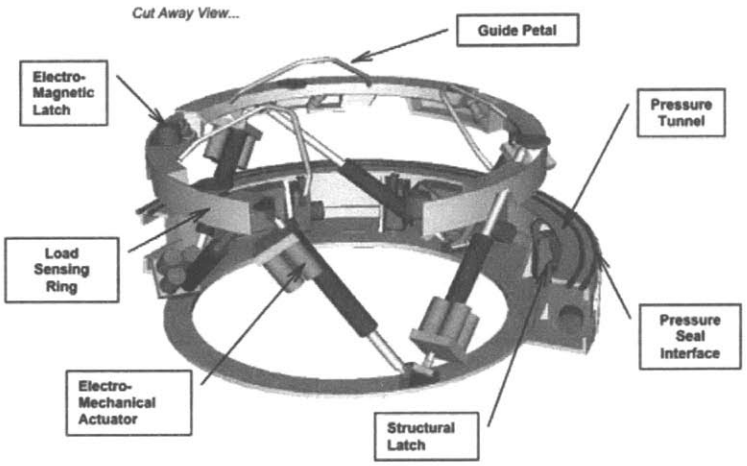

Figure 3-12: Low Impact Docking System (LIDS) (courtesy of NASA).

Autonomous Satellite Docking System (ASDS) [24]: Developed by Michigan Aerospace for autonomous unmanned docking of micro-satellites in a micro-gravity environment. This a non-universal design (see Section 3.2) with the ability to soft-dock. It is scalable with a high tolerance to misalignment.

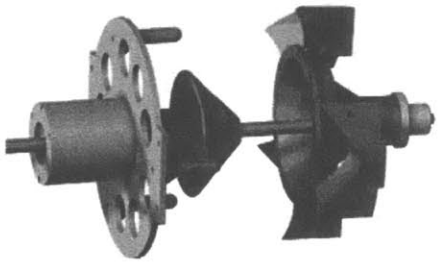

Figure 3-13: Autonomous Satellite Docking System, Developed by Michigan Aerospace (courtesy of Michigan Aerospace)

The docking systems and procedures mentioned above were developed for manned spaceflight. There has been little effort to develop docking systems for unmanned autonomous vehicles. The United States currently lacks the ability to autonomously dock spacecraft in orbit. For human missions, the design is largely governed by the size of the passageway [16]. The design requirements for unmanned missions are quite different, since there is no need for a pressurized tunnel to transfer the crew and/or cargo between the docked vehicles. The next section seeks to define the major design requirements, or

capabilities of unmanned docking systems. Some of the same concepts used for human missions carry over to an equivalent design requirement for unmanned missions.

3.2. Capabilities

This section develops a list of docking port capabilities for unmanned space missions where docking is needed to autonomously assemble space systems. The following is a list of docking port capabilities including a brief description:

Universal: All of the ports are identical in design and fabrication, yet they have the ability to dock together (i.e. one cannot always be male while the other is always female). By being universal, any two identical ports can dock together. This requirement is very subtle, but imposes large restrictions on the design.

Large docking tolerances: Two modules are able to dock even with substantial initial misalignment. Thus, the docking port must aid in attenuating the initial alignment error (Figure 3-14).

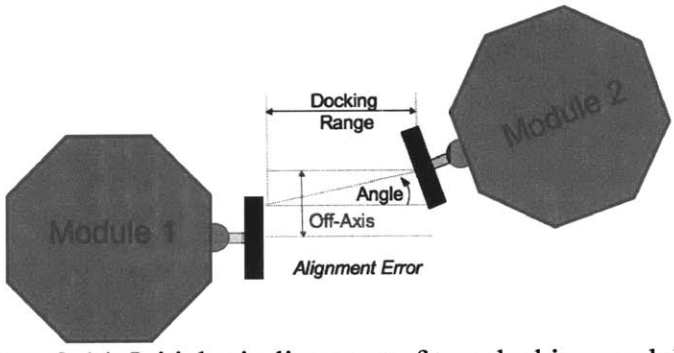

Figure 3-14: Initial misalignment of two docking modules.

Computer control: The docking port must be controllable from an onboard or remote computer, with the necessary sensors so the computer can monitor the state (e.g. fully open, locked, etc.). This provides the ability for the modules to be assembled and reconfigured autonomously.

Soft contact and capture: A soft capture occurs when two docking ports remain in contact without a rigid mechanical lock. Meaning, there is an attractive force that pulls the two modules together and holds them in place. The soft capture attenuates any non-zero relative velocity during initial contact without transferring large shock loads between modules. With a soft capture it is less likely that two modules would collide during docking. Most current docking ports require a non-zero velocity to activate latches, and thus run the risk of missing the target with dangerous amounts of kinetic energy. The nearly fatal collision of the Progress cargo ship and Mir during a docking maneuver in 1997 is an example of the dangers involved with non-zero velocity docking. Electromagnets may be an effective method for soft capture [25].

Transfer mechanical loads: By mechanically connecting the modules, separate propulsion and ACS modules are able to control the translation and rotation of all the connected modules. Also, it is possible to form one large rigid structure by connecting multiple small modules.

Fine alignment: Being able to connect two modules very precisely may be important if the connecting modules form an optical payload. Though it is likely that a second stage adjustment will be necessary for high precision alignments, it may be desirable for the docking port to provide a certain level of initial fine alignment.

Large angle articulation: The docking port is able to articulate before or after docking (Figure 3-15). This gives the modules the ability to form different shapes.

Electrical connection for power and data lines: Modules should have the ability to share electrical power. Thus, a central power module (such as a solar panel) could distribute power to the entire module cluster. Data lines allow for communication between modules, which is necessary for docking/undocking, transferring range data, and general system control. These connections also allow one module to control a passive module that does not have a computer, power, etc. unless it is connected to another module.

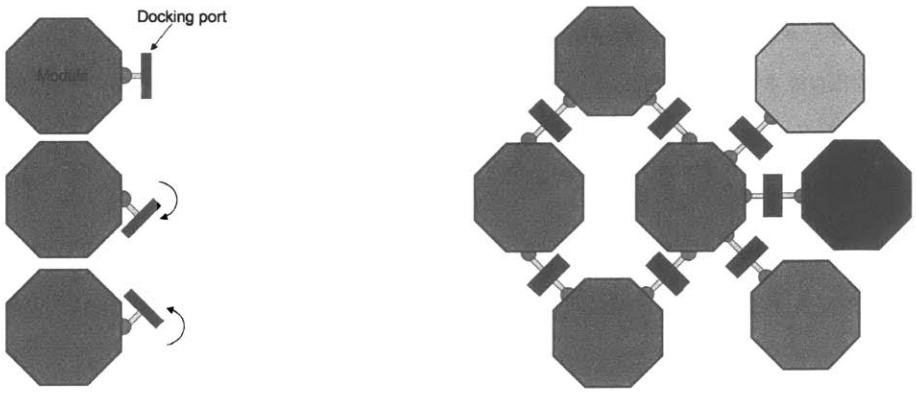

Figure 3-15: Large angular articulation of the docking port could be used to connect multiple modules.

Transfer thermal loads: This allows the modules to have a centralized thermal system, and thus separate systems are not needed on each module. This could be done by passing thermal fluid or by having contact between conductive materials.

Transfer fluid: The ability to transfer fuel, thermal fluid, etc. across docked modules.

Variable/multiple roll orientations: The docking ports can connect with any particular roll orientation. Thus, two modules could dock with one being upside down.

Scalability: The docking port size can be scaled up or down depending on the module size, while still leaving the ability for small and large docking ports to connect together. Having a fixed sized docking port could also satisfy scalability if multiple ports are used to connect larger modules (Figure 3-16).

System identification: A module is able to perform system checks on other modules either actively or passively. For example, one module could check the health of the other modules using accessible sensors. Another example is the ability for one module to mechanically excite other modules to find certain mass properties such mode shapes, frequencies, etc (Figure 3-17).

Attraction/repulsion for docking/undocking: It may be necessary for two docking ports to apply a substantial force during docking/undocking to connect/disconnect various connections (electrical, thermal, etc.). It may also be necessary for the two modules to be separated to a safe distance before thrusters begin firing. For these reasons, there must be a mechanical and/or electrical repulsive force to engage/break the various connections and propel the undocked module to a safe distance. Using a attractive/repulsive force other than the thrusters reduces the risk of plume impingement on sensitive payloads, and is a much more localized force to engage/break connections.

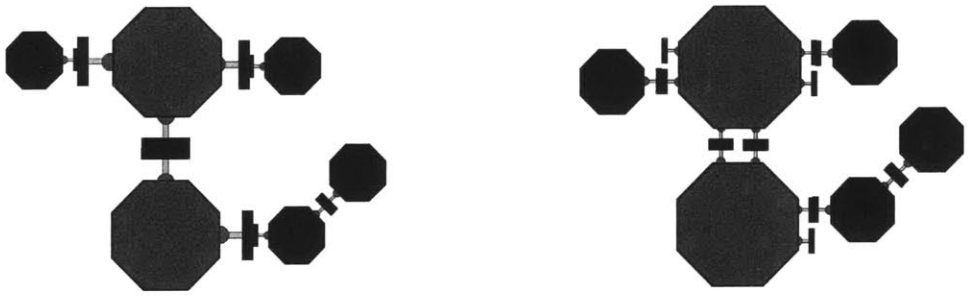

(a) (b)

Figure 3-16: Docking ports may either be scalable (a) or just a fixed size (b).

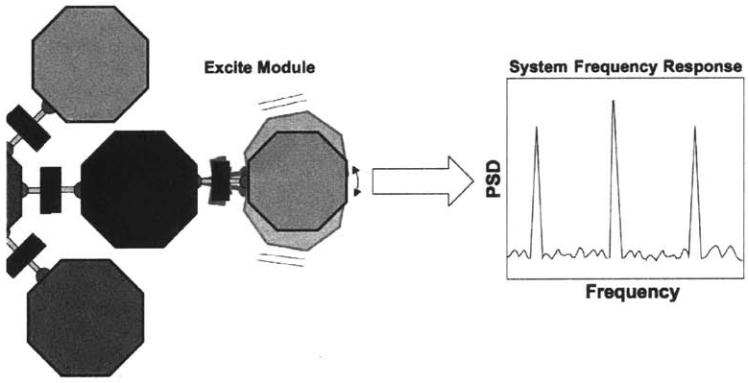

Figure 3-17: An example of how the docking port could be used to perform system identification with docked modules.

Active to passive docking: An active module has the ability to dock (thrusters, sensors, electrical power, etc.), while a passive module does not have this ability. For example, a passive module may not have thrusters or electrical power, so it is not capable of maneuvering and commanding itself to dock to other modules. However, if all docking

ports allow for active docking to passive ports, then an active module could maneuver itself to a passive module and connect to the passive port. Once the connection is made, the active module could transfer power and move the passive module. It may also have the ability to operate the passive docking mechanism. The active module could also have the ability to fully control the passive module using the connections available through the docking port. This could be very useful when assembling large structures in space. A few active modules could assemble many passive modules to form large space systems. This would reduce the number of components required on each module, and thus could reduce the overall mass and complexity.

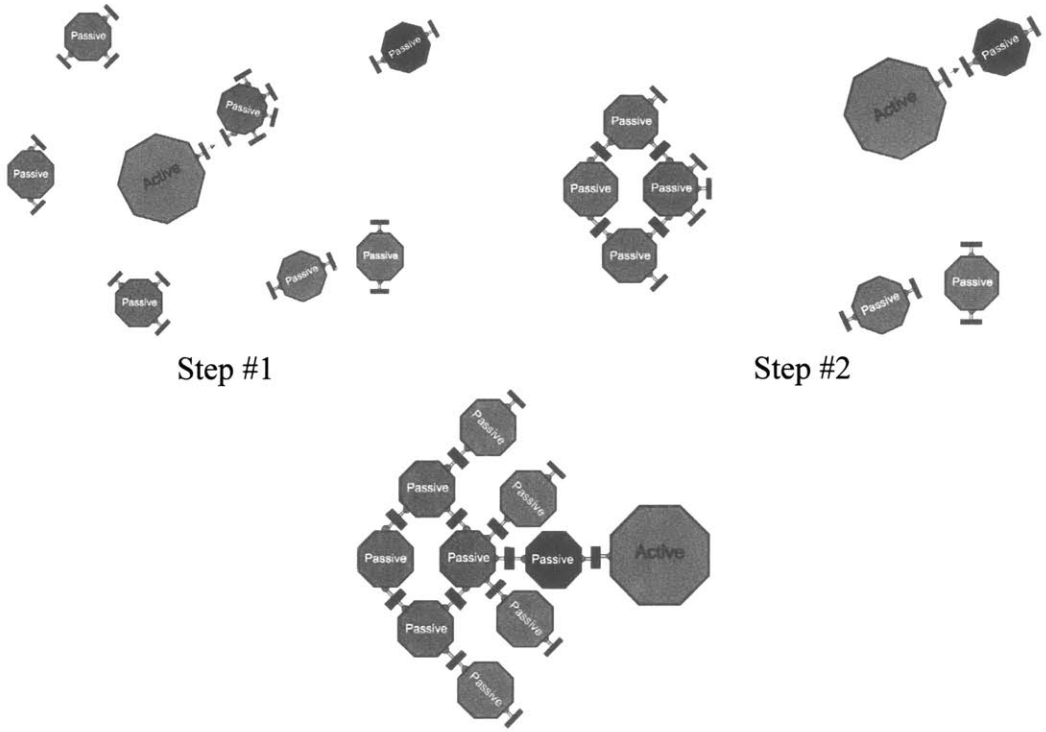

Figure 3-18: Active and passive docking ports

Variable damping and stiffness: This would allow for variable damping and stiffness between modules, while maintaining a rigid connection for data, power, etc. It would allow particular modules to be isolated from other modules, which would be useful for payloads that are sensitive to vibrations being generated on other modules. This could also be used to tune the dynamics of the entire system.

Reusability: The ability for the docking port to be operated multiple times during the mission life. Thus, there should not be any spring-loaded or explosive devices that can only be activated a small number of times.

This section developed a list of docking port capabilities for unmanned space missions where docking is needed to autonomously assemble space systems. The need for these various capabilities will largely depend upon the mission requirements and may be limited by cost. The next section develops general classifications for docking ports, so that any docking port can be generically described in terms of their distinctive features.

3.3. General Design Classifications

Docking ports can be classified as either central or peripheral. This distinction describes how two docking ports connect. A central design has locking components near the center of the docking port, while the peripheral design has them out and away from the center (Figure 3-19). The peripheral design is superior to the central design in the following ways:

Rigidity: By having the locking components far from the center the docking port has more leverage for a rigid connection.
Space: The peripheral design leaves more room for connections between modules on the contact surface.

The peripheral design is inferior to the central design in the following ways:

Entanglement: Because the locking components are outward and more exposed, there is more of a chance for entanglement during docking.
Volume: The peripheral designs are often times more bulky and occupy more physical space.

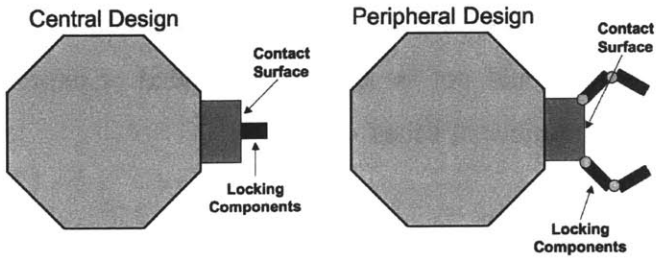

Figure 3-19: Examples of central (left) and peripheral designs (right).

Docking ports can be made universal by having a reconfigurable or inverse-symmetric design. A reconfigurable docking port has components that must be actuated before docking can occur. An example of such a port can be found in Figure 3-20. Before docking, the central core on one of the ports is retracted while the other is extended. Thus, a reconfiguration is needed before docking can occur. This may be undesirable since the initial step of retracting or extending the central core introduces an additional mode of failure to the docking procedure; if one of the cores is unable to fully retract, docking would likely be impossible. This type also requires a gearing mechanism or a linear actuator, which adds complexity. Lastly, this design requires that the docking port be long enough to contain the entire length of two cores, which increases its overall size.

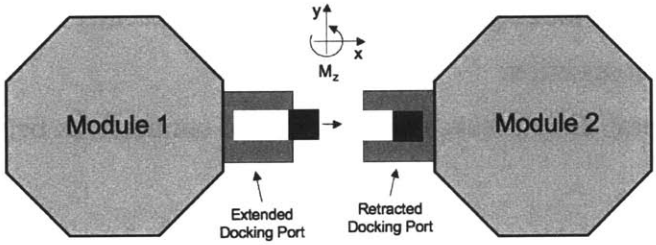

Figure 3-20: An example of a reconfigurable docking port design.

For an inverse-symmetric design, the docking port is made universal by having inverse symmetry across the face of the docking port. An example of such a design is shown in Figure 3-21, which uses a protruding pin and an entrance hole. The protruding pin is rigidly attached and thus does not extend or retract. This design is much more compact since nothing is being retracted. In addition, the protruding pin is off-axis, which provides more rotational rigidity (M_z). The schematic shows only one pin and hole, though

multiple pins could be used as long as the pin pattern is matched with holes through the center vertical axis of the docking port (Figure 3-22). The inverse symmetry through the vertical axis keeps the port universal. One advantage to adding pins is an increase in possible docking orientations. For example, the docking port has one docking orientation with one pin; similarly, there are two docking orientations with two pins. However, it should be noted that a turntable-type device could be used to rotate the port about the x-axis into the proper position before docking. This would allow the port to dock in *any* orientation in the y-z plane.

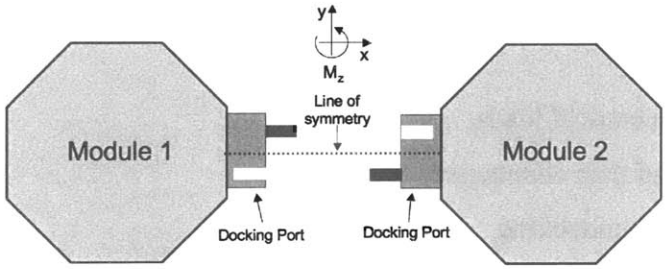

Figure 3-21: An example of an inverse-symmetric docking port design.

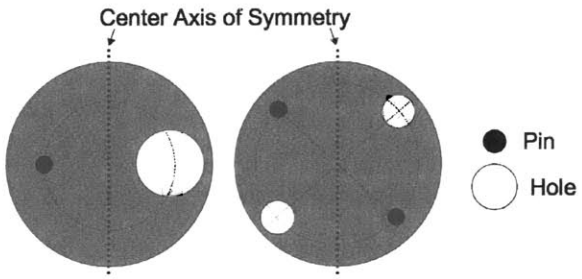

Figure 3-22: Various pin-hole combinations for an inverse-symmetric design.

There are many different types of both reconfigurable and inverse-symmetric designs, thus the above examples only serve to illustrate the overall idea behind the different classifications. The design classifications mentioned above: central; peripheral; reconfigurable and inverse-symmetric can be used to generalize many different docking port designs. When developing universal design concepts it was found that most designs fit into a combination of these classifications.

3.4. An Example of a Docking Port Design

The capabilities and classifications discussed in the previous sections were used to develop an actual functioning design. This docking port has been termed the Universal Docking Port (UDP). The following capabilities were considered as requirements for this design:

- Universal design
- Large docking tolerances
- Computer control
- Soft capture
- Transfer mechanical loads
- Electrical and data connection
- Repulsion for undocking
- Reusable

Refer to Section 3.1 for a description of these capabilities. Below is a list of the more practical requirements that constrained the final design:

Must be capable of mass production: A large number of docking ports were required. Thus, this should not be a very complex design that cannot be easily populated across all of the modules.

The over-all size should be minimized: The UDP should not be used only for demonstration purposes; it should be capable of being mounted on an actual vehicle, thus it should have a compact size. Also, if the mass of the docking port is small, then the penalty of modularity is less (Section 2.2).

Should not deplete the module batteries when operated: Since there is a limited amount of power available from the vehicle, the docking port should minimize the amount of

power consumed. Thus, the design should not require power after docking is complete (i.e. no steady state power).

Use off-the-shelf parts if possible: Minimize the amount of customized components, which typically improves performance and decreases fabrication time.

Figure 3-23 shows some of the key features of the final design; these features include a steel core and aluminum channel for an electromagnet coil, which acts as the soft capture mechanism and provides a repulsive force during undocking, two brass tabs to transfer electrical power, and an angled pin and chamfered hole to increase docking tolerances. Also, two counter rotating disks and a motor are used as part of the locking mechanism. Lastly, since wireless communication is used, a wire data connection is not needed. Table 3-1 summarizes the key specifications of the design, and Figure 3-24 and Figure 2-1 show the UDP used with two SPHERES and mounted on a single SWARM module, respectively.

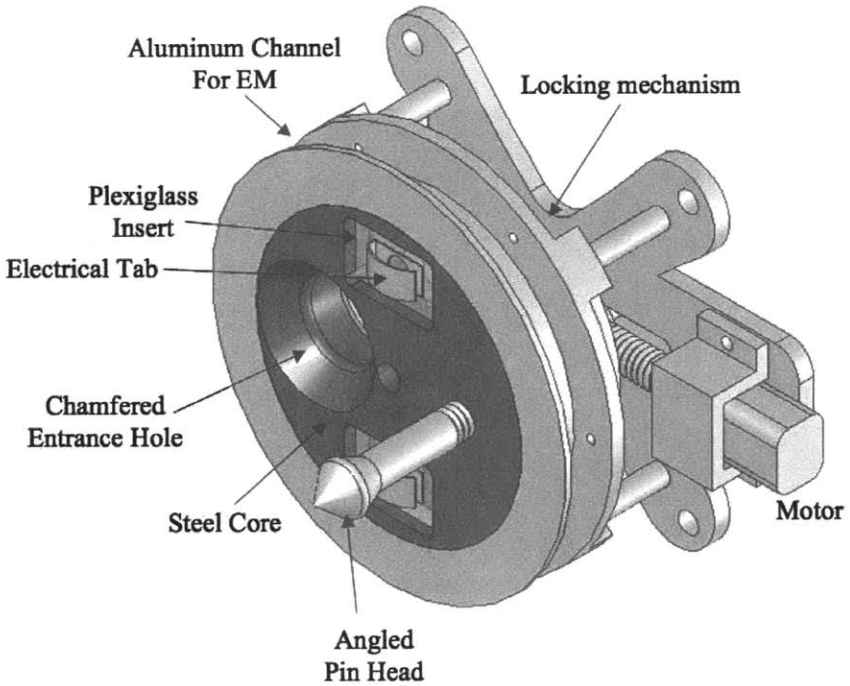

Figure 3-23: A CAD drawing of the UDP, showing some of the key features of the design.

Table 3-1: Key specifications for the UDP.

Dimensions	7.6 X 3.8 cm	**Electromagnet Wire**	28 gage copper EM wire
Protruding Pin Length	3.2 cm	**Electromagnet Resistance**	10 Ohms
Entrance Hole Diameter	1.5 cm	**Electromagnet Voltage**	24 Volts
Mass	0.45 kg	**Electromagnet Wire Turns**	~200 turns

This final UDP design required multiple iterations (Figure 3-25). Manufacturing considerations drove many of these iterations, since mass production was a requirement. A simple design was chosen with a minimum number of parts, which could be easily made given the available resources. For example, many of the parts were made on a two-dimensional water-jet. This machine is almost 100% automated, easy to use and cost effective for creating 2-dimensional parts. The remaining parts were made on either a lathe or mill, and when possible were simplified using jigs, and automated using computer programs.

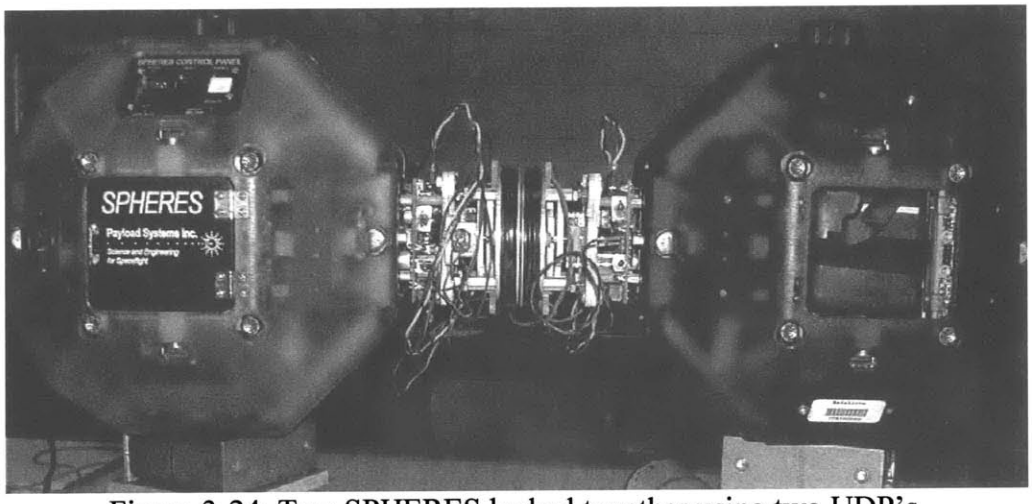

Figure 3-24: Two SPHERES locked together using two UDP's.

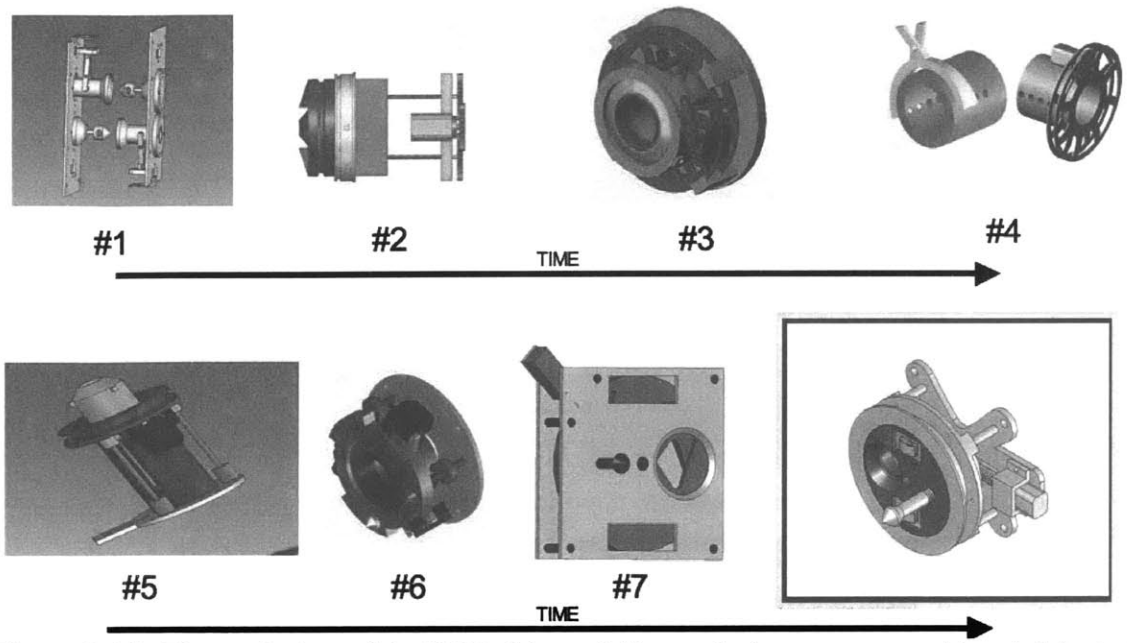

Figure 3-25: The evolution of the UDP. Many different designs were considered. Most of these designs were infeasible due to the complex machining required.

3.4.1. Concept of operation

The general docking and undocking operations of the UDP are summarized in Figure 3-26. The docking sequence is initiated once the metrology sensors have brought the modules within docking range. The computer gives commands via the Bluetooth communications network to enter docking mode, and the docking begins by activating the electromagnets on each of the UDP's. Contact sensors are used to determine when the UDP's are ready to be locked and when a successful lock has been achieved.

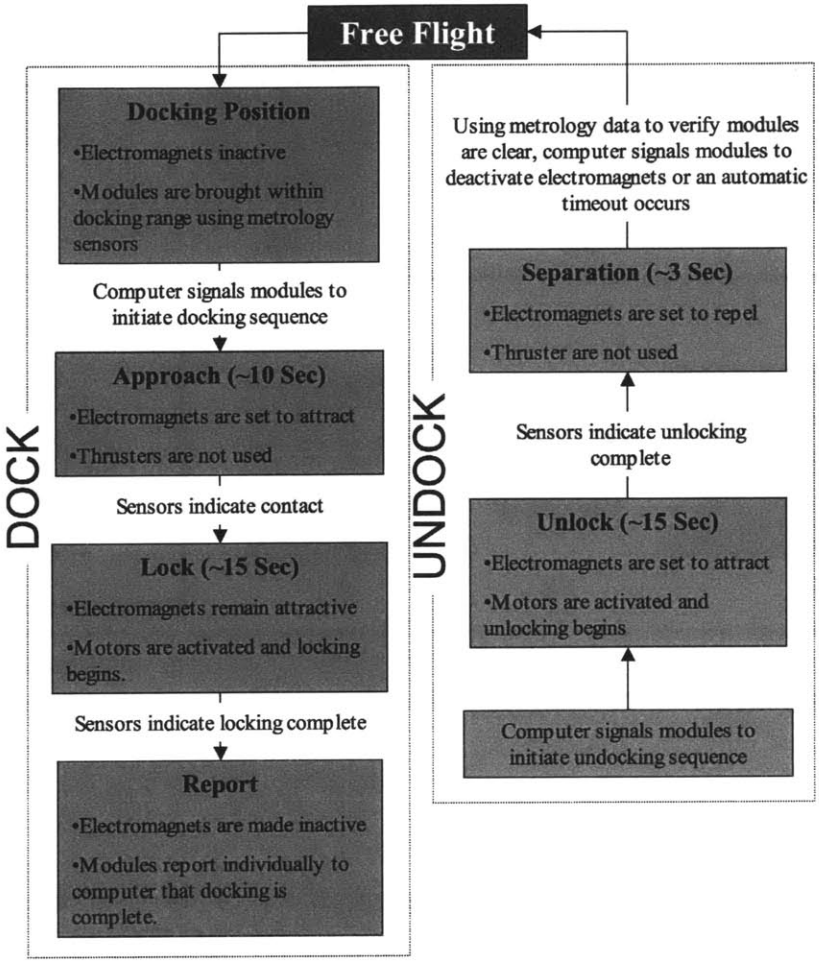

Figure 3-26: Flow-chart showing the docking and undocking sequence

3.4.2. Details of the design

This section provides the details of the UDP design, and is outlined by the capabilities discussed in Section 3.2.

Capability: Universal

The UDP is an inverse-symmetric and central based design (Section 3.3). The inverse-symmetry makes it universal.

Capability: Large docking tolerances

A chamfered entrance hole and angled protruding pin (Figure 3-23) are used to compensate for alignment error during docking

Capability: Computer control

A circuit board was designed to allow the computer to control the UDP (Figure 3-27 and Figure 3-28). It was designed to receive the high and low signals from sensors, execute computer commands and provide bus power to the UDP so it can be transferred through the brass tabs. Additionally, there are switches on the board so that the motor and electromagnet can be activated manually.

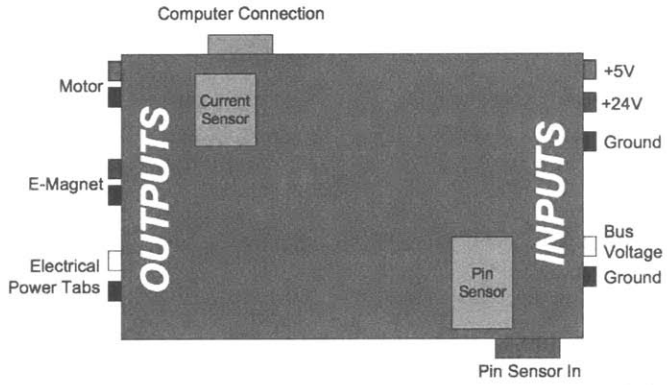

Figure 3-27: Input/output structure of the UDP circuit board.

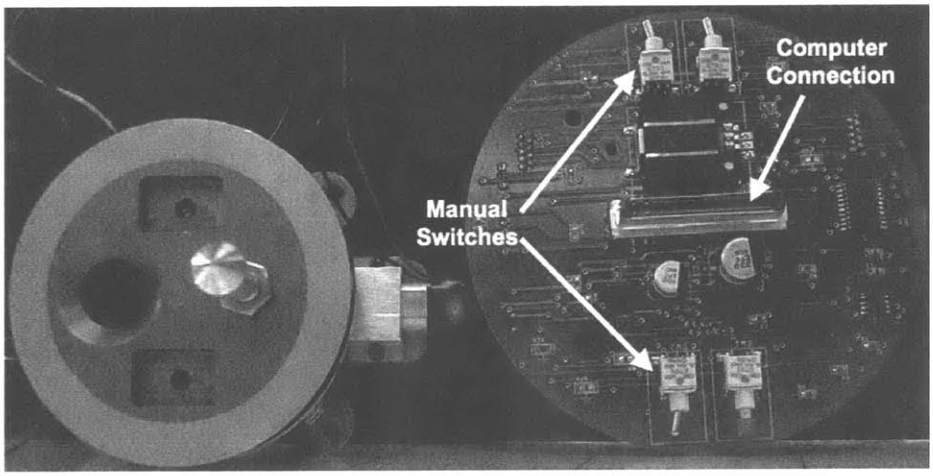

Figure 3-28: The actual UDP circuit board (right).

There is a contact and current sensor integrated into the circuit board. The contact sensor detects when the two modules have made contact, after which the UDP can be locked. To accomplish this, an interrupt-type optical sensor was used. Once the pin is sufficiently inside the entrance hole, the protruding pin blocks the sensor beam, which sends a low signal to the computer (Figure 3-29). A second sensor is used to detect when the locking mechanism is completely open and closed. When the motor has stalled, the sensor detects a current spike, and relays a high signal to the computer; this signifies that the UDP is locked, or that it is fully open.

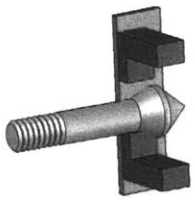

Figure 3-29: The pin blocks the sensor. The sensor is mounted directly behind the second rotating ring (Figure 3-30).

The circuit board had two different versions. The first version sent and received high/low commands between the circuit card and computer directly using a 10-pin connector. A high signal is considered anything above 3 volts, while a low signal is anything below 1 volt. The following signals are *sent* from the computer to the circuit (each bullet point is a separate data line and the voltage signal is in parenthesis):

- Motor on/off (high/low) – Computer control
- Motor on/off (high/low) – Manual override
- Motor direction (high/low) – Computer control
- Motor direction (high/low) – Manual override
- Electromagnet direction (high/low) - Computer control
- Electromagnet on/off (high/low) – Computer control

The computer *receives* the following signals from the circuit:

- Current sensor signal, which designates when the docking port is fully locked/unlocked (high)
- Ground
- Contact sensor signal, which designates when the two docking ports have made contact or are apart (low/high)
- Ground

The second version uses a PIC chip on the circuit board, which utilizes a standard protocol to communicate serially with the computer. The computer gives the PIC a single command, and the PIC chip executes the programmed docking sequence locally without any other commands from the computer.

Capability: Soft capture

The electromagnet provides the soft capture. The electromagnet force helps with final alignment and is used to hold the modules together during locking. The front of the UDP is made of steel with a concentric aluminum channel. The steel enhances the magnetic field, and the channel houses the wrappings of coated copper wire that form the electromagnet. The two disadvantages of using an electromagnet are an increase in weight from the steel core and the additional power consumption when the electromagnet is activated. It should be noted that an entirely aluminum core was tested, but the magnetic field was not sufficient.

Capability: Transfer mechanical loads

To mechanically connect the modules, a locking mechanism is required. This mechanism uses two counter-rotating disks, which are used to both pinch and wedge the protruding pin (Figure 3-30). Once each of the pins has been inserted into the opposing UDP, the motor is activated, which begins the locking process. The ramp on the back of the pin's head creates a wedge effect, which draws the two modules together and forms a tight mechanical lock. The disks are counter-rotated by pulling a pin along a curved slot (Figure 3-31). The two disks are identical, but one is flipped, so they counter rotate equally

in opposite directions. Figure 3-32 shows how a threaded motor rod is used to translate the pin along the curved slot. By using a threaded motor shaft, the disks are locked when the motor is turned off.

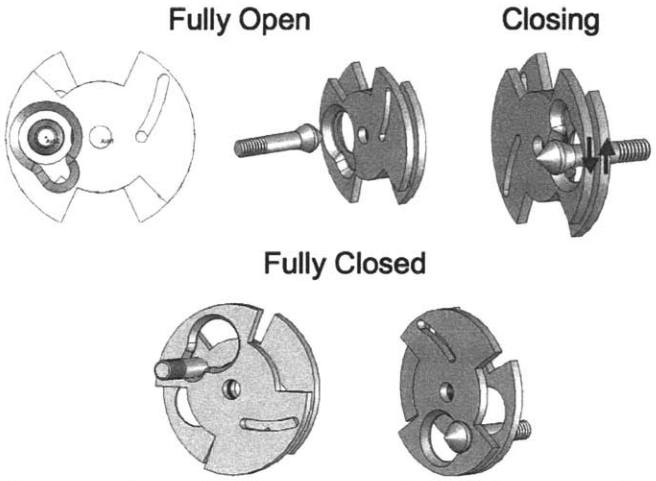

Figure 3-30: This illustrates how the counter-rotating disks are used to lock the pin. The pin is both pinched and wedged.

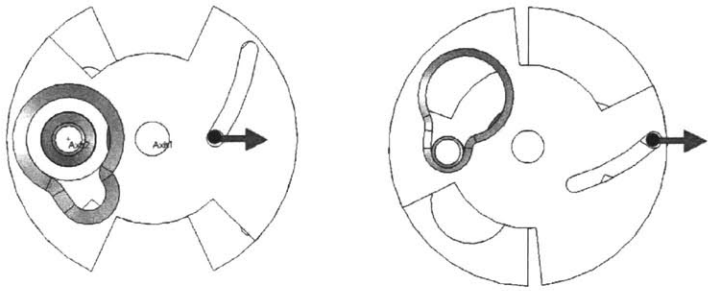

Figure 3-31: The curved slot and pin are used to counter-rotate the disks.

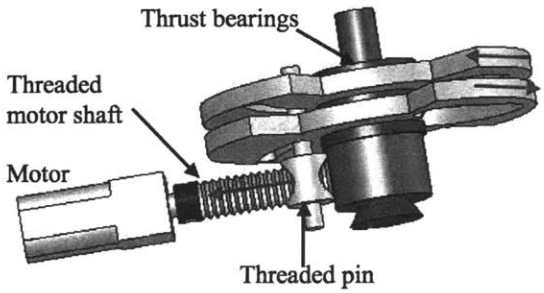

Figure 3-32: The motor is used to move a pin through the curved slots in the disk for counter-rotation.

Capability: Electrical and data connection

Two brass tabs are used to pass bus voltage through the UDP (Figure 3-23). The top tab is the positive and the bottom is the negative. When the two docking UDP's are connected, the opposing tabs create a closed electrical connection, and electricity can be passed between the modules. Multiple bus voltages were required, thus a voltage regulator card was necessary in each module to provide the other voltages. The need for this additional power-card is considered a drawback of the decision to pass a single bus voltage through the UDP, versus having multiple voltages directly passed. It should be noted that the power tabs are mounted on a plexiglass insert to isolate the electrical connection from the surrounding steel. The wires from the power tabs need to be fed through the UDP from the front to the back, so they can be connected to the UDP card (Figure 3-33). Lastly, Bluetooth® wireless units provide wireless communication between each module and the central computer module, thus a physical data connection was not needed.

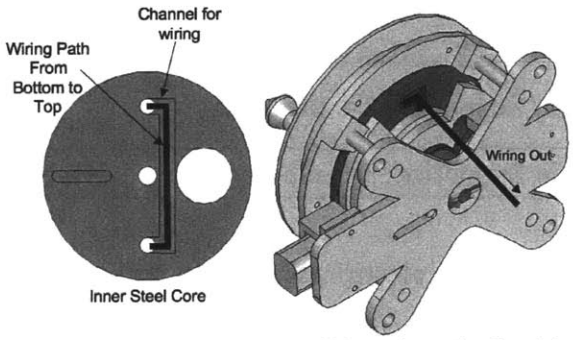

Figure 3-33: The routing of the electrical wiring.

Capability: Repulsive force for undocking

The two modules are repelled smoothly during undocking by switching the polarity on one of the electromagnets. However, there is not a substantial force generated by the electromagnet, so it is unlikely that this method could be used to disconnect physical data connections, etc.

Capability: Reusability

The UDP is fully reusable because it uses an electrical motor, threaded rod and counter-rotating disks for locking and unlocking.

3.4.3. Testing and validation

Tests showed that two modules can be commanded to autonomously dock and undock. Table 3-2 summarizes some of the tests performed on the UDP. The "Weight Supported" results are not maximum values, but rather the operational values; it is likely that the UDP could support much larger mechanical loads. Lastly, tests showed that two UDP's can be locked together and then pass electrical current. However, while the ability for one module to charge the batteries of another module was included in the design, it has not been tested.

Table 3-2: Summary of UDP Tests

Maximum Docking Range	~10 cm
Time for Final Capture (EM pull)	2-5 seconds
Time to Lock	15 seconds
Weight Supported, Cantilevered	110 N, 25 cm lever arm
Weight Supported, Tensile	110 N

The effectiveness of the electromagnet was determined by measuring the force between two docking ports with active electromagnets. The test setup consisted of two docking ports, one on a mass scale and another placed directly overhead on a vertical track. The scale measurement was recorded as the vertical distance was increased. The results are shown in Figure 3-34 through Figure 3-36. As expected, the force drops off very quickly with axial distance. When both electromagnets are activated, the force is essentially zero for distances greater than 4 cm. From Figure 3-34 it can be seen that by doubling the voltage, the maximum force increased by more than a factor of four. Figure 3-35 shows that the force generated is roughly four times less when only one electromagnet is activated, and that the repulsive force is nearly ten times less than the attractive force.

Lastly, Figure 3-36 shows that the attractive force decreases with time. This is likely due to resistive heating, since the magnet is passively air-cooled. Meaning, the magnet is cooled by the ambient air currents, and does not have an active cooling system.

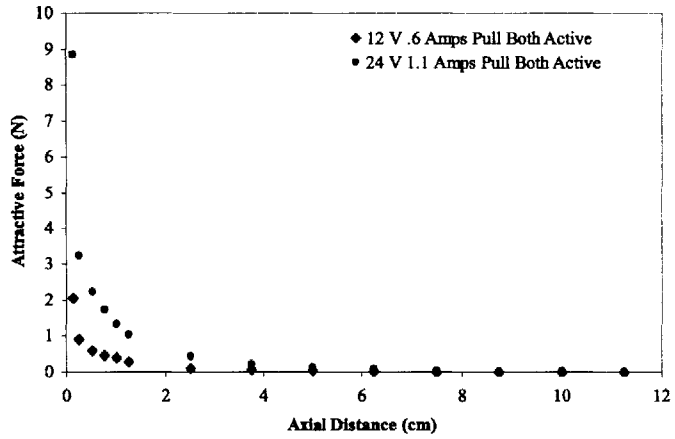

Figure 3-34: Attractive force versus axial distance for two active electromagnets.

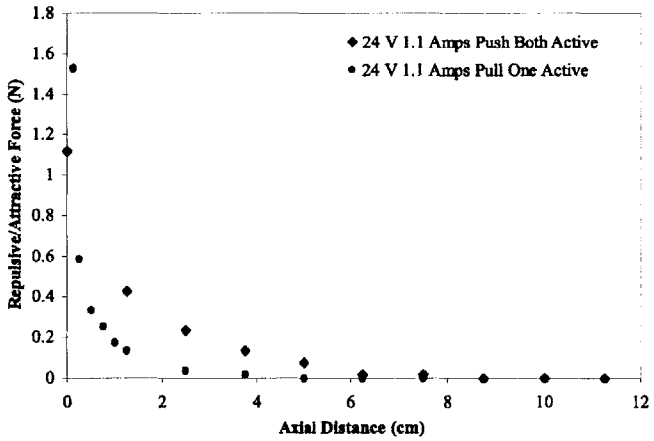

Figure 3-35: Attractive force versus axial distance with one active electromagnet, and the repulsive force versus axial distance for two active electromagnets.

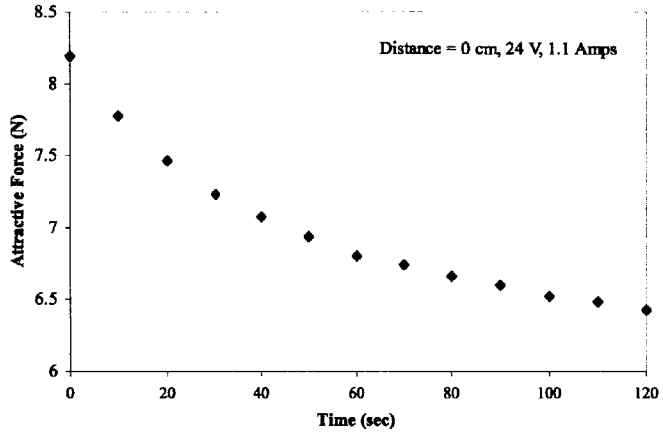

Figure 3-36: Attractive force versus time with near zero separation between the two activated docking ports.

3.5. Summary

This chapter presented a brief history of docking ports, and then generalized to form a list of docking port capabilities for unmanned space missions. Classifications were then developed, so that any docking port can be described in terms of their distinctive features. These classifications are: central, peripheral, reconfigurable, and inverse-symmetric. These capabilities and classifications were then applied to an actual functioning design, called the Universal Docking Port (UDP). This design was discussed in detail, and various test results were presented. The UDP has an inverse-symmetric and universal design, which is capable of passing mechanical and electrical loads between modules. Supporting electronics allow for computer control of the UDP, and the electromagnet provides an attractive force for a soft capture for docking and a repulsive force for undocking.

Complex rendezvous and docking maneuvers will require advancements in both docking port and sensor technology. The sensor provides state information to guide the vehicle along a docking trajectory. To this end, the next chapter describes the development of an optical docking sensor called the Miniature Video Docking Sensor (MVDS), which is used to determine the six relative degrees of freedom of two docking vehicles.

Chapter 4. State Determination using the Miniature Video Docking Sensor

When autonomously docking two vehicles, it is necessary to know the relative position, attitude, and angular rates of each vehicle. This information is referred to as the relative states. Docking algorithms use this state information to guide the vehicle along a trajectory, which may be optimized for minimal time or fuel. The docking algorithms heavily rely on accurate state information when determining a trajectory, and thus a high-fidelity state measurement is essential for any docking maneuver. This chapter will describe the hardware and algorithm development for a Miniature Video Docking Sensor (MVDS), which can be used to determine the six relative degrees-of-freedom (DOF) state information of two docking vehicles.

4.1. Overview of the MVDS

The MVDS is a space traceable optical docking sensor, which was demonstrated using the SPHERES spacecraft testbed [6]. This testbed consists of a micro-satellite, or SPHERE, which can autonomously control its position and attitude using CO_2-based thrusters and on-board gyroscopes. The testbed can be operated on an air-table in a 1-g laboratory environment, in a reduced gravity research aircraft or inside the International Space Station (ISS). The current design of the MVDS is only rated for the 1-g laboratory environment.

The MVDS determines the six relative DOF between the SPHERE and a fixed docking port ("Mothership"), and is used for fully autonomous docking and undocking (Figure 4-1). The SPHERE and Mothership are referred to as the chase vehicle and target, respectively. It should be noted that this system would also work with two floating vehicles. The MVDS uses a CCD-based camera on the target docking port to detect three

LED's on the SPHERE. An Extended Kalman Filter (EKF) is used as part of the state estimator. The SPHERE is initially brought into the operating range of the sensor using the SPHERE's existing ultrasonic global metrology system. Once inside the operating range, the MVDS is activated and is used to control the SPHERE. Currently, the MVDS computes the states of the SPHERE using Matlab code on a desktop computer and sends this information via radio communication to the SPHERE with an update rate of approximately 6 Hz. The SPHERE uses this information along with onboard algorithms to dock to the target (Figure 4-2).

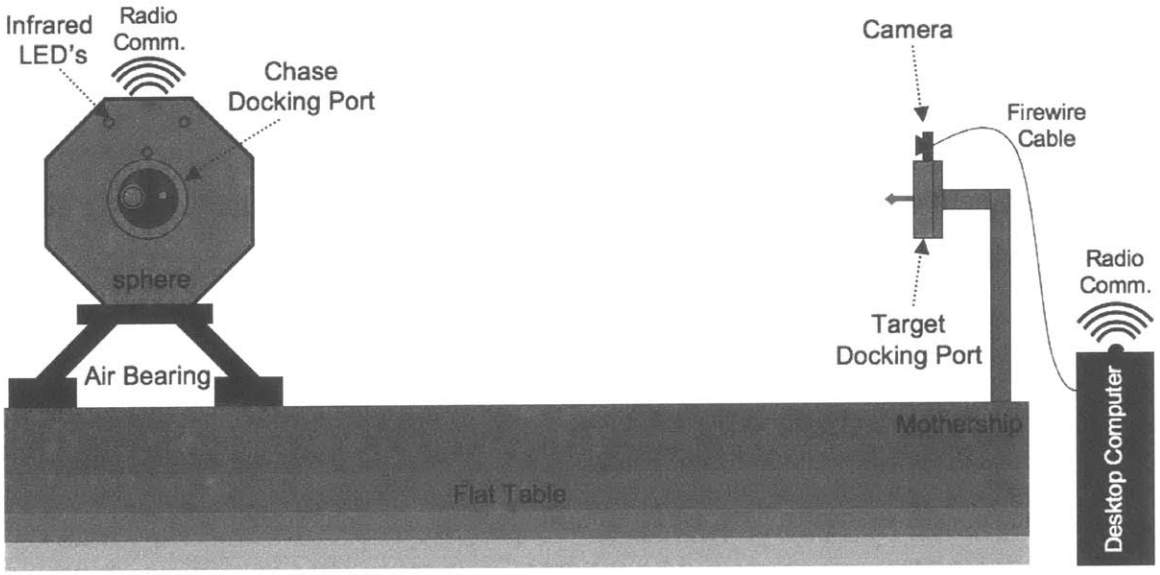

Figure 4-1: The test setup.

The concept of MVDS was derived from a large body of work done at NASA Marshall Space Flight Center (MSFC) with the Advanced Video Guidance Sensor (AVGS). The concepts of the AVGS began with a Martin Marietta study, which compared three different video-based techniques for automated spacecraft docking. The study concluded that a three spot target held the most promise, and thus it was further developed through the present [26]. AVGS technology has flown on the Space Shuttle (STS 87) and as part of the DART mission [27], [28].

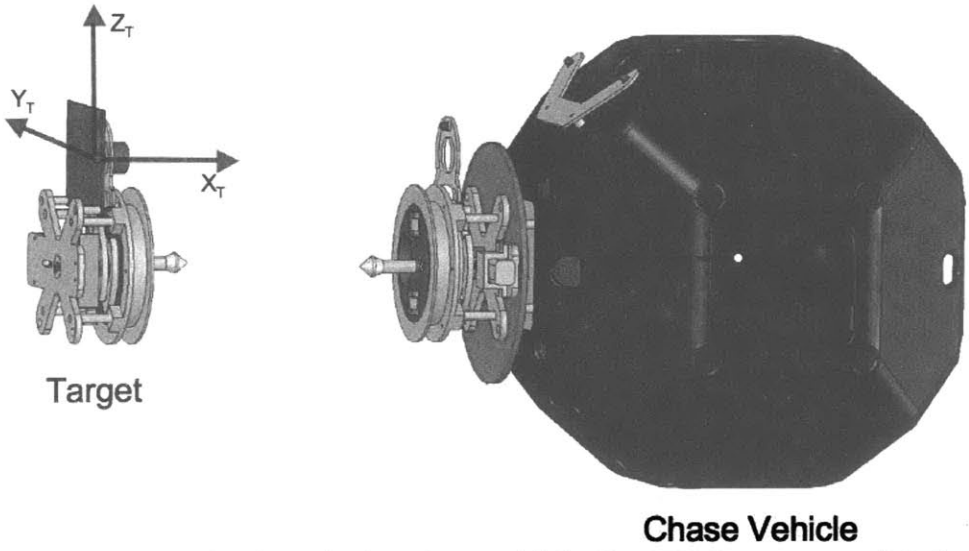

Figure 4-2: The objective is to dock a chase vehicle (SPHERE) to a target (Mothership).

4.2. Hardware

The MVDS hardware currently consists of a CCD-based digital video camera, three infrared LED's, and a desktop computer. Radio communication is used to send the relative state information from a desktop computer to the chase vehicle. This section will discuss each of these hardware components in detail, including some of the theory required to use the camera-LED system as a measuring device.

4.2.1. Using a camera as a measuring device

As will be discussed in Section 4.3, the EKF compares actual to predicted measurements. These measurements must be directly related to the relative states of the vehicle. The camera is used to image three LED's that are placed at known locations on the vehicle. The row and column location of the centroid for each LED as seen by the CCD is the actual measurement. The predicted measurement is determined using the current state estimate, a basic optical model of the camera, and by knowing the location of the LED's on the SPHERE.

A CCD-based digital video camera produces a 2D grayscale image at a fixed frame rate (Figure 4-3). A picture and the specifications of the camera can be found in Figure 4-4 and Table 4-1, respectively.

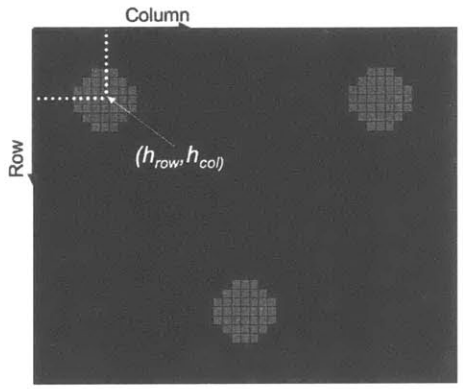

Figure 4-3: The CCD-based camera produces a 2D grayscale image similar to the illustration shown above. The row and column location of the centroid for each LED must be determined (h_{row}, h_{col}).

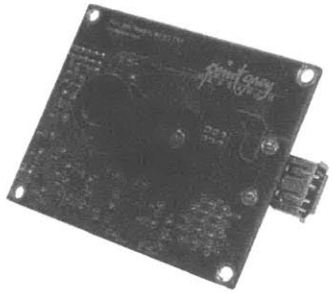

Figure 4-4: The camera used for the MVDS. The dimensions are 2.5 by 2 inches.

Table 4-1: The camera specifications.

Manufacturer/Model	Point Grey/ Dragonfly
Imaging Device	1/3'' Sony CCD
Resolution	480x640
Colors	Grayscale
Connector	6-pin IEEE-1394 (FireWire)
Dimensions	2.5'' X 2''
Frame Rate	30 fps
Pixel Size (P)	7.4e-6 m
Field of View	50 degrees, full cone
Focal Length (*f*)	6 mm

Figure 4-5-a shows the basic theory used to determine range information from the camera image. The following relationship for a thin lens is used:

$$\frac{1}{S_o} + \frac{1}{S_i} = \frac{1}{f} \tag{4-1}$$

where f is the focal length of the camera lens. Using the similar triangles shown in Figure 4-5-a it can be shown that:

$$Y_i = \left(\frac{S_i}{S_o}\right) \cdot Y_o \tag{4-2}$$

The objective is to calculate the center of the illumination spot on the CCD (h_{row}, h_{col}) for a given position of the LED in the target coordinate system ${}^{T}(R_x, R_y, R_z)$. To this end, Equation 4-2 and Figure 4-5-b can be used to form the following relationship:

$$\begin{bmatrix} h_{row} \\ h_{col} \end{bmatrix} = C \cdot \begin{bmatrix} \left(\frac{\kappa}{R_x}\right) \cdot R_z \\ \left(\frac{\kappa}{R_x}\right) \cdot R_y \end{bmatrix} \tag{4-3}$$

where C is the inverse of the pixel size (P), given in pixels per meter (Table 4-1).

By comparing Figure 4-5-a and Figure 4-5-b, it can be seen that it was assumed that the image distance (S_i) is always equal to the distance between the lens and the CCD (κ). However, the image distance is continually changing as the object distance is varied, and since the camera has a fixed simple lens, this assumption can only be valid for particular object locations. Section 4.4.2 will address this issue in depth.

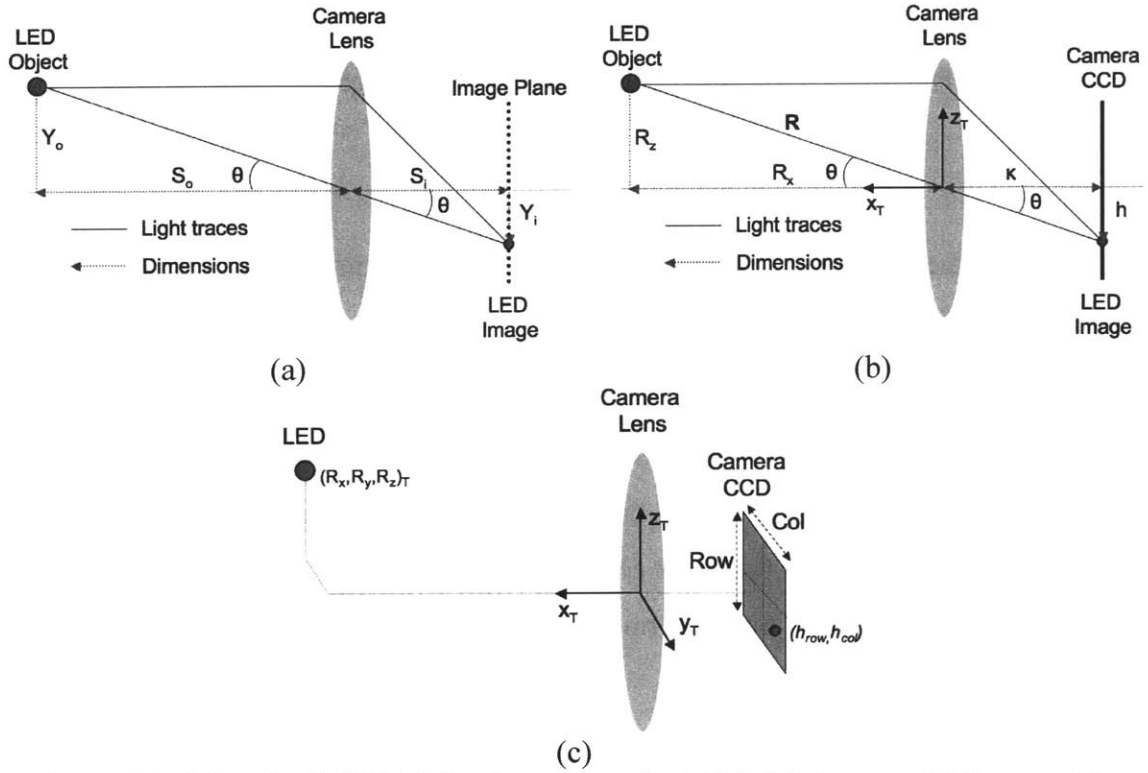

Figure 4-5: (a) A single LED being imaged on the CCD. (b) Same as (a) but uses the naming convention used in this study. (c) The LED location $(R_x, R_y, R_z)_T$ is converted to a the row and column location on the CCD (h_{row}, h_{col}).

4.2.2. Selecting the type and location of the LED's

The type of LED is not important, though it must produce an intensity that can be detected by the camera and analyzed by the computer. Infrared LED's were chosen for the MVDS so that the camera could filter out the ambient light while clearly detecting the LED's. A glass filter that blocks out visible light was placed in front of the camera lens to aid in the filtering process. There are many ways to generate three illuminated points, though this active LED system seemed to be the easiest to implement.

Range and angle sensitivity is the ability of the sensor to determine small changes in the relative range and angle between the chase and target docking ports. As will be discussed in Section 4.4, the sensitivity strongly depends on the resolution of the camera's CCD and the placement of the LED's. Because of this, a high-resolution camera is desirable, and the positions of the LED's must be considered. Also, particular LED placements will yield multiple solutions. The configuration of the LED's used for the

MVDS is shown in Figure 4-6. Being sensitive in range means that small changes in the object distance (R_x) can be detected. This is equivalent to the spot on the CCD moving across many pixels for a small change in the vehicle's range. From Equation 4-2 and Figure 4-5-c it can be seen that this sensitivity is obtained by making R_y as large as possible. Thus, the following relationship exists for range sensitivity (Figure 4-6):

$$\text{Range Sensitivity} \sim D_1$$

Angular sensitivity is achieved by having the image of LED #1 move across many pixels on the CCD for small changes in the angle of the vehicle. Thus:

$$\text{Angular Sensitivity} \sim D_2$$

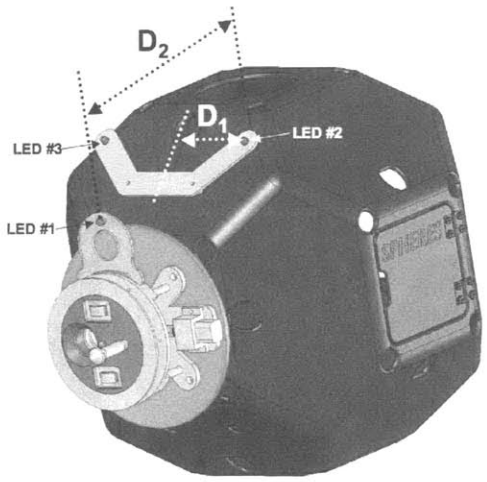

Figure 4-6: The dimensions that are used to determine the relationship between the LED placement and measurement sensitivity.

As mentioned earlier, there are multiple solutions because only three LED's are used. Meaning, there are multiple spacecraft orientations that would produce the same image on the CCD. This is because any three points form a plane; this would not be a problem if four or more points were used (though they should not all lie in a plane). The three-point redundancies are less of a problem in 2D since the possible orientations are more restricted. A few of the most common redundancy problems will be discussed, though reference [29] presents a much more detailed discussion of this topic. As shown in Figure 4-7, there are multiple solutions for particular orientations when a vector normal to

the camera lens is parallel and aligned to a normal vector to the plane formed by the three LED's. If these conditions exist, it is not possible to determine the sign of θ. Figure 4-8 and Figure 4-9 show how multiple solutions can be removed for particular orientations by relocating one LED.

When practically designing against these redundant solutions, one must first define the operating conditions of the sensor. For the present application, the camera will never fly above the target as shown in Figure 4-7, thus the configuration of the three LED's as shown in Figure 4-6 is sufficient.

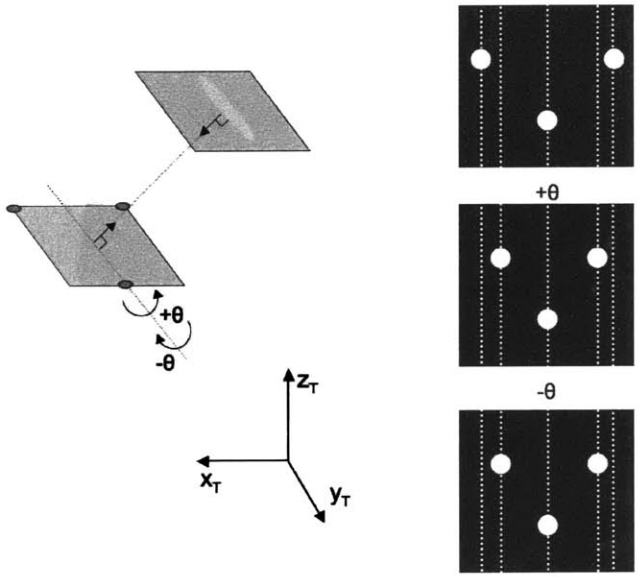

Figure 4-7: Three LED's (left) imaged on the CCD (right). Multiple solutions will exist for particular orientations whenever only three LED's are used. The vertical dashed lines on the right are shown only for reference, and are not part of the actual CCD image.

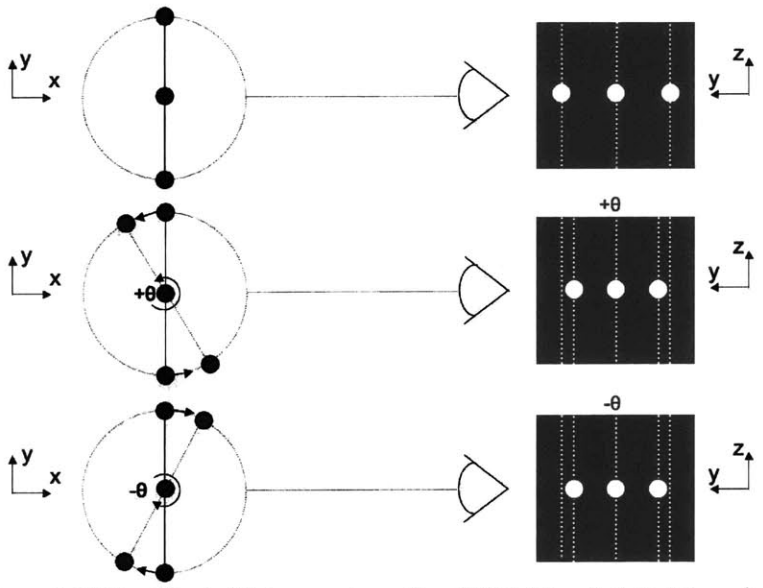

Figure 4-8: Three LED's (far left) imaged on the CCD (far right). The viewpoint of the camera is shown in the center. The image depicts an equal angle change in opposite directions. This is an example of when multiple solutions exist. The vertical dashed lines on the right are shown only for reference, and are not part of the actual CCD image.

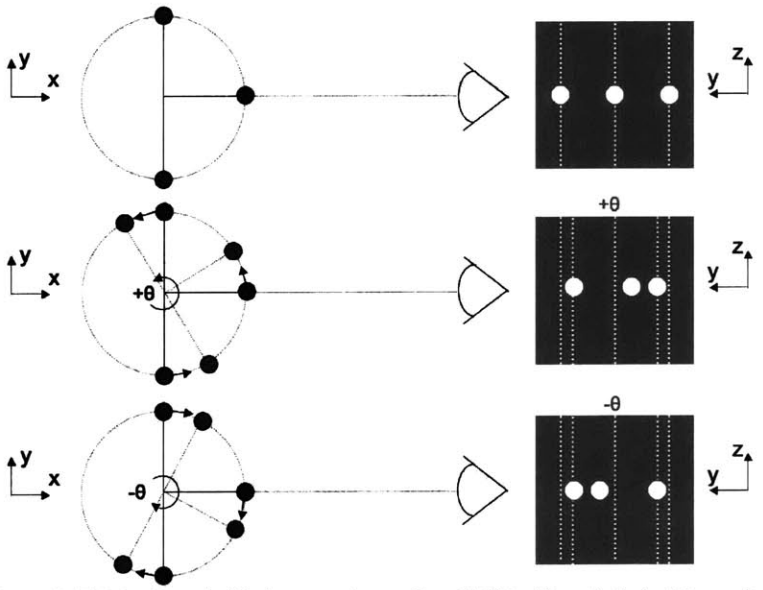

Figure 4-9: Three LED's (far left) imaged on the CCD (far right). The viewpoint of the camera is shown in the center. The image depicts three LED's rotated by an equal angle in opposite directions. Multiple solutions can be eliminated if the center LED is placed out in front in the x-direction. However, this only eliminates the multiple solutions for particular viewpoints. The vertical dashed lines on the right are shown only for reference, and are not part of the actual CCD image.

4.3. Algorithms

This section describes in detail the algorithms used in the MVDS. The first algorithm seeks to find the location of the center for each LED on the CCD. The second algorithm is an Extended Kalman Filter, which finds the best estimate of the state.

4.3.1. Finding the centers of the LED's on the CCD

The camera is a discrete measuring device that uses an array of over 300,000 pixels to measure the intensity of light as images are focused onto the CCD. Each pixel measures light intensity using a scale from 0 to 256. When the computer triggers the camera to capture an image, the entire 480x640 matrix of intensity values is dumped into the computer buffer for analysis. This process is repeated as quickly as possible, while mostly being limited by the computation speed of the computer.

Each LED illuminates a number of pixels to form a circular spot (Figure 4-10). An algorithm is required to determine the center of each LED (h_{row}, h_{column}) within the CCD matrix. Many different methods have been developed to perform this task, and these are commonly used in star-tracking algorithms.

As will be discussed later, built-in Matlab functions were used to determine the center of each LED on the CCD. However, this section will discuss a possible method for finding the center of an illumination spot if the algorithm was not written in an interpretive language such as Matlab. The basic idea is shown in Figure 4-10 and Figure 4-11. This method ran at approximately 15 Hz when written in C. It works by assuming that the illumination spot has a circular shape. The algorithm scans each of the pixels until an intensity value above a pre-set threshold is found. Once such a pixel is found, the algorithm first checks to make sure that the found pixel has not already been analyzed. Ensuring that the found pixel does not reside anywhere inside any of the previously found LED circles performs this check. If it has not been analyzed, then the center and the largest radius of the circle are determined.

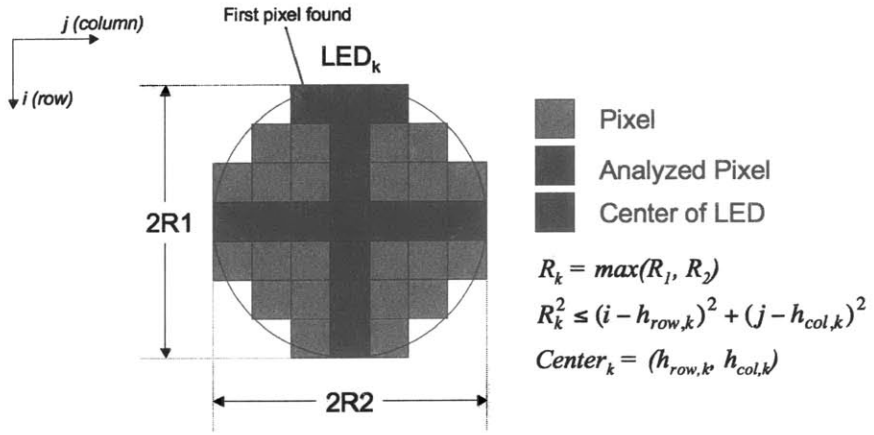

Figure 4-10: Determining the center of the LED spot on the CCD.

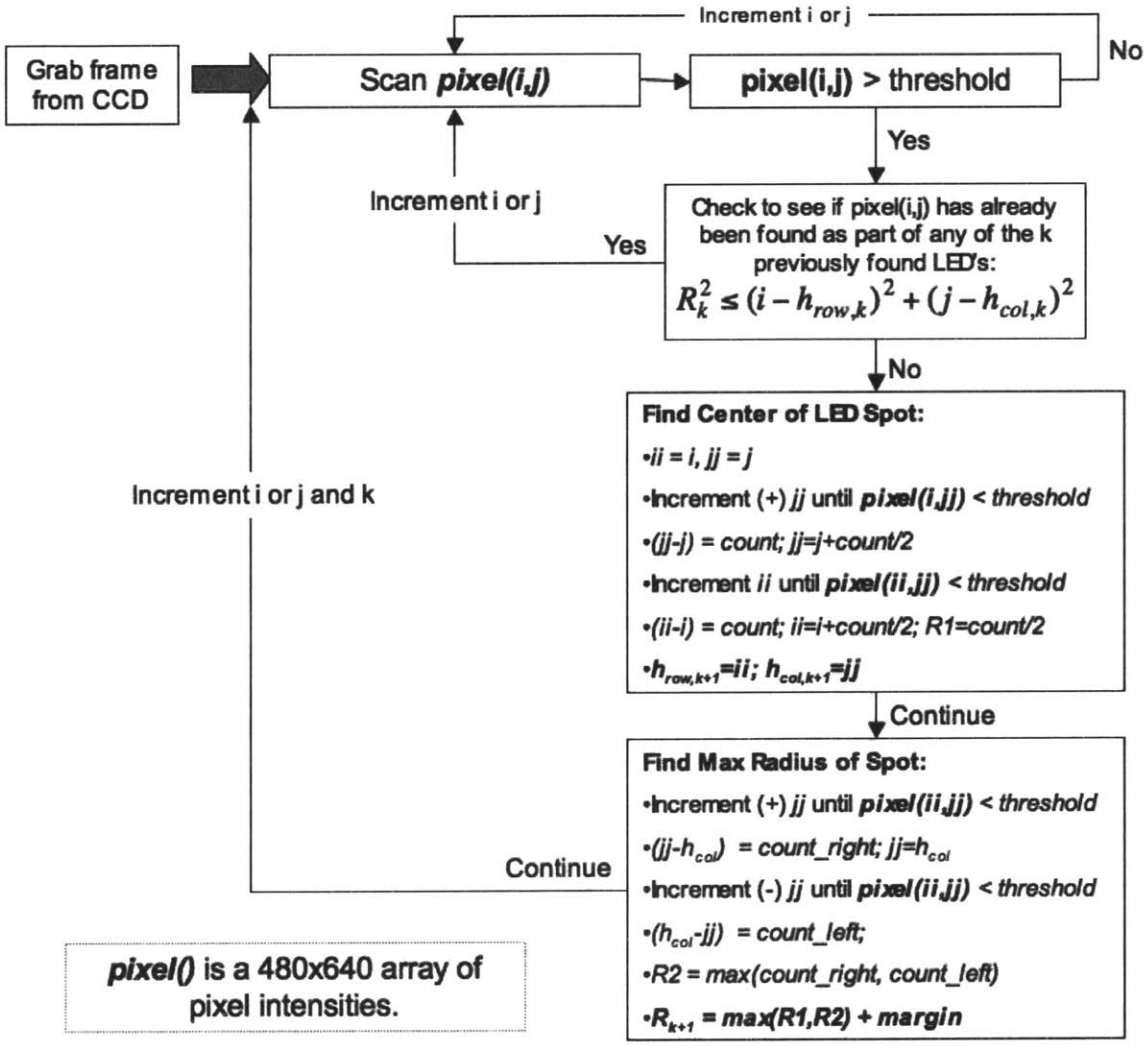

Figure 4-11: The algorithm used to find the center of the LED spots on the CCD.

4.3.2. A continuous-discrete Extended Kalman Filter

The six relative DOF of the docking vehicle are determined using a continuous-discrete Extended Kalman Filter. A system with continuous dynamics and discrete measurements can be modeled mathematically as:

$$\dot{\boldsymbol{x}} = f[\boldsymbol{x}(t),\boldsymbol{u}(t)] + \boldsymbol{\varepsilon}'(t) \qquad \boldsymbol{\varepsilon}'(t) \sim N[0,\boldsymbol{Q}(t)] \qquad 4\text{-}4$$

$$z_k = \boldsymbol{h}_k[\boldsymbol{x}(t_k)] + \boldsymbol{\varepsilon}_k \qquad \boldsymbol{\varepsilon}_k \sim N[0,\boldsymbol{R}_k] \qquad 4\text{-}5$$

This non-linear model is for a time-varying system with dynamics $f[\boldsymbol{x}(t),\boldsymbol{u}(t)]$, with sets of measurements z_k made at discrete times t_k [30]. The vectors $\boldsymbol{\varepsilon}'(t)$ and $\boldsymbol{\varepsilon}_k = \boldsymbol{\varepsilon}_k(t_k)$ are independent zero-mean white noise processes with covariance $\boldsymbol{Q}(t)$ and $\boldsymbol{R}_k$, respectively.

The EKF uses both the system dynamics (Equation 4-4) and measurements (Equation 4-5) to determine the best estimate of the state vector, $\hat{\boldsymbol{x}}(t)$. The system dynamics are used to propagate the states by an increment in time, while the measurements are used to adjust the state propagation to yield a more accurate estimate. Figure 4-12 shows schematically how the states are propagated and updated for each increment of time.

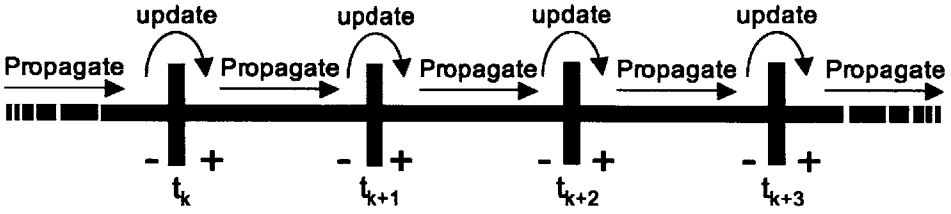

Figure 4-12: The EKF propagates using the system dynamics and updates using the CCD measurements.

The following equations are used to "propagate" the state estimate and covariance:

$$\dot{\hat{\boldsymbol{x}}} = f[\hat{\boldsymbol{x}}(t),\boldsymbol{u}(t)] \qquad 4\text{-}6$$

$$\dot{\boldsymbol{P}}(t) = \boldsymbol{F}[\hat{\boldsymbol{x}}(t)]\boldsymbol{P}(t) + \boldsymbol{P}(t)\boldsymbol{F}^T[\hat{\boldsymbol{x}}(t)] + \boldsymbol{Q}(t) \qquad 4\text{-}7$$

The measurements are used to "update" the state vector and covariance using the following equations:

$$\hat{\boldsymbol{x}}_k^{(+)} = \hat{\boldsymbol{x}}_k^{(-)} + \boldsymbol{K}_k\left[z_k - \boldsymbol{h}_k(\hat{\boldsymbol{x}}_k^{(-)})\right] \tag{4-8}$$

$$\boldsymbol{P}_k^{(+)} = \left[\boldsymbol{I} - \boldsymbol{K}_k\boldsymbol{H}_k(\hat{\boldsymbol{x}}_k^{(-)})\right]\boldsymbol{P}_k^{(-)} \tag{4-9}$$

$$\boldsymbol{K}_k = \boldsymbol{P}_k^{(-)}\boldsymbol{H}_k^T(\hat{\boldsymbol{x}}_k^{(-)})\left[\boldsymbol{H}_k(\hat{\boldsymbol{x}}_k^{(-)})\boldsymbol{P}_k^{(-)}\boldsymbol{H}_k^T(\hat{\boldsymbol{x}}_k^{(-)}) + \boldsymbol{R}_k\right]^{-1} \tag{4-10}$$

where $^{(-)}$ signifies values immediately prior to the update, $^{(+)}$ signifies immediately after the update, and ^ signifies an estimated value. The vector $\boldsymbol{h}_k(\hat{\boldsymbol{x}})$ provides the expected measurement values based on the current state estimate. The matrices $\boldsymbol{F}(\hat{\boldsymbol{x}})$ and $\boldsymbol{H}_k(\hat{\boldsymbol{x}}_k)$ are the Jacobian of the state and expected measurements, respectively, and are defined as:

$$\boldsymbol{F}[\hat{\boldsymbol{x}}(t)] \equiv \left.\frac{\partial \boldsymbol{f}(\boldsymbol{x}(t))}{\partial \boldsymbol{x}}\right|_{\boldsymbol{x}(t)=\hat{\boldsymbol{x}}(t)^{(+)}} \tag{4-11}$$

$$\boldsymbol{H}_k[\hat{\boldsymbol{x}}(t_k)] \equiv \left.\frac{\partial \boldsymbol{h}(\boldsymbol{x}(t))}{\partial \boldsymbol{x}}\right|_{\boldsymbol{x}(t)=\hat{\boldsymbol{x}}(t_k)^{(-)}} \tag{4-12}$$

The Jacobian is defined as:

$$\frac{\partial \boldsymbol{a}}{\partial \boldsymbol{b}} = \begin{bmatrix} \frac{\partial a_1}{\partial b_1} & \frac{\partial a_1}{\partial b_2} & \cdots & \frac{\partial a_1}{\partial b_n} \\ \frac{\partial a_2}{\partial b_1} & \frac{\partial a_2}{\partial b_2} & \cdots & \frac{\partial a_2}{\partial b_n} \\ \vdots & \vdots & \ddots & \vdots \\ \frac{\partial a_n}{\partial b_1} & \frac{\partial a_n}{\partial b_2} & \cdots & \frac{\partial a_n}{\partial b_n} \end{bmatrix} \tag{4-13}$$

A block diagram of this iterative process can be found in Figure 4-13. In summary, the state estimate, which is determined by using the propagation equations, is used to determine the predicted LED locations on the CCD ($\boldsymbol{h}_k$). These predicted locations are compared with the actual location as found by the measurement taken by the camera (z_k). The difference between these two values is multiplied by a gain ($\boldsymbol{K}_k$) to provide a correction factor ($\Delta\boldsymbol{x}$), which is added to the initial estimate to yield the updated state and covariance.

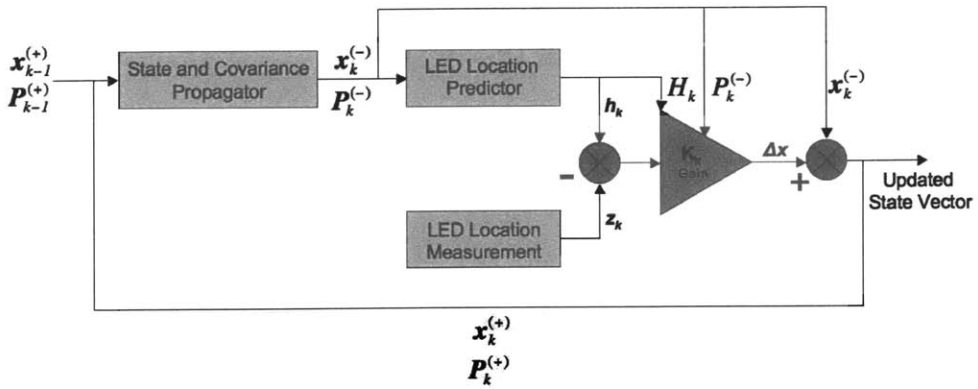

Figure 4-13: A block diagram showing the iterative process of the EKF.

4.3.2.1. Defining the state

The state is a 13x1 vector containing the position $\boldsymbol{r}$, velocity $\boldsymbol{v}$, quaternion $\boldsymbol{q}$, and the angular rate $\boldsymbol{\omega}$ components:

$$\boldsymbol{x} = \begin{bmatrix} \boldsymbol{r}^T & \boldsymbol{v}^T & \boldsymbol{q}^T & \boldsymbol{\omega}^T \end{bmatrix} \tag{4-14}$$

$$= \begin{bmatrix} r_x & r_y & r_z & v_x & v_y & v_z & q_1 & q_2 & q_3 & q_4 & \omega_x & \omega_y & \omega_z \end{bmatrix} \tag{4-15}$$

The position and velocity vector are referenced from the center of the SPHERE to the camera (Figure 4-14), and the four-element attitude quaternion is used to represent the orientation of the SPHERE. It should be noted that the state vector is given in the chase coordinate frame.

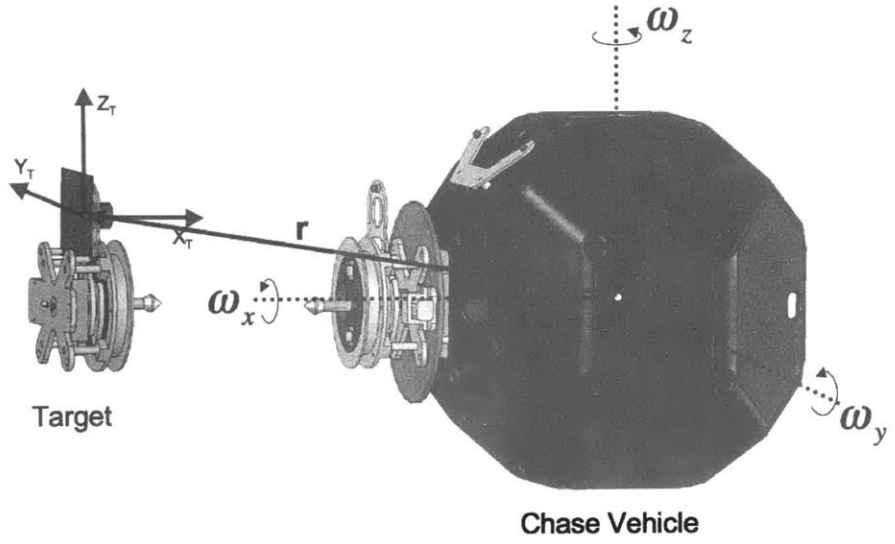

Figure 4-14: The state of the SPHERE.

4.3.2.2. State and covariance propagation

The following first order approximation can be used to propagate the state and covariance matrix:

$$\hat{\boldsymbol{x}}_k^{(-)} = \hat{\boldsymbol{x}}_{k-1}^{(+)} + \dot{\hat{\boldsymbol{x}}}(\hat{\boldsymbol{x}}(t))\Delta t\Big|_{\hat{\boldsymbol{x}}(t)=\hat{\boldsymbol{x}}_{k-1}^{(+)}} \tag{4-16}$$

$$\boldsymbol{P}_k^{(-)} = \boldsymbol{P}_{k-1}^{(+)} + \dot{\boldsymbol{P}}(\hat{\boldsymbol{x}}(t))\Delta t\Big|_{\hat{\boldsymbol{x}}=\hat{\boldsymbol{x}}_{k-1}^{(+)}} \tag{4-17}$$

where $\hat{\boldsymbol{x}}_{k-1}^{(+)}$ and $\boldsymbol{P}_{k-1}^{(+)}$ are the state and covariance at the previous time step. The values of $\dot{\hat{\boldsymbol{x}}}$ and $\dot{\boldsymbol{P}}$ are determined using the equations derived below (Equations 4-19 and 4-23, respectively). The time increment, Δt is determined using the following relationship:

$$\Delta t = t_k - t_{k-1} \tag{4-18}$$

The derivation for $\dot{\hat{\boldsymbol{x}}}$ begins by rewriting Equation 4-6 as

$$\dot{\hat{\boldsymbol{x}}} = \boldsymbol{A}(\hat{\boldsymbol{x}})\hat{\boldsymbol{x}}(t) \tag{4-19}$$

where

$$\boldsymbol{A}(\hat{\boldsymbol{x}}) = \begin{bmatrix} \boldsymbol{0}_{3x3} & \boldsymbol{I}_{3x3} & \boldsymbol{0}_{3x4} & \boldsymbol{0}_{3x3} \\ \boldsymbol{0}_{3x3} & \boldsymbol{0}_{3x3} & \boldsymbol{0}_{3x4} & \boldsymbol{0}_{3x3} \\ \boldsymbol{0}_{4x3} & \boldsymbol{0}_{4x3} & \frac{1}{2}\boldsymbol{\Omega}(\hat{\boldsymbol{\omega}}) & \boldsymbol{0}_{4x3} \\ \boldsymbol{0}_{3x3} & \boldsymbol{0}_{3x3} & \boldsymbol{0}_{3x4} & \boldsymbol{0}_{3x3} \end{bmatrix} \tag{4-20}$$

and

$$\boldsymbol{\Omega}(\hat{\boldsymbol{\omega}}) \equiv \begin{bmatrix} 0 & \omega_z & -\omega_y & \omega_x \\ -\omega_z & 0 & \omega_x & \omega_y \\ \omega_y & -\omega_x & 0 & \omega_z \\ -\omega_x & -\omega_y & -\omega_z & 0 \end{bmatrix} \tag{4-21}$$

Equations 4-20 and 4-21 use the following relationship for propagating the attitude quaternion:

$$\dot{\boldsymbol{q}} = \frac{1}{2}\boldsymbol{\Omega}(\hat{\boldsymbol{\omega}})\boldsymbol{q} \tag{4-22}$$

The derivation of $\dot{\boldsymbol{P}}$ begins by combining 4-7, 4-11 and 4-19:

$$\dot{P}(t) = \frac{\partial(A(\hat{x})\hat{x}(t))}{\partial\hat{x}} P(t) + P(t)\frac{\partial(A(\hat{x})\hat{x}(t))^T}{\partial\hat{x}} + Q(t) \qquad 4\text{-}23$$

where

$$\frac{\partial(A(\hat{x})\hat{x}(t))}{\partial\hat{x}} = \frac{1}{2}\begin{bmatrix} 0_{3x3} & I_{3x3} & 0_{3x1} & 0_{3x1} & 0_{3x1} & 0_{3x1} & 0_{3x1} & 0_{3x1} & 0_{3x1} \\ 0_{3x3} & 0_{3x3} & 0_{3x1} & 0_{3x1} & 0_{3x1} & 0_{3x1} & 0_{3x1} & 0_{3x1} & 0_{3x1} \\ 0_{1x3} & 0_{1x3} & 0 & \omega_z & -\omega_y & \omega_x & q_4 & -q_3 & q_2 \\ 0_{1x3} & 0_{1x3} & -\omega_z & 0 & \omega_x & \omega_y & q_3 & q_4 & -q_1 \\ 0_{1x3} & 0_{1x3} & \omega_y & -\omega_x & 0 & \omega_z & -q_2 & q_1 & q_4 \\ 0_{1x3} & 0_{1x3} & -\omega_x & -\omega_y & -\omega_z & 0 & -q_1 & -q_2 & -q_3 \\ 0_{3x3} & 0_{3x3} & 0_{3x1} & 0_{3x1} & 0_{3x1} & 0_{3x1} & 0_{3x1} & 0_{3x1} & 0_{3x1} \end{bmatrix} \qquad 4\text{-}24$$

The white noise covariance matrix, $Q(t)$, is assumed to be constant and will be discussed in Section 4.3.2.4.

4.3.2.3. State and covariance update using measurements

Equations 4-8 and 4-9 are the key equations used to update the state. To use these equations, the predicted location of the LED's based on the propagated state, h_k, must be determined along with the Kalman gain, K_k. The state is updated by comparing predicted LED locations (row and column) to the measured values. The difference between these two values is multiplied by the Kalman gain, which yields a correcting term for the state, Δx (Figure 4-13).

Predicting the location of the LED's based on the state: h_k

The objective of this subsection is to develop an algorithm that will predict the location of the LED's on the CCD based on the current states. The location of the LED is specified by its row and column location given in pixels (Figure 4-3). Thus, for a given position and orientation of the SPHERE there is a corresponding row and column illumination point on the CCD for each of the LED's.

First, a vector must be drawn from each LED to the camera as shown in Figure 4-15. The predicted location of each LED on the CCD can be determined by rewriting Equation 4-3:

$$\boldsymbol{h} = \begin{bmatrix} row_{LED\#1} \\ column_{LED\#1} \\ row_{LED\#2} \\ column_{LED\#2} \\ row_{LED\#3} \\ column_{LED\#3} \end{bmatrix} = C\kappa \begin{bmatrix} \left(\frac{1}{{}^{T}R_{1,x}}\right).{}^{T}R_{1,z} \\ \left(\frac{1}{{}^{T}R_{1,x}}\right).{}^{T}R_{1,y} \\ \left(\frac{1}{{}^{T}R_{2,x}}\right).{}^{T}R_{2,z} \\ \left(\frac{1}{{}^{T}R_{2,x}}\right).{}^{T}R_{2,y} \\ \left(\frac{1}{{}^{T}R_{3,x}}\right).{}^{T}R_{3,z} \\ \left(\frac{1}{{}^{T}R_{3,x}}\right).{}^{T}R_{3,y} \end{bmatrix} \qquad 4\text{-}25$$

where ${}^{a}R_{b,c}$ is the scalar component of a 3D vector in the a coordinate frame, going from the camera to the LED b, along the c axis. Superscripts T and C designate the target and chase coordinate frame, respectively (Figure 4-15).

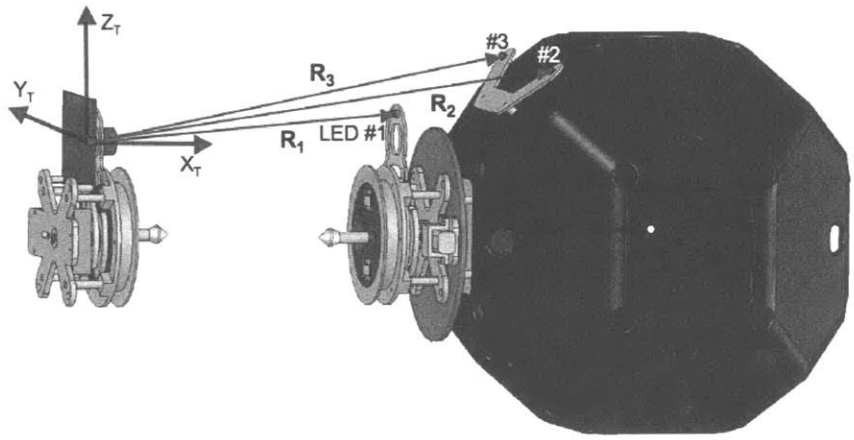

Figure 4-15: Vectors from the camera to each of the LED's.

Though the $\boldsymbol{R}$ vectors are initially unknown, two other known pieces of information can be used to determine ${}^{T}\boldsymbol{R}$, as shown in Figure 4-16. The relationship can be summarized as:

$${}^{T}\boldsymbol{R}_{i} = {}^{T}\boldsymbol{S}_{i} - {}^{T}\boldsymbol{r} \qquad 4\text{-}26$$

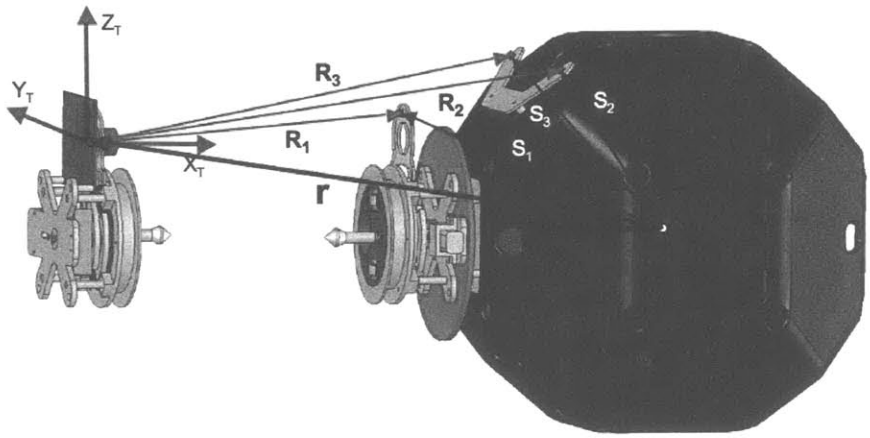

Figure 4-16: The known position of the SPHERE ($\boldsymbol{r}$) along with the location of the LED's ($\boldsymbol{S}_i$) can be used to determine the $\boldsymbol{R}$ vectors.

A 3D computer model was used to measure the location of the LED's in the chase coordinate frame, which yielded the static values of ${}^{C}\boldsymbol{S}_{1,c}$, ${}^{C}\boldsymbol{S}_{2,c}$ and ${}^{C}\boldsymbol{S}_{3}$. The vector ${}^{C}\boldsymbol{r}$ is part of the known state vector. The *attitude matrix*, $\boldsymbol{A}_q$, can be used to convert these vectors to the target frame (Appendix C). Since the $\boldsymbol{S}$ and $\boldsymbol{r}$ vectors are known a priori in the chase coordinate frame, Equation 4-26 can be rewritten as:

$$ {}^{T}\boldsymbol{R}_i = \boldsymbol{A}_q^t\left({}^{C}\boldsymbol{S}_i - {}^{C}\boldsymbol{r}\right) \qquad 4\text{-}27 $$

Now that each of the ${}^{T}\boldsymbol{R}_i$ vectors are known, Equation 4-25 can be used to predict the location of the LED's based on the state, which is the vector $\boldsymbol{h}_k$.

Determining the Kalman gain: $\mathbf{K}_k$

The Kalman gain is determined using Equation 4-10, which requires knowledge of $\boldsymbol{H}_k$ and $\boldsymbol{R}_k$. It is assumed that $\boldsymbol{R}_k$ is constant, and these values will be discussed in Section 4.3.2.4. As shown in Equation 4-12, $\boldsymbol{H}_k$ is the Jacobian of $\boldsymbol{h}_k$, which is a function relating the measurements to the states. Thus, $\boldsymbol{H}_k$ represents how the measurements change as a function of each of the state variables. Calculating $\boldsymbol{H}_k$ by hand is quite rigorous, thus the symbolic toolbox in Matlab was used. To determine $\boldsymbol{H}_k$, the vector $\boldsymbol{h}_k$ must be put directly in terms of the state by combining Equations 4-25 and 4-27. This modified form of $\boldsymbol{h}_k$ is then differentiated directly using Equation 4-13.

4.3.2.4. Initial conditions

The initial values of the state vector should be chosen to closely match the position of the vehicle when the docking sensor is initially activated. The initial position of the vehicle can be estimated since the global metrology is commanded to bring the vehicle to an approximate location before the docking sensor is activated. Thus, the following initial values were used for the state vectors:

$$\boldsymbol{r}_{initial} = \begin{bmatrix} 1 & 0 & 0 \end{bmatrix}^T \text{ m} \tag{4-28}$$

$$\boldsymbol{v}_{initial} = \begin{bmatrix} 0 & 0 & 0 \end{bmatrix}^T \text{ m/s} \tag{4-29}$$

$$\boldsymbol{q}_{initial} = \begin{bmatrix} 0 & 0 & 1 & 0 \end{bmatrix}^T \tag{4-30}$$

$$\boldsymbol{\omega}_{initial} = \begin{bmatrix} 0 & 0 & 0 \end{bmatrix}^T \text{ rad/s} \tag{4-31}$$

These initial state values assume that the SPHERE is initially 1 m directly in front of the camera and orientated upright with zero angular and range velocities. Another method would be to pass the global state estimates as the initial conditions.

The values for $\boldsymbol{P}_{initial}$ and $\boldsymbol{Q}$ were chosen iteratively. Reasonable values were chosen but then modified until a good convergence pattern was observed. The values for $\boldsymbol{R}$ were determined by calculating the variance of static CCD measurements.

$$\boldsymbol{P}_{initial} = \begin{bmatrix}
.00001 & 0 & 0 & 0 & 0 & 0 & 0 & 0 & 0 & 0 & 0 & 0 & 0 \\
0 & .00001 & 0 & 0 & 0 & 0 & 0 & 0 & 0 & 0 & 0 & 0 & 0 \\
0 & 0 & .00001 & 0 & 0 & 0 & 0 & 0 & 0 & 0 & 0 & 0 & 0 \\
0 & 0 & 0 & .00002 & 0 & 0 & 0 & 0 & 0 & 0 & 0 & 0 & 0 \\
0 & 0 & 0 & 0 & .00002 & 0 & 0 & 0 & 0 & 0 & 0 & 0 & 0 \\
0 & 0 & 0 & 0 & 0 & .00002 & 0 & 0 & 0 & 0 & 0 & 0 & 0 \\
0 & 0 & 0 & 0 & 0 & 0 & .001 & 0 & 0 & 0 & 0 & 0 & 0 \\
0 & 0 & 0 & 0 & 0 & 0 & 0 & .001 & 0 & 0 & 0 & 0 & 0 \\
0 & 0 & 0 & 0 & 0 & 0 & 0 & 0 & .001 & 0 & 0 & 0 & 0 \\
0 & 0 & 0 & 0 & 0 & 0 & 0 & 0 & 0 & .001 & 0 & 0 & 0 \\
0 & 0 & 0 & 0 & 0 & 0 & 0 & 0 & 0 & 0 & .002742 & 0 & 0 \\
0 & 0 & 0 & 0 & 0 & 0 & 0 & 0 & 0 & 0 & 0 & .002742 & 0 \\
0 & 0 & 0 & 0 & 0 & 0 & 0 & 0 & 0 & 0 & 0 & 0 & .002742
\end{bmatrix} \tag{4-32}$$

$$Q = \begin{bmatrix} 10^{-6} & 0 & 0 & 0 & 0 & 0 & 0 & 0 & 0 & 0 & 0 & 0 & 0 \\ 0 & 10^{-6} & 0 & 0 & 0 & 0 & 0 & 0 & 0 & 0 & 0 & 0 & 0 \\ 0 & 0 & 10^{-6} & 0 & 0 & 0 & 0 & 0 & 0 & 0 & 0 & 0 & 0 \\ 0 & 0 & 0 & 10^{-7} & 0 & 0 & 0 & 0 & 0 & 0 & 0 & 0 & 0 \\ 0 & 0 & 0 & 0 & 10^{-7} & 0 & 0 & 0 & 0 & 0 & 0 & 0 & 0 \\ 0 & 0 & 0 & 0 & 0 & 10^{-7} & 0 & 0 & 0 & 0 & 0 & 0 & 0 \\ 0 & 0 & 0 & 0 & 0 & 0 & 10^{-4} & 0 & 0 & 0 & 0 & 0 & 0 \\ 0 & 0 & 0 & 0 & 0 & 0 & 0 & 10^{-4} & 0 & 0 & 0 & 0 & 0 \\ 0 & 0 & 0 & 0 & 0 & 0 & 0 & 0 & 10^{-4} & 0 & 0 & 0 & 0 \\ 0 & 0 & 0 & 0 & 0 & 0 & 0 & 0 & 0 & 10^{-4} & 0 & 0 & 0 \\ 0 & 0 & 0 & 0 & 0 & 0 & 0 & 0 & 0 & 0 & 10^{-5} & 0 & 0 \\ 0 & 0 & 0 & 0 & 0 & 0 & 0 & 0 & 0 & 0 & 0 & 10^{-5} & 0 \\ 0 & 0 & 0 & 0 & 0 & 0 & 0 & 0 & 0 & 0 & 0 & 0 & 10^{-5} \end{bmatrix} \quad 4\text{-}33$$

$$R = \begin{bmatrix} .125 & 0 & 0 & 0 & 0 & 0 \\ 0 & .125 & 0 & 0 & 0 & 0 \\ 0 & 0 & .125 & 0 & 0 & 0 \\ 0 & 0 & 0 & .125 & 0 & 0 \\ 0 & 0 & 0 & 0 & .125 & 0 \\ 0 & 0 & 0 & 0 & 0 & .125 \end{bmatrix} \quad 4\text{-}34$$

All the values are given in Standard International units.

4.3.3. Overview of the Matlab code

The Matlab code contains the algorithms used to execute the MVDS. The following is a summary of the key algorithm features, and Figure 4-17 is a flowchart of the Matlab code.

Initial setup

1. The serial/wireless communication port is opened

2. The camera is activated and the settings are adjusted using the Matlab Image Acquisition Toolbox:

vid = videoinput('dcam',1,'Y8_640x480'); % activates the camera
set(getselectedsource(vid),'Gain',500); % sets the gain of the camera
set(getselectedsource(vid),'FrameRate','30'); % sets the frame rate of the camera

set(getselectedsource(vid),'ShutterMode','man'); % sets the shutter mode of the camera
set(getselectedsource(vid),'Shutter',450); % sets the shutter speed of the camera
triggerconfig(vid, 'manual'); % set trigger of the camera to manual
start(vid); % the camera is now ready to grab images when called upon

Algorithm Loop

1. Grabs the computer's clock time to determine Δt

2. Camera captures an image; obtains a 640x480 array of pixel intensities:

frame = getsnapshot(vid); % captures a frame from the camera

3. The function three_points.m is called which finds the centers of the three LED's using functions available with Matlab's Image Processing Toolbox:

frame_binary = im2bw(frame, graythresh(frame)); % converts the captured image to a binary image
[B,L] = bwboundaries(frame_binary,'noholes'); % finds all the circles in the image
s = regionprops(L, 'centroid'); % calculates the centroids of each circle
centroids = cat(1, s.Centroid); % the row and column for each of the centroids is stored

4. Checks to make sure only three LED's were found. If more were found, it takes the three brightest ones. A stray dim IR source could be incorrectly seen as an LED.

5. The rows and columns of the three LED centroids are passed to the function e_kalman_filter.m. This function uses Equations 4-16 and 4-17 to propagate the state and convariance and then Equations 4-8, 4-9 and 4-10 to update the state and covariance.

6. The updated state is sent wirelessly to the SPHERE. The SPHERE uses this information to dock to the Mothership.

7. The updated state and covariance are used as the new input, and the algorithm is continually looped.

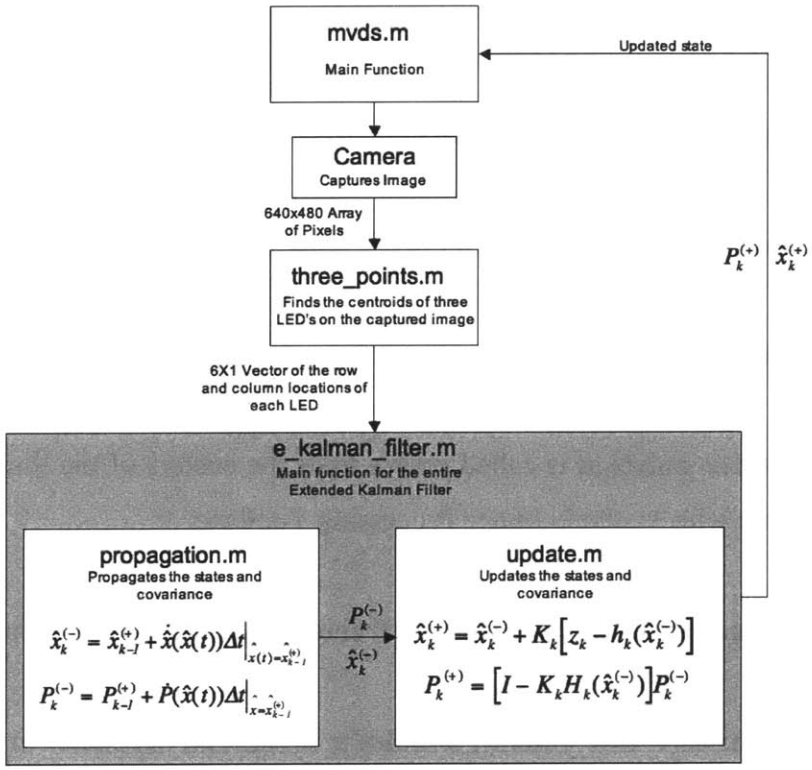

Figure 4-17: Flow chart of the Matlab code.

4.4. Testing and Validation

Two types of tests were performed to verify the validity of the MVDS. The first test used the sensor to take measurements at known distances. These results give an estimate of the sensor accuracy, and can be compared with a theoretical model to understand the sources of error in the measurements. The second test used the sensor to complete a fully autonomous docking and undocking maneuver as shown in Figure 4-1. The results from these tests will be presented and analyzed to determine the validity of the MVDS.

4.4.1. Experimentally estimating the accuracy of the MVDS

The MVDS was used to take measurements at known distances. The objective of this test was to simulate the conditions when two vehicles are docking. The test setup is shown in Figure 4-18. The SPHERE was mounted on a rotating stand with a dial to adjust the relative angle (θ) of the SPHERE. The stand was able to measure the actual angle with an accuracy of ½ degree. The angle is zero when the faces of both docking ports are parallel to each other. A separate docking port was mounted on a linear track, which was moved by known amounts using a motor-driven threaded shaft. The vector ***d*** is the distance between the centers of the two docking ports, and the track is able to make relative d_x and d_z displacements as shown in the figure. The track moves by increments of $1/4000^{th}$ of an inch in the d_x direction and $1/8000^{th}$ of an inch in the d_z direction. When the UDP's are touching and aligned this distance is zero. The measurement error is defined as the difference between the known position and the measurement:

$$error = d_{actual} - d_{measured} \tag{4-35}$$

The percentage error can be determined using:

$$error(\%) = \frac{error}{d_{actual}} 100\% \tag{4-36}$$

Before beginning the tests, the sensor was "calibrated," which involved determining the distance between the lens and CCD, κ (Figure 4-5-b). As mentioned earlier, κ is assumed to be constant, and the value must be estimated experimentally since it is unknown. To this end, measurements were taken at d_x = 60 cm and then κ was varied until the error was zero.

The first test measured the error in the d_x direction. The track was placed directly in front of the SPHERE as shown in Figure 4-18. The two docking ports were brought together so their faces were touching, and then the track was moved back to vary d_x and measurements were taken from d_x = 1.5 cm to 150 cm with 1.27 cm increments. The error, as defined in Equations 4-35 and 4-36, is plotted for varying values of d_x in Figure 4-19. A theoretical model is developed in Section 4.4.2 to explain the sources of error, and thus the general trends found in Figure 4-19.

The next test measured the error in the d_z direction. Again, the two docking ports were brought together and aligned by putting their faces together. The track was moved to a known d_x location and then d_z was varied from approximately -7 to +5 cm with 1.27 cm increments. These measurements were done at three known d_x locations. The range of the linear track limited these measurements, and at close distances the sensor reached the limit of its operating range because of the camera's limited field of view (Table 4-1).

The final test measured the error for different SPHERE angles (θ). The angle is defined in Figure 4-18. Again, the two docking ports were brought together and aligned by putting their faces together. The track was moved to a known d_x location and the angle was varied from approximately zero to seventy degrees with two-degree increments. These measurements were taken at two known d_x locations, with $d_y = d_z = 0$. The results from these angle measurements are shown in Figure 4-21.

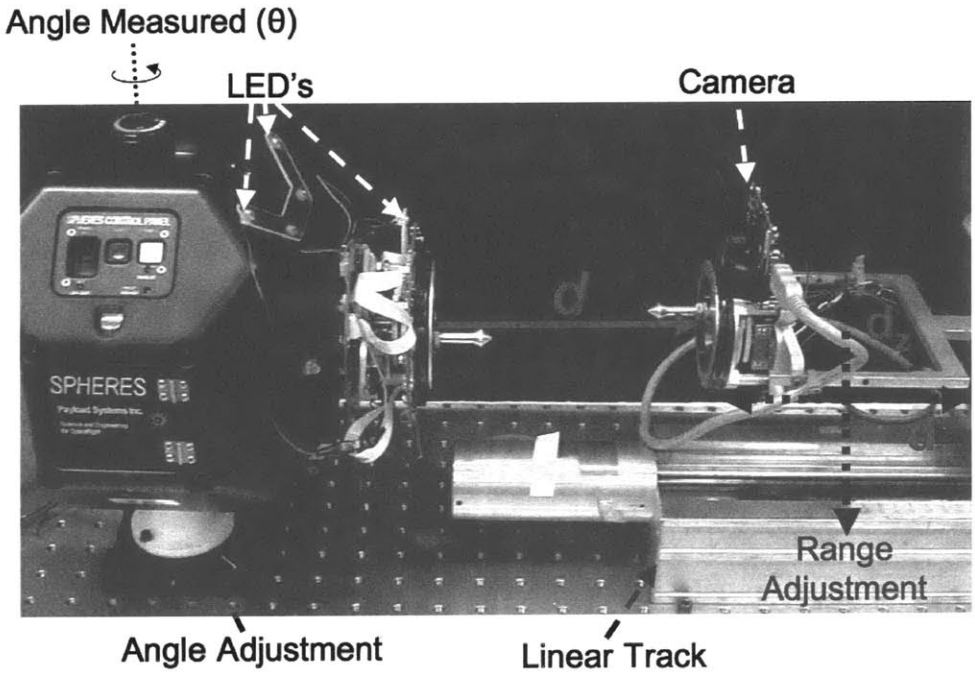

Figure 4-18: Experimental setup for measuring the MVDS error.

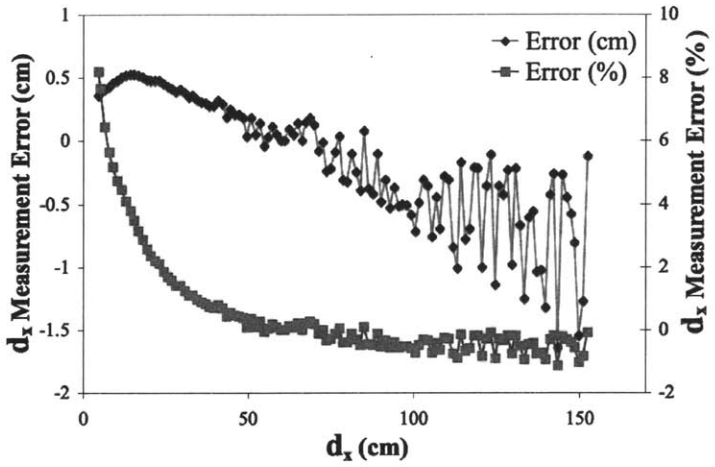

Figure 4-19: MVDS experimental error (x-direction).

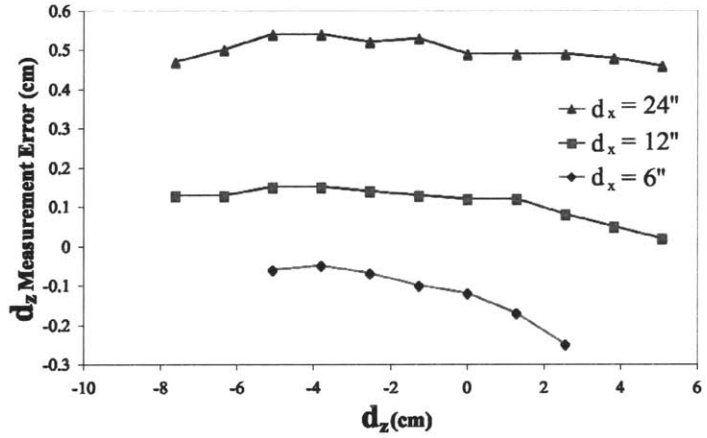

Figure 4-20: MVDS range error (z-direction).

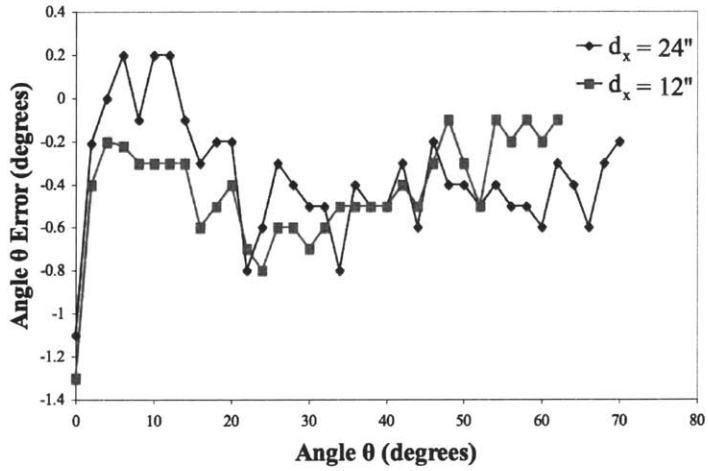

Figure 4-21: MVDS angle error.

The following conclusions can be made based on these tests:

- The error in the d_x direction is less than ½ cm from 1.5 to 100 cm.
- The error in the d_y and d_z direction is less than ½ cm for d_x distances up to 30 cm. Other distances were not tested, though values could be extrapolated using the experimental data.
- The error in angle is less than 1 degree for d_x distances up to 30 cm (except for $\theta = 0$). Other distances were not tested, though values could be extrapolated using the experimental data.
- Though the maximum case was not tested because of experimental limitations, it can be deduced that the sensor would work for values of d_x greater than 2 meters.
- The largest measurable angle (θ) is 70 degrees.

4.4.2. Analyzing the experimental results using theoretical models

This section examines the experimental results shown in Figure 4-19. Comparisons are made with theoretical models to find sources of errors. Only the d_x direction will be considered since it is the only direction where a sufficient amount of data was collected. Also, it is likely that the most dominant error sources will be found by just analyzing this single direction.

The experimental measurement error shown in Figure 4-19 can be separated into two sources of error. One source adds a "bias," which causes the error to initially behave like an upside-down parabola and then linearly decrease (Figure 4-22). The other error source adds error "uncertainty," which is seen as oscillations in the data that increase in amplitude with distance (d_x). Since the separation distance between the two docking ports (d_x) is slightly less than the distance between the camera and LED's (R_x), it will be assumed that:

$$R_x = d_x + 4 \text{ [cm]} \qquad 4\text{-}37$$

Thus, in the following derivations R_x will be used instead of d_x. For the plots, R_x values were converted to d_x using Equation 4-37.

Error bias:

The error bias could be caused by the optical model shown in Figure 4-5-b, which assumed that the LED image is perfectly focused on the CCD. In reality, the image distance (S_i) varies with the object distance (S_o) according to Equation 4-1, and thus there is only one object distance that would produce a focused image on the fixed CCD. Consequently, the LED is out of focus, and thus the image on the CCD is blurred and shifted as shown in Figure 4-23. Using the similar triangles shown in Figure 4-23, the following relationship can be formed:

$$\frac{h_{measured}}{\kappa} = \frac{h_{actual}}{S_i} \tag{4-38}$$

The measurement error (%) is the difference between the actual and measured LED centroid location:

$$error_{bias,t}(\%) = \frac{h_{actual} - h_{measured}}{h_{actual}} 100\% \tag{4-39}$$

where the subscript *bias,t* designates the theoretical error bias. By combining Equations 4-38 and 4-39:

$$error_{bias,t}(\%) = \left(1 - \frac{\kappa}{S_i}\right) 100\% \tag{4-40}$$

The image distance (S_i) can be determined using Equation 4-1. A comparison between the experimental and theoretical percent error is shown in Figure 4-24. If it is assumed that this theoretical error bias is directly propagated through to the distance measurement, then:

$$error_{bias,t} = \frac{R_{x,actual} \cdot error_{bias,t}(\%)}{100} \tag{4-41}$$

This is a prediction of the experimental error as defined in Equation 4-35. Equation 4-41 can be used to compare the experimental and theoretical error bias measurements as shown in Figure 4-25. The parameter values used to determine the theoretical error are shown in Table 4-2.

It was found that the theoretical error bias closely matches the experimental results (Figure 4-24 and Figure 4-25). The next subsection investigates the error uncertainty, which is seen as oscillations in the data that increase in amplitude with distance.

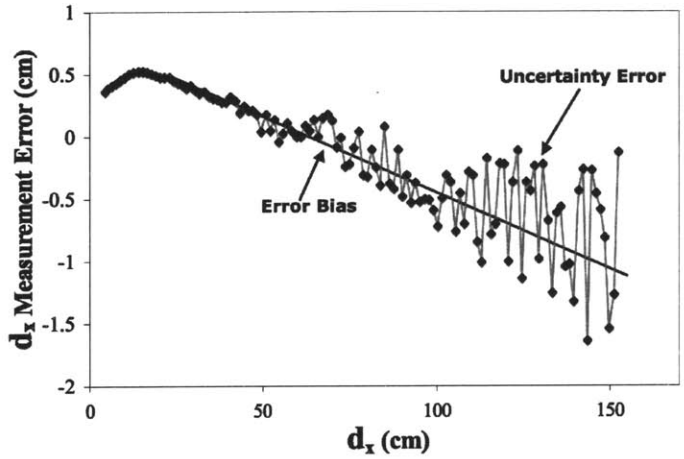

Figure 4-22: The experimental error, which was also shown in Figure 4-19. There is both an error bias (black curve) and an error uncertainty (oscillations).

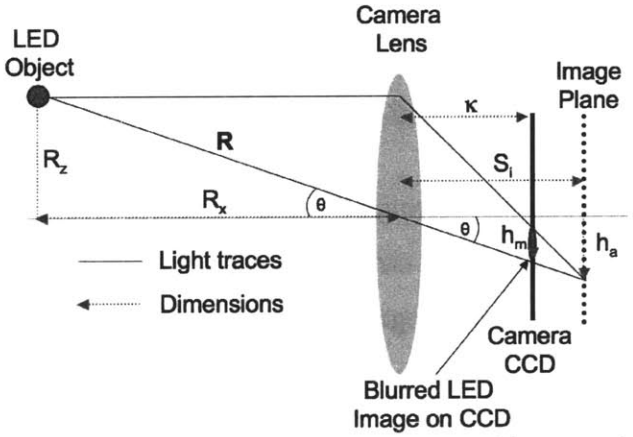

Figure 4-23: The optical model used to explain the error bias term in Figure 4-22. The variables $h_{measured}$ and h_{actual} are shown as h_m and h_a, respectively.

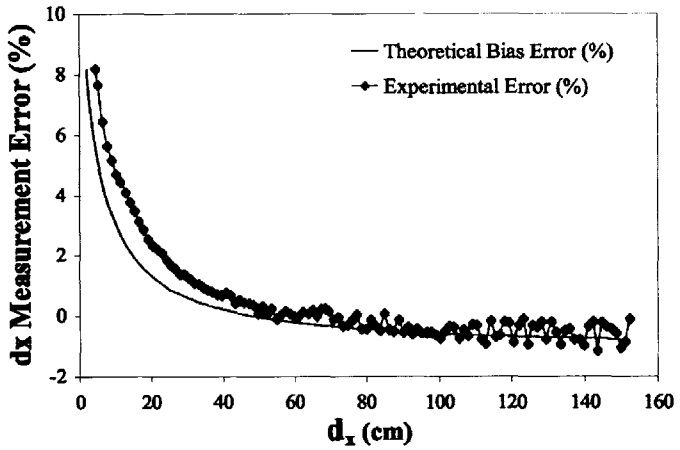

Figure 4-24: Comparing the experimental error (%) to the theoretical error bias.

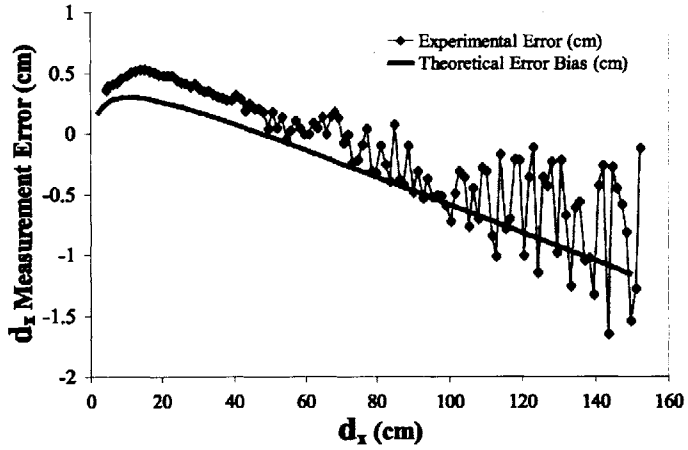

Figure 4-25: Comparing the experimental error to the theoretical error bias.

Error uncertainty:

The uncertainty is defined as smallest change in the LED position that can be accurately detected by the CCD, and is represented as ΔR_x. It is predicted that the uncertainty causes oscillations in the data that increase in amplitude with distance (Figure 4-22). This uncertainty exists because the camera is a discrete measuring device, and thus can only sense discrete changes in the LED position.

The uncertainty in the LED position (ΔR_x) can be related to the smallest detectable change in the CCD image location (Δh), which is measured in pixels, by finding a function f such that:

$$\Delta R_x = f(\Delta h) \tag{4-42}$$

The value of Δh is equal to a multiple or fraction of a pixel. The following definitions will be used:

$$\Delta R_x = R_{x,2} - R_{x,1} \tag{4-43}$$

$$\Delta h = h_2 - h_1 \tag{4-44}$$

The subscripts 1 and 2 designate the value before and after the LED moves, respectively. It can be seen from Figure 4-26 that when only moving in the R_x direction, the following is true:

$$R_{y,1} = R_{y,2} = R_y \qquad \text{and} \qquad R_{x,1} = R_x \tag{4-45}$$

Thus by using similar triangles:

$$\frac{R_y}{R_{x,1}} = \frac{h_1 P}{\kappa} \qquad \text{and} \qquad \frac{R_y}{R_{x,2}} = \frac{h_2 P}{\kappa} \tag{4-46}$$

where P is the size of a single pixel in meters (Table 4-1). Equations 4-43, 4-44, 4-45 and 4-46 can be combined to show that:

$$\Delta h = \frac{\kappa R_y}{P}\left(\frac{1}{\Delta R_x + R_x} - \frac{1}{R_x}\right) \tag{4-47}$$

By rearranging, ΔR_x can be determined:

$$|\Delta R_x| = \frac{\beta R_x^2}{\beta R_x + 1} \tag{4-48}$$

where

$$\beta = \frac{\Delta h P}{\kappa R_y} = \frac{\Delta h P}{\kappa D_1} \tag{4-49}$$

Equation 4-49 assumes that $R_y = D_1$ (Figure 4-6). From Equations 4-48 and 4-49, it can be seen that the uncertainty in the ΔR_x direction is smallest when the LED is close (small R_x),

the pixels on the CCD are very small (P is small), and R_y is large (D_I is large). Thus, the theoretical error uncertainty, $error_{uncertainty,t}$, can be estimated as:

$$error_{uncertainty,t} = RAND * |\Delta R_x| \qquad 4\text{-}50$$

where RAND is a random number ranging from -1 to +1. A random number generator is used since true uncertainty typically consists of bounded random values. The uncertainty in this case will be random, bounded from $-|\Delta R_x|$ to $+|\Delta R_x|$.

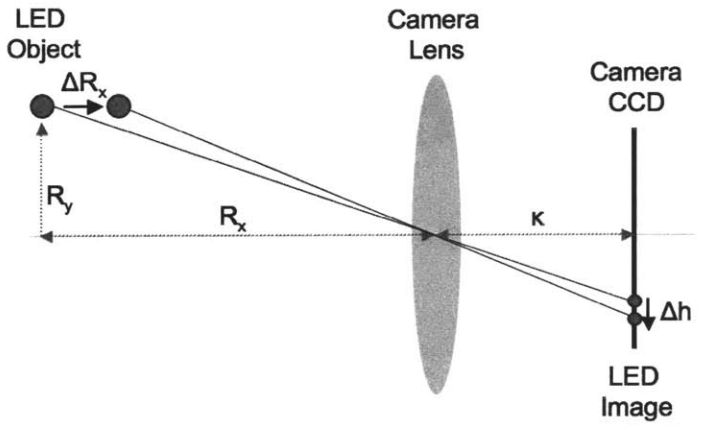

Figure 4-26: The optics model used to determine the theoretical uncertainty.

Combing the theoretical error bias and uncertainty:

The total theoretical error, $error_t$, can be estimated by combining the theoretical error bias and uncertainty derived in Equations 4-41 and 4-50, respectively:

$$error_t = error_{bias,t} + error_{uncertainty,t} \qquad 4\text{-}51$$

The theoretical and experimental errors are compared in Figure 4-27. The parameter values used to determine the theoretical error are shown in Table 4-2. It can be seen that the theoretical and experimental errors closely match, thus the bias and uncertainty errors are likely the most dominant error sources. These findings are summarized in Table 4-3. A list of other possible error sources can be found in Table 4-4, though they are likely less dominant; each is categorized as either a hardware or software related error.

Table 4-2: The values used to determine the theoretical bias and uncertainty error.

Parameter	Value
κ	6.07 mm
f	6 mm
Δh	¼ pixel
R_x	d_x+4.5 cm

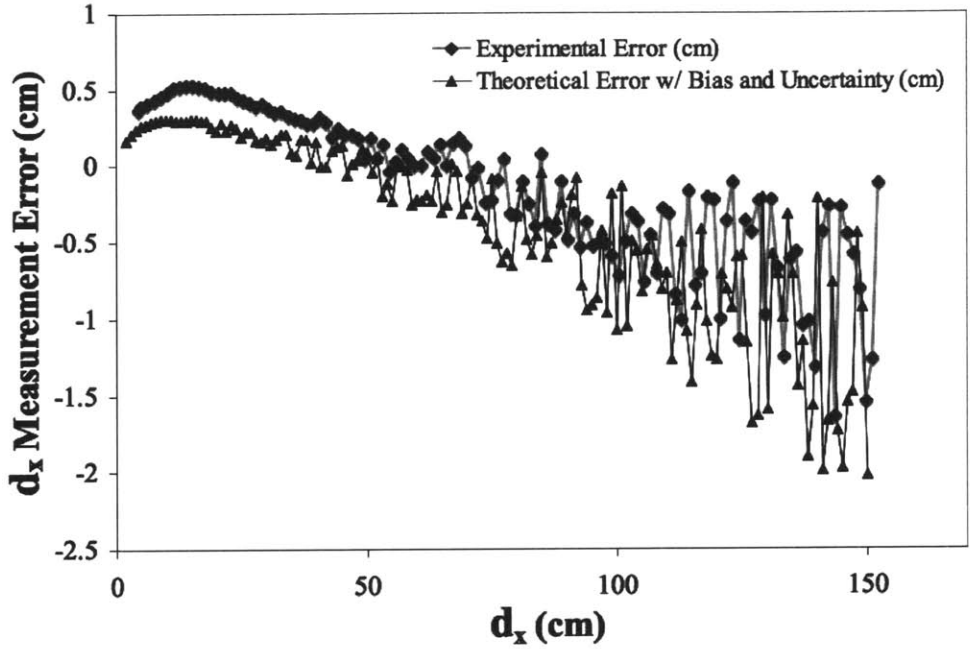

Figure 4-27: Comparing the theoretical and experimental error.

Table 4-3: The most dominant sources of error for the MVDS.

Dominant Error Sources	Possible Solutions
The error bias is caused by assuming that the LED image is perfectly focused on the CCD. In reality, the image distance (S_i) varies with the object distance (S_o) according to Equation 4-1, and thus there is only one object distance that would produce a focused image on the fixed CCD. Consequently, the LED is out of focus, and thus the image on the CCD is blurred and shifted as shown in Figure 4-23, which produces an inaccurate centroid location (h_{row}, h_{col}).	1. Use an auto-focusing lens that can also determine and track the value of κ. 2. If an auto-focusing lens is not available (i.e. using a fixed lens), then pick the d_x distance where you want the sensor to be most accurate. Then determine the S_i for this distance and put κ equal to S_i. 3. Use an optical system with a larger depth of focus.
The **error uncertainty** exists because the camera is a discrete measuring device, and thus can only sense discrete changes in the LED position.	1. Use a higher resolution CCD (smaller P). 2. Make D_1 larger.

Table 4-4: Other possible sources of error.

Hardware error sources: • Improper camera mounting (crooked, misaligned) • Lens defects (focal length, mounting) • Geometry measurements ($\mathbf{S}_i$, CAD model of the SPHERE/camera etc.)
Software error sources: • Finding the center of the LED's on the CCD (h_{row}, h_{col}) • Solution does not converge to the actual measurements (general EKF errors)

4.4.3. Autonomous docking and undocking using the MVDS and UDP

To perform a realistic demonstration of an autonomous docking maneuver, the MVDS and UDP were used in a series of docking tests as depicted in Figure 4-1 and Figure 4-2. The actual experimental hardware is shown in Figure 4-28. Besides initiating the docking and undocking, the entire maneuver was performed autonomously.

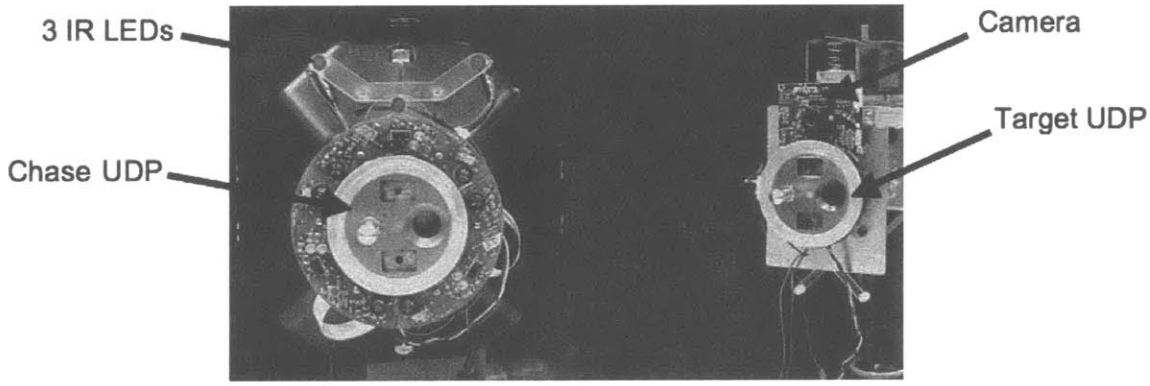

Figure 4-28: The UDP and MVDS hardware used to perform the autonomous docking and undocking tests.

To initiate the autonomous dock, a command was sent wirelessly from the desktop computer to the SPHERE. The SPHERE then used its global metrology system to position and orient itself within the operating range of the sensor (Figure 4-29). Once inside the operating range, the MVDS was activated. The MVDS computed the relative state of the

vehicle and sent the information via radio communication to the SPHERE with an update rate of approximately 6 Hz. The SPHERE used this state information along with an onboard docking algorithm [31] to orient itself approximately 1.5 centimeters in front of the target UDP. The electromagnets were then activated on the docking ports, which provided a soft capture. The pin sensor on the UDP was used to sense when full contact was achieved, and the docking ports were subsequently locked and then deactivated using the current sensor (Figure 3-26). After it was verified that a rigid docking was achieved, a command was sent from the desktop computer to the SPHERE to initiate undocking. The docking ports were unlocked, and then the electromagnets were set to repel. This pushed the SPHERE away from the Mothership, and the SPHERE then used the global metrology system to reposition and orient itself in a new predefined location. This concluded the autonomous docking test using the MVDS and UDP.

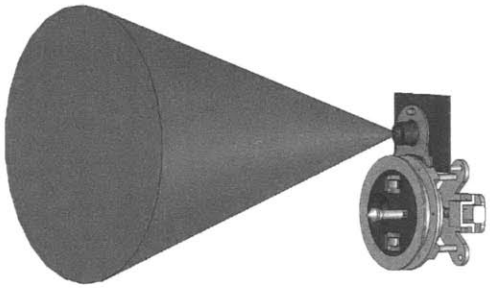

Figure 4-29: The MVDS has an operating range that is defined by a 50 degree full cone.

This test was performed multiple times with repeated success. The test results are shown in Figure 4-30 through Figure 4-33. The docking algorithm specified that the SPHERE should initially position itself approximately 45 cm from the target. Once at this location, the SPHERE was to glide straight into the target, with a decreasing velocity and a stop a 5 cm. The stop allowed the SPHERE to check its position and fine adjust its trajectory.

It should be noted that the onboard gyroscopes were used to obtain direct measurements of the angular velocities, $\boldsymbol{\omega}$. Although these velocities were computed using the EKF, the gyroscopes provide a cleaner and higher bandwidth calculation.

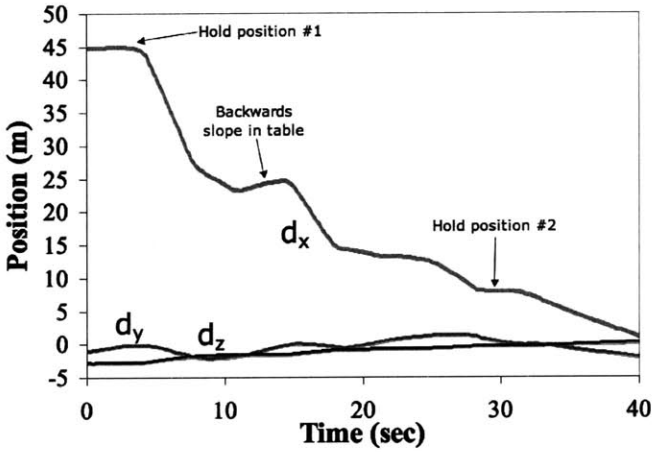

Figure 4-30: The distance between the two docking port faces during the docking test.

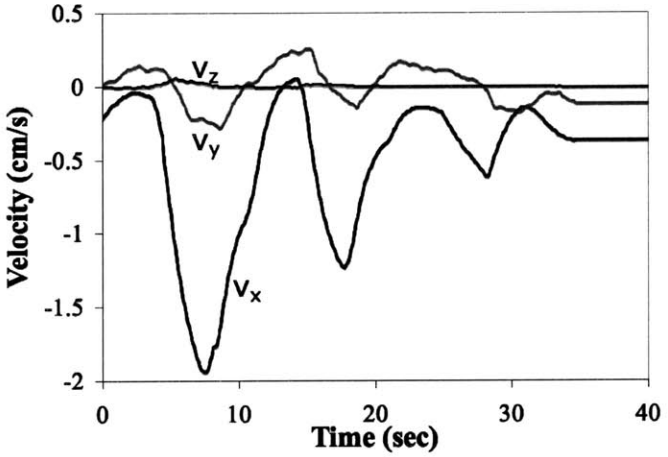

Figure 4-31: The relative velocity of the SPHERE during the docking test.

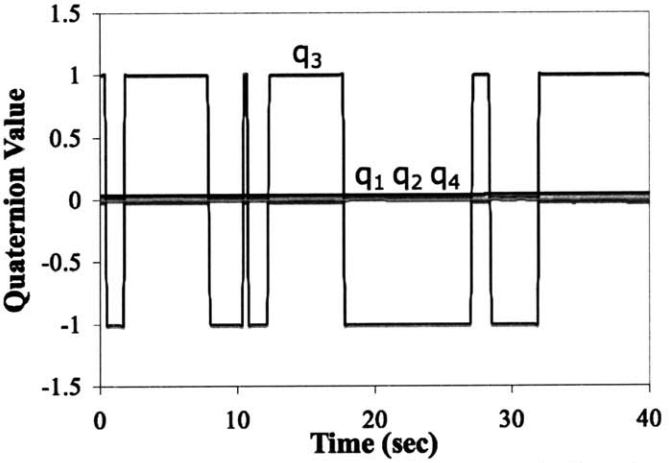

Figure 4-32: The relative quaternions of the SPHERE during the docking test.

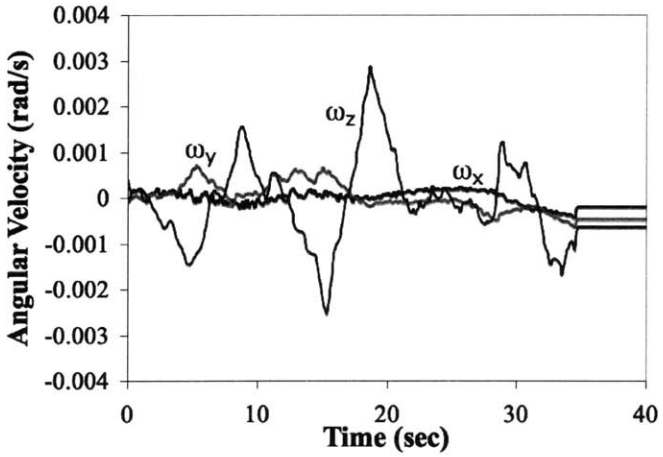

Figure 4-33: The relative angular velocity of the SPHERE during the docking test.

The large error sources in this test include the following:

- The table was difficult to level. The backwards slope in the table can be seen in Figure 4-30.
- Drag between the air-bearing pucks and table.
- Sensor limitations (Section 4.4.1).

4.5. Summary

This chapter discussed the development of the Miniature Video Docking Sensor (MVDS), which uses a set of infrared LED's, a miniature CCD-based video camera, and an Extended Kalman Filter (EKF) to determine the six relative degrees of freedom of two docking vehicles. Both the sensor hardware and software were discussed, including the theory of the EKF.

Two types of tests were performed to verify the validity of the MVDS. The first test used the sensor to take measurements at known distances. The error in the d_x direction is less than ½ cm from 1.5 to 100 cm while the error in the d_y and d_z direction is less than ½ cm for d_x distances up to 30 cm. Lastly, the error in angle is less than 1 degree for d_x distances up to 30 cm (except for $\theta = 0$). These results give an estimate of the sensor

accuracy, and were compared with a theoretical model to understand the sources of error in the measurements. The two dominant sources of theoretical error were found to be an error "bias" and "uncertainty." The error bias is caused by assuming that the LED image is perfectly focused on the CCD. In reality, the image distance (S_i) varies with the object distance (S_o) according to Equation 4-1, and thus there is only one object distance that would produce a focused image on the fixed CCD. Consequently, the LED is out of focus, and thus the image on the CCD is blurred and shifted as shown in Figure 4-23. The error uncertainty exists because the camera is a discrete measuring device, and thus can only sense discrete changes in the LED position. Suggestions on ways to reduce the error bias and uncertainty are presented in Table 4-3.

The second test used the sensor to complete a fully autonomous docking and undocking maneuver as shown in Figure 4-1. This demonstrated the fully integrated docking port and sensor system, which was a main focus of this thesis.

Chapter 5. Conclusions

This final chapter begins with a summary of the entire thesis. Then a list will be formed to outline the major contributions made by this body of work. Lastly, possible future work will be discussed, followed by a vision for the future of autonomous assembly and reconfiguration.

5.1. Thesis Summary

Section 2.1 defined a modular spacecraft design as one that has standardized and reconfigurable components with multiple decoupled subsystems. Examples were given of past space missions that have modular-like designs, though no mission to date serves as an example of a fully modular spacecraft as previously defined. An example was the Multi-mission Modular Spacecraft (MMS) program, which successfully produced a set of Earth-orbiting satellites using modular concepts. There are a few future missions that seek to demonstrate modularity (ex. SCOUT), though it is still unclear how modularity will fit into the overall future space initiatives.

Section 2.2 gave an overview of the SWARM project with a focus on the Bluetooth wireless communication protocol and the universal docking port. Then Section 2.2.3 defined a set of qualitative metrics and used the SWARM hardware to determine the relative "cost" of modularity. It was found that the electronics were the most costly component in this particular case.

The objective of Section 2.3 was to compare two methods for assembling a segmented primary mirror. Though this was not an example of a completely modular system, it investigated the concept of assembling and possibly reconfiguring a large number of modules in space. Comparisons were made between the propellant and electromagnetic-based systems. It was found that the propellant-based system is able to

assemble the telescope 2 to 3.5 times faster for a given amount of mass. However, as the telescope diameter increases, the difference between the two systems reduces. It was also noted that the telescope could be reconfigured without additional mass when using EMFF, though this is not the case with the propellant-based system. Thus, EMFF could offer mass savings if reconfiguration is required.

Chapter 3 discussed docking ports, which are required when autonomously assembling and reconfiguring modules. After a brief history, a list of docking port capabilities for unmanned spacecraft was formed, followed by a description of a universal docking port design. Lastly, Chapter 4 presented the development of the Miniature Video Docking Sensor (MVDS), which included analytical and empirical estimations of the measurement accuracy. It was found that the MVDS error in range is less than one cm within the operating range of 1.5 meters. The error in angle is less than 1 degree for range distances up to 30 cm. Other distances were not tested, though values could be extrapolated using the experimental data. This thesis concluded with the results from a fully integrated docking test, which used the SPHERES micro-satellites, the UDP, and the MVDS.

5.2. Contributions

This thesis made the following contributions:

- An overview of the SWARM ground-based testbed, which sought to demonstrate the use of modular spacecraft in a laboratory environment, and to investigate the "cost" of modularity.

- A framework for analyzing two different methods for assembling a large segmented mirror in space. Algorithms and equations were developed for both the propellant and EMFF-based systems.

- A brief history of docking ports, and a list of docking port capabilities for unmanned missions where docking is needed to assemble modular space systems.

- The design and fabrication of a miniature Universal Docking Port (UDP).

- The design and fabrication of an optical sensor that provides the relative state estimation of two vehicles during docking (MVDS).

- The demonstration of a repeatable autonomous docking maneuver using a micro-satellite and the fully integrated docking port and sensing system.

5.3. Future Work

Future docking port development will likely involve adding capabilities to the current UDP design. The capabilities of highest priority were ranked on a relative scale as shown in Table 5-1. Novelty, relevance, and difficulty were the metrics used. Novelty measures the level of technology development required, relevance measures how relevant the capability is to the overall objectives of the present research, and difficulty measures the complexity and amount of time that would be required to add that particular capability. It can be seen that the highest priority capabilities include adding data and communication capabilities directly to the docking port, fluid transfer and closed-loop EM control to improve the soft capture ability.

The next step for the MVDS is to integrate the camera onto the SPHERES vehicle. To do this, a dedicated Digital Signal Processor (DSP) will likely be used to analyze the captured images and then send information through the SPHERE's expansion port. It will be challenging to implement a DSP capable of capturing and analyzing images quickly (10+ Hz).

The algorithms used in the MVDS could also be improved. A better system dynamics model would be:

$$\dot{\hat{\boldsymbol{x}}} = \boldsymbol{A}(\hat{\boldsymbol{x}})\hat{\boldsymbol{x}}(t) + \boldsymbol{B}\dot{\boldsymbol{v}}(t) \qquad 5\text{-}1$$

The added $\dot{\boldsymbol{v}}(t)$ term could be determined by integrating the thruster values with time:

$$\dot{\boldsymbol{v}}(t) = \int_{t_{k-1}}^{t_k} \boldsymbol{T} dt \qquad 5\text{-}2$$

where $\boldsymbol{T}$ is a vector containing each of the SPHERE's thruster values. Also, more accurate algorithms could be developed to determine the center of the LED illumination spots. Lastly, the algorithms could be improved by adding a dynamic intensity threshold algorithm, which is used when finding the LED's on the CCD.

Currently the MVDS is an active-active system. Meaning, both vehicles must have power and be in a functionally operating mode for the sensor to work properly. An interesting alternative would be to place spots made of reflective corner cube tape all around the vehicle. A laser could be used to pulse light at the target, and the reflections would be focused to form spots on the CCD. The complications would be in filtering out the unwanted reflections, and knowing where each illumination spot is coming from on the SPHERE. Multiple frequency lasers and filters could help solve these problems.

Lastly, the MVDS could be improved by adding multiple target patterns. One technique could use a set of LED's (or spots made from reflective tape) that is used at far distances, and then another set to be used for very fine adjustments once the two docking vehicles are close. Another concept is to have many LED's (or spots made from reflective tape) all over the SPHERE, and have the algorithm utilize the largest number of LED's it can detect. This could greatly increase the accuracy of the sensor by providing the EKF with more measurements. A challenge with adding multiple targets will be to differentiate the various illuminated spots. Currently the algorithm only knows the order and location of the spots by having a priori information.

Table 5-1: The highest priority capabilities were ranked to determine future work.

	Novelty	Relevance	Difficulty	Total
3-position variable stiffness	2	2	2	**2**
Large angle articulation for configurations and con-ops	2	1	1	**1.5**
Close loop EM control for near zero impact docking	3	3	1	**2.4**
Addition of data communication that is established at docking	2	3	3	**2.5**
Fluid transfer	3	3	1	**2.4**
Heat sink/pipe, low resistance high conductivity path	2	3	1	**1.9**
System ID Capabilities or active vibration suppression	3	2	1	**2.2**
Weights	**0.5**	**0.2**	**0.3**	
	3=high 1=low	3=high 1=low	3=easy 1=hard	

5.4. The Future of Autonomous Assembly and Reconfiguration

Modular space systems could aid in the exploration of space by providing a means of building larger and more complex systems. Also, by having the ability to autonomously assemble and reconfigure (AAR) while in space, the lifetime of a modular spacecraft could be increased by providing the option of replacing only particular failed subsystems after years of operation. However, the autonomous assembly and reconfiguration of any modular space system will require advancements in autonomous rendezvous and docking technology.

Manual rendezvous and docking was successfully demonstrated during the manned Gemini and Apollo missions, and the Progress spacecraft is currently able to autonomously dock to the International Space Station. However, the complications experienced during NASA's recent Demonstration for Autonomous Rendezvous Technology (DART) mission proved the need for more technology.

Looking to the future, the SPHERES testbed can be used as a low cost and less risky alternative to full-scale missions. This thesis showed that docking ports and sensors

can be integrated with the SPHERES vehicle to demonstrate autonomous docking maneuvers. The UDP and MVDS can be used to demonstrate different AAR mission scenarios and to test complex docking algorithms. For example, the Space Systems Laboratory has plans to use the integrated docking system (SPHERES, UDP and MVDS) to assemble a modular telescope in a ground-based laboratory environment. Also, the integrated system will be used to test algorithms for autonomous docking with a freely tumbling target [32]. These are the type of demonstrations that will propel the AAR technology to the next level of maturity, and will aid in the exploration of space.

Appendix A. Engineering Drawings of the Universal Docking Port

DESCRIPTION	CURRENT REV	CURRENT QTY	Manufacturer	Manufacturer #
DISK	Rev 2	2	MIT-SSL	-
LANCE	Rev 3	1	MIT-SSL	-
MOTOR MOUNT	Rev 2	1	MIT-SSL	-
MOTOR SHAFT	Rev 4	1	MIT-SSL	-
PIN	Rev 5	1	MIT-SSL	-
SPACER	Rev 3	1	MIT-SSL	-
FRONT PLATE-CORE	Rev 3	1	MIT-SSL	-
FRONT PLATE-OUTER RING	Rev 2	1	MIT-SSL	-
BACK PLATE	Rev 6	1	MIT-SSL	-
Motor	-	1	SANYO NA4S SA43A	NA4S SA43A
STAND-OFFS	-	4	Digikey	-
THRUST BEARING	-	3	Torrington NTA-411	NTA-411
ELECTROMAGNETIC WIRE, VENDOR = ARCOR	-	1	ARCOR 28 AWG Magnet Wire	2700MG28
PIN SENSOR	-	-	Panasonic CNZ1120 (ON112)	CNZ1120 (ON112)
SENSOR WIRE, FOUR COLORS: RED/YELLOW/BROWN/BLACK	-	1		

Figure A-5-1: Bill of Materials (BOM) for the Universal Docking Port.

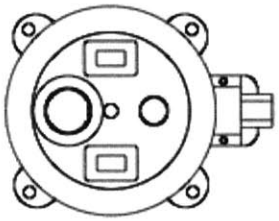

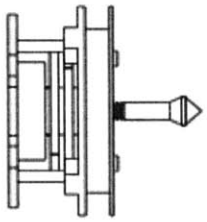

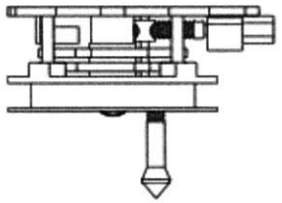

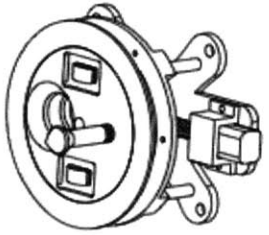

		UNLESS OTHERWISE SPECIFIED:		NAME	DATE
		DIMENSIONS ARE IN INCHES TOLERANCES: FRACTIONAL ± ANGULAR: MACH ± BEND ± TWO PLACE DECIMAL ± THREE PLACE DECIMAL ±	DRAWN	LPR	1/16/05
			CHECKED		
			ENG APPR.		
			MFG APPR.		
		INTERPRET GEOMETRIC TOLERANCING PER:	Q.A.		
		MATERIAL: Steel and Aluminum	COMMENTS:		
NEXT ASSY	USED ON	FINISH: NONE			
APPLICATION		DO NOT SCALE DRAWING			

PROPRIETARY AND CONFIDENTIAL

THE INFORMATION CONTAINED IN THIS DRAWING IS THE SOLE PROPERTY OF MIT-SPACE SYSTEMS LABORATORY. ANY REPRODUCTION IN PART OR AS A WHOLE WITHOUT THE WRITTEN PERMISSION OF MIT-SPACE SYSTEMS LABORATORY IS PROHIBITED.

SWARM - MIT

TITLE:
Interface Assembly

ENGINEER:
LENNON RODGERS

REV
3

SCALE: 1:2 | WEIGHT: | SHEET 1 OF 1

5 4 3 2 1

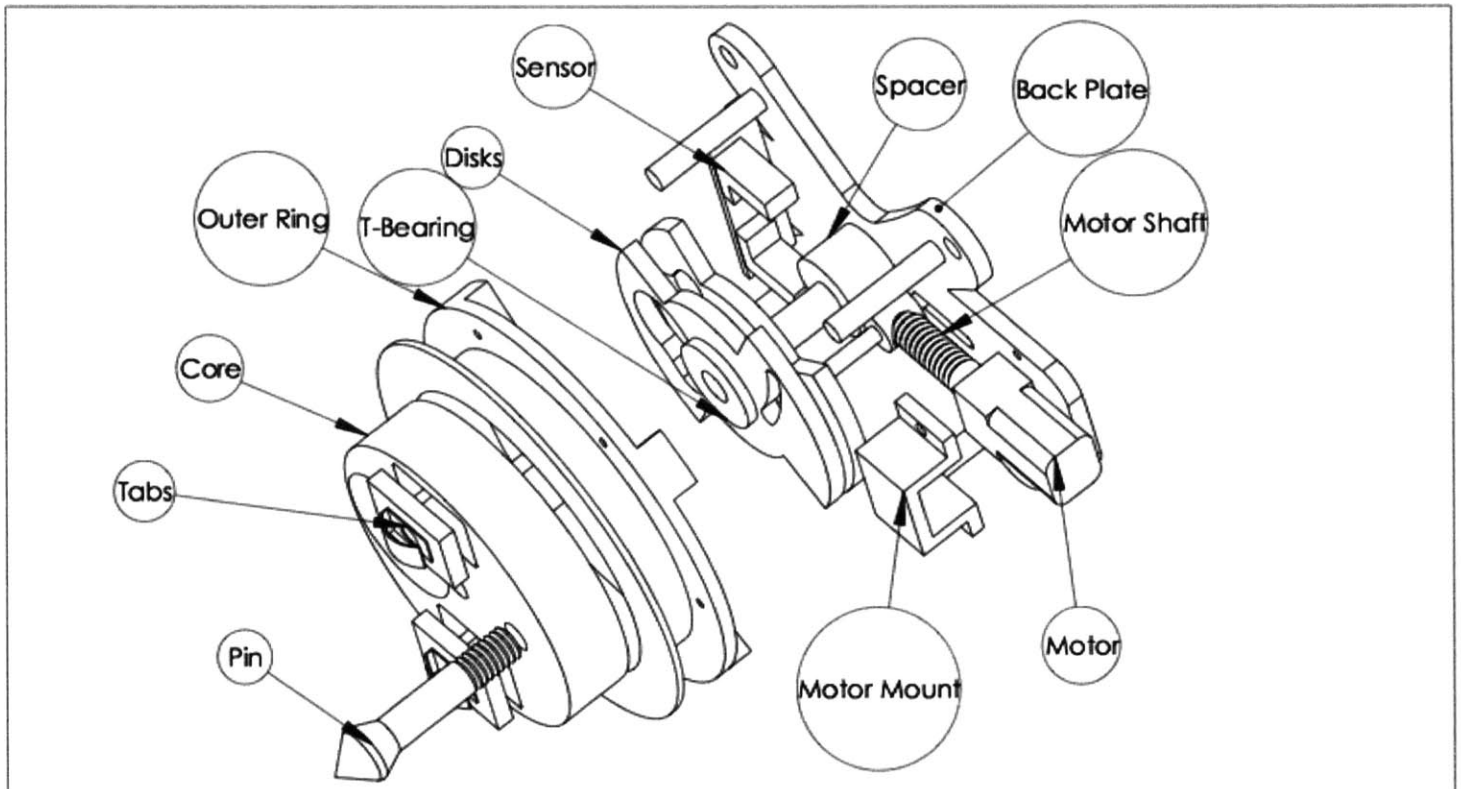

		UNLESS OTHERWISE SPECIFIED:		NAME	DATE
		DIMENSIONS ARE IN INCHES TOLERANCES: FRACTIONAL ± ANGULAR: MACH ± BEND ± TWO PLACE DECIMAL ± THREE PLACE DECIMAL ±	DRAWN	LPR	1/16/05
			CHECKED		
			ENG APPR.		
			MFG APPR.		
		INTERPRET GEOMETRIC TOLERANCING PER:	Q.A.		
		MATERIAL: Steel	COMMENTS:		
NEXT ASSY	USED ON	FINISH: NONE			
APPLICATION		DO NOT SCALE DRAWING			

SWARM - MIT

TITLE: Exploded Assembly

ENGINEER: LENNON RODGERS

REV 1

SCALE: 1:2 | WEIGHT: | SHEET 1 OF 1

5 4 3 2 1

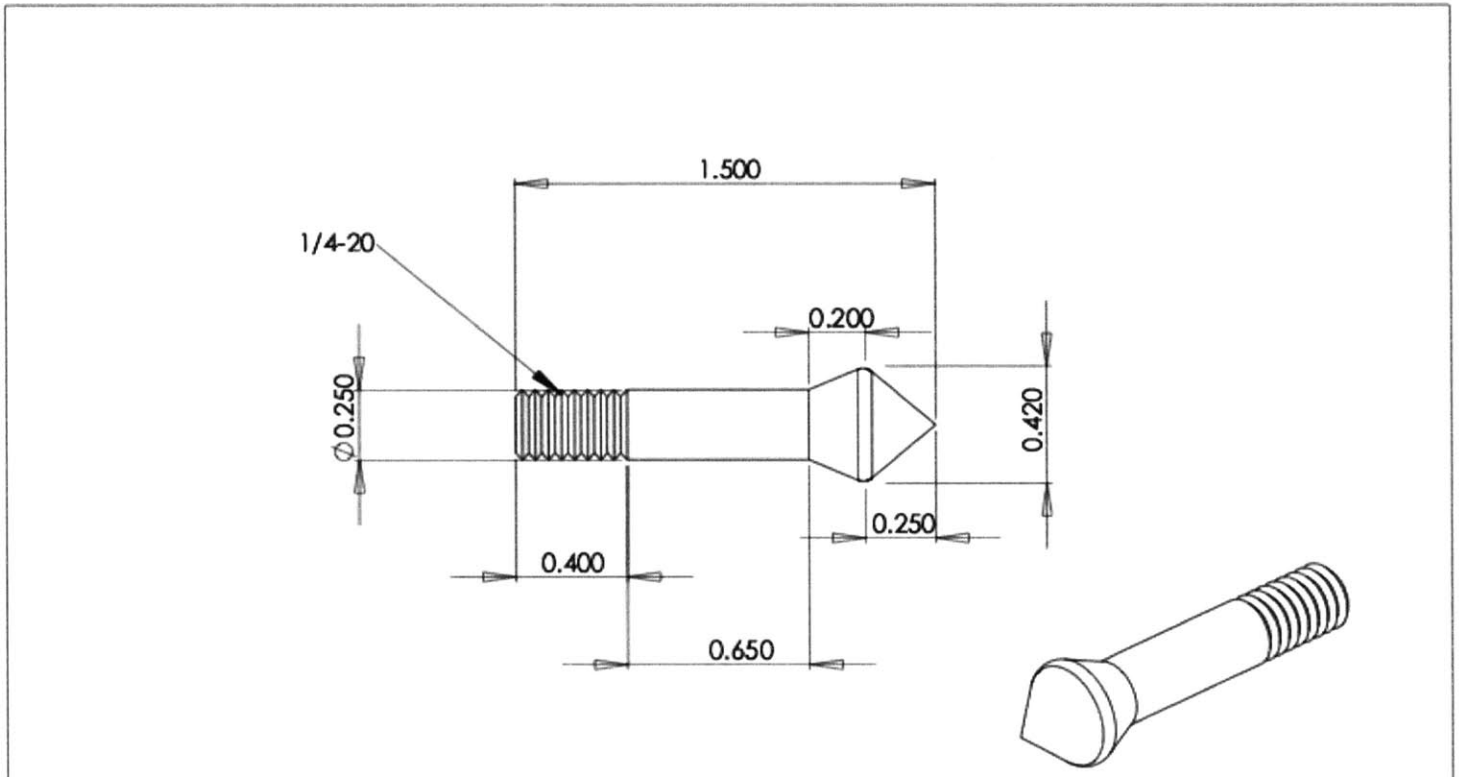

		UNLESS OTHERWISE SPECIFIED:		NAME	DATE
		DIMENSIONS ARE IN INCHES TOLERANCES: FRACTIONAL ± ANGULAR: MACH ± BEND ± TWO PLACE DECIMAL ± THREE PLACE DECIMAL ±	DRAWN	LPR	1/16/05
			CHECKED		
			ENG APPR.		
			MFG APPR.		
		INTERPRET GEOMETRIC TOLERANCING PER:	Q.A.		
		MATERIAL: Steel	COMMENTS:		
NEXT ASSY	USED ON	FINISH: NONE			
APPLICATION		DO NOT SCALE DRAWING			

SWARM - MIT

TITLE:
Lance

ENGINEER:
LENNON RODGERS

REV
3

SCALE: 2:1 | WEIGHT: | SHEET 1 OF 1

5 4 3 2 1

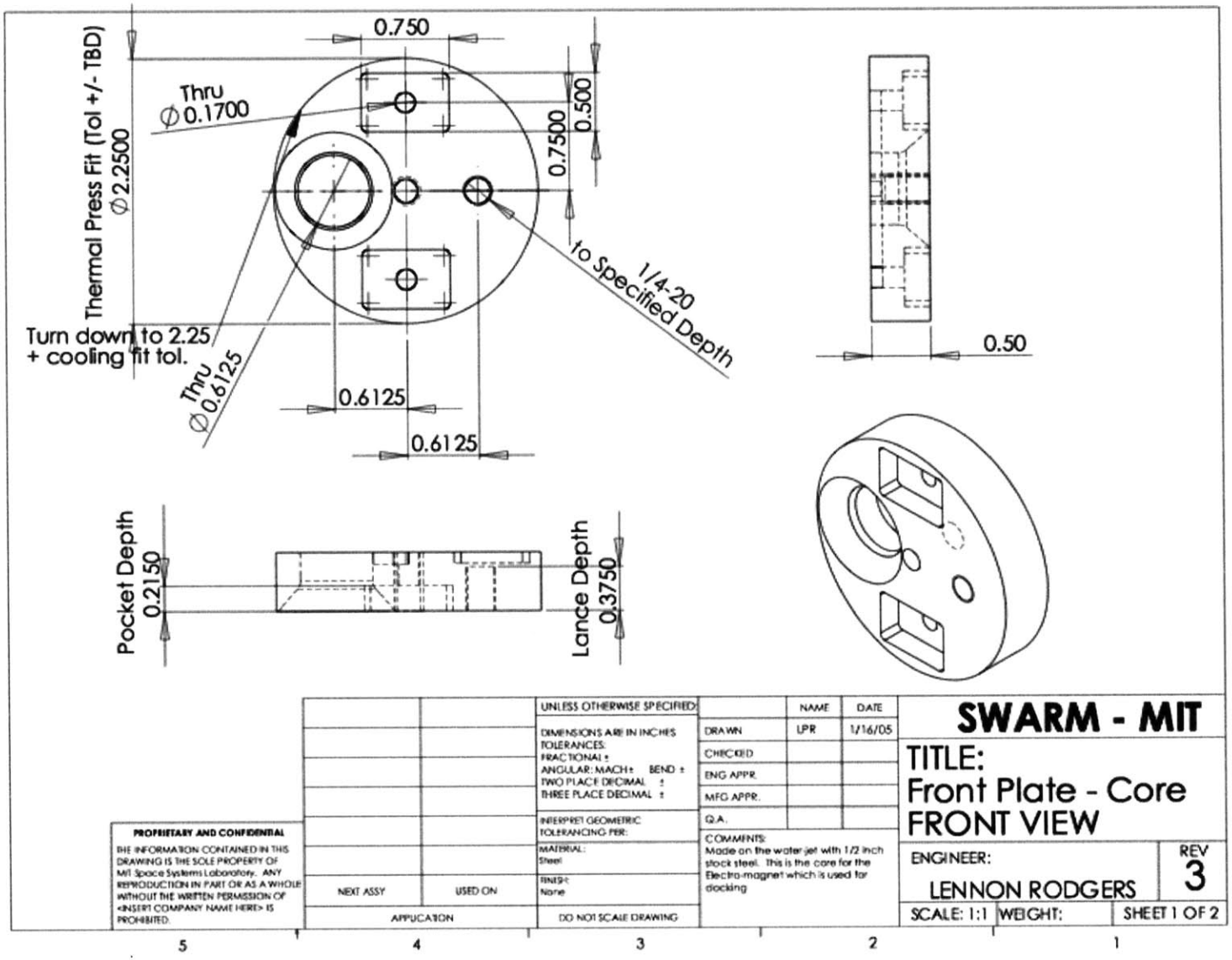
0.750
Thru
Ø 0.1700
0.7500
0.500
Thermal Press Fit (Tol +/- TBD)
Ø 2.2500
1/4-20
to Specified Depth
Turn down to 2.25
+ cooling fit tol.
Thru
Ø 0.6125
0.6125
0.6125
0.50
Pocket Depth
0.2150
Lance Depth
0.3750
UNLESS OTHERWISE SPECIFIED:
DIMENSIONS ARE IN INCHES
TOLERANCES:
FRACTIONAL ±
ANGULAR: MACH ± BEND ±
TWO PLACE DECIMAL ±
THREE PLACE DECIMAL ±
INTERPRET GEOMETRIC TOLERANCING PER:
MATERIAL: Steel
FINISH: None
DO NOT SCALE DRAWING
NEXT ASSY
USED ON
APPLICATION
NAME
DATE
DRAWN
LPR
1/16/05
CHECKED
ENG APPR.
MFG APPR.
Q.A.
COMMENTS:
Made on the water jet with 1/2 inch stock steel. This is the core for the Electro-magnet which is used for docking
PROPRIETARY AND CONFIDENTIAL
THE INFORMATION CONTAINED IN THIS DRAWING IS THE SOLE PROPERTY OF MIT Space Systems Laboratory. ANY REPRODUCTION IN PART OR AS A WHOLE WITHOUT THE WRITTEN PERMISSION OF <INSERT COMPANY NAME HERE> IS PROHIBITED.
SWARM - MIT
TITLE:
Front Plate - Core
FRONT VIEW
ENGINEER:
LENNON RODGERS
REV
3
SCALE: 1:1
WEIGHT:
SHEET 1 OF 2
5
4
3
2
1

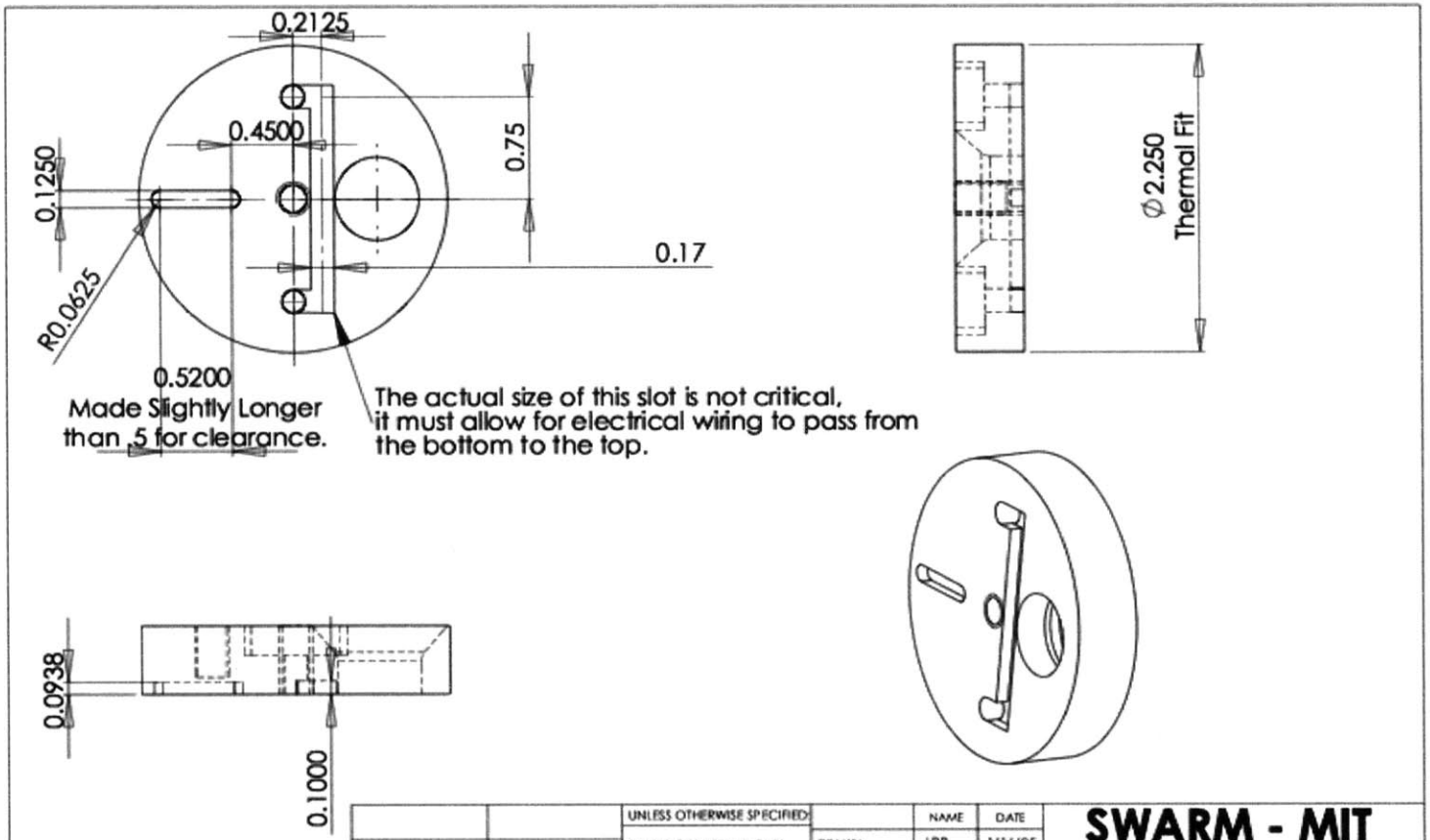

		UNLESS OTHERWISE SPECIFIED:		NAME	DATE
		DIMENSIONS ARE IN INCHES TOLERANCES: FRACTIONAL ± ANGULAR: MACH ± BEND ± TWO PLACE DECIMAL ± THREE PLACE DECIMAL ±	DRAWN	LPR	1/16/05
			CHECKED		
			ENG APPR.		
			MFG APPR.		
		INTERPRET GEOMETRIC TOLERANCING PER:	Q.A.		
		MATERIAL: Steel	COMMENTS: Made on the water jet with 1/2 inch stock steel. This is the core for the Electro-magnet which is used for docking		
NEXT ASSY	USED ON	FINISH: None			
APPLICATION		DO NOT SCALE DRAWING			

SWARM - MIT

TITLE:
Front Plate - Core
BACK VIEW

ENGINEER: LENNON RODGERS

REV 2

SCALE: 1:1 | WEIGHT: | SHEET 2 OF 2

5 4 3 2 1

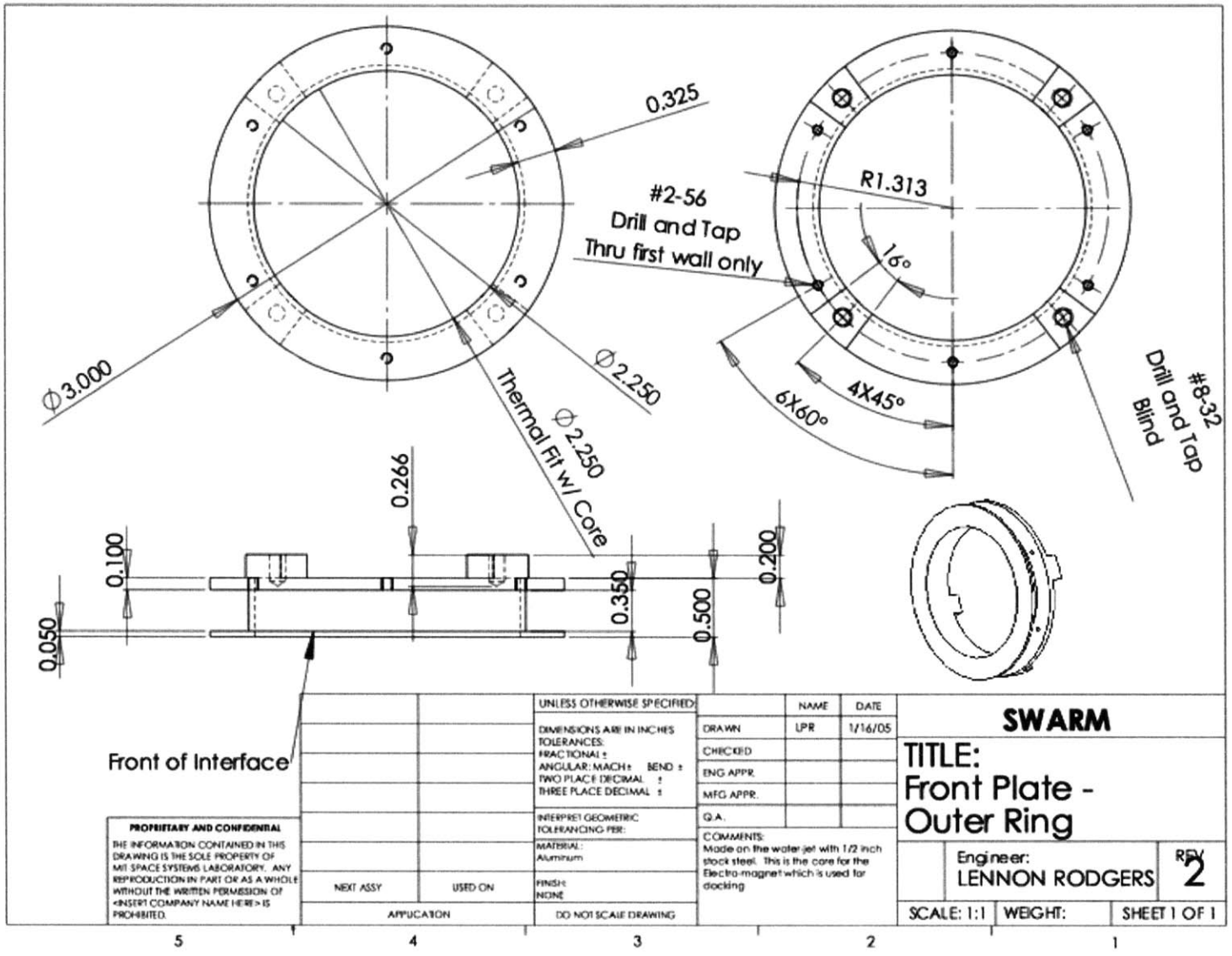
0.325
#2-56
Drill and Tap
Thru first wall only
R1.313
16°
Ø3.000
Ø2.250
Thermal Fit w/ Core
Ø2.250
6X60°
4X45°
#8-32
Drill and Tap
Blind
0.266
0.100
0.050
0.350
0.500
0.200
Front of Interface
UNLESS OTHERWISE SPECIFIED:
DIMENSIONS ARE IN INCHES
TOLERANCES:
FRACTIONAL ±
ANGULAR: MACH ± BEND ±
TWO PLACE DECIMAL ±
THREE PLACE DECIMAL ±
INTERPRET GEOMETRIC TOLERANCING PER:
MATERIAL: Aluminum
FINISH: NONE
DO NOT SCALE DRAWING
NAME
DATE
DRAWN LPR 1/16/05
CHECKED
ENG APPR.
MFG APPR.
Q.A.
COMMENTS:
Made on the water jet with 1/2 inch stock steel. This is the core for the Electro-magnet which is used for docking
NEXT ASSY
USED ON
APPLICATION
PROPRIETARY AND CONFIDENTIAL
THE INFORMATION CONTAINED IN THIS DRAWING IS THE SOLE PROPERTY OF MIT SPACE SYSTEMS LABORATORY. ANY REPRODUCTION IN PART OR AS A WHOLE WITHOUT THE WRITTEN PERMISSION OF <INSERT COMPANY NAME HERE> IS PROHIBITED.
SWARM
TITLE:
Front Plate -
Outer Ring
Engineer:
LENNON RODGERS
REV
2
SCALE: 1:1
WEIGHT:
SHEET 1 OF 1
5
4
3
2
1

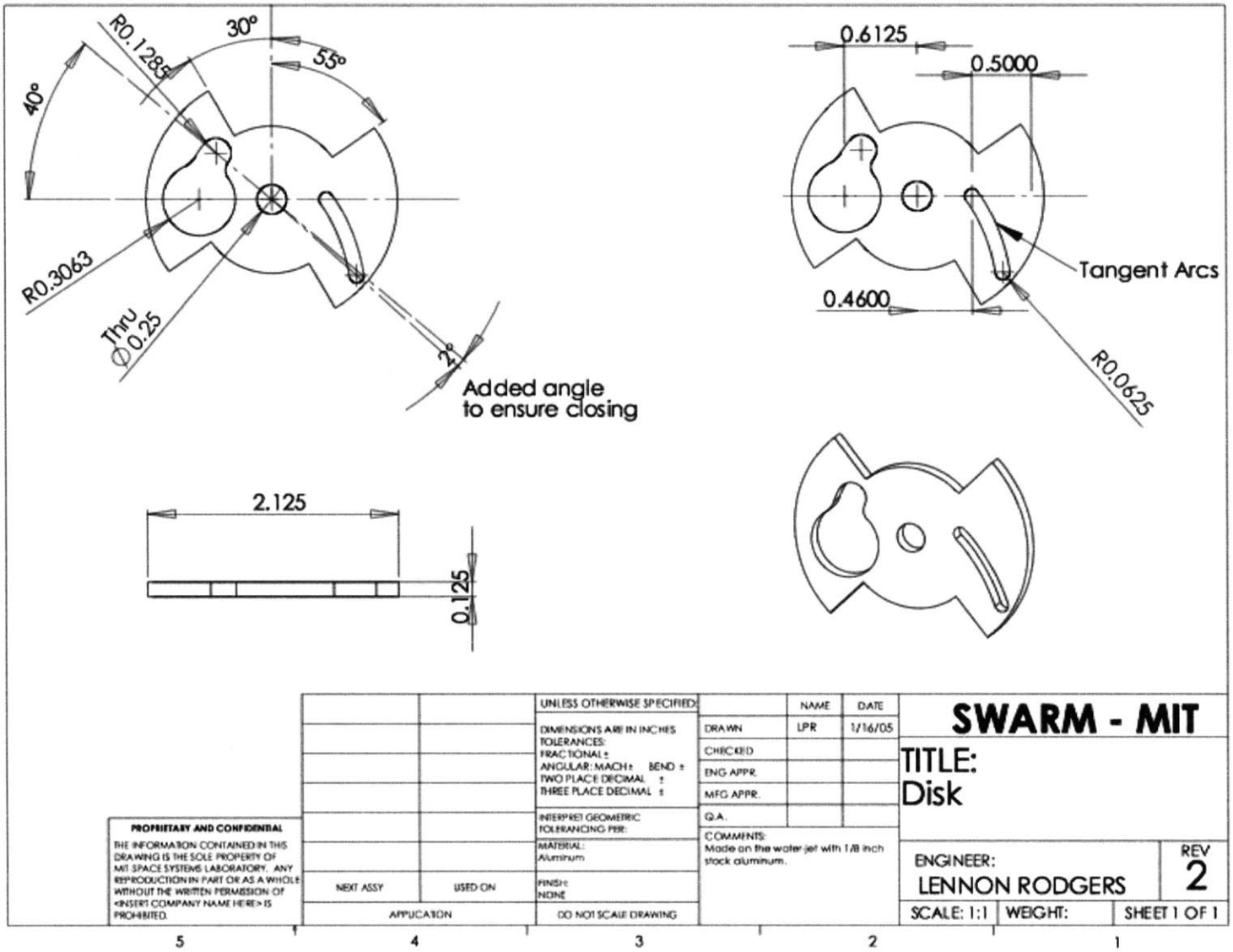
R0.1285
30°
55°
40°
R0.3063
Thru
Ø0.25
2°
Added angle
to ensure closing
0.6125
0.5000
Tangent Arcs
0.4600
R0.0625
2.125
0.125
UNLESS OTHERWISE SPECIFIED:
DIMENSIONS ARE IN INCHES
TOLERANCES:
FRACTIONAL ±
ANGULAR: MACH ± BEND ±
TWO PLACE DECIMAL ±
THREE PLACE DECIMAL ±
INTERPRET GEOMETRIC TOLERANCING PER:
MATERIAL:
Aluminum
FINISH:
NONE
DO NOT SCALE DRAWING
NEXT ASSY
USED ON
APPLICATION
NAME
DATE
DRAWN
LPR
1/16/05
CHECKED
ENG APPR.
MFG APPR.
Q.A.
COMMENTS:
Made on the water jet with 1/8 inch stock aluminum.
PROPRIETARY AND CONFIDENTIAL
THE INFORMATION CONTAINED IN THIS DRAWING IS THE SOLE PROPERTY OF MIT SPACE SYSTEMS LABORATORY. ANY REPRODUCTION IN PART OR AS A WHOLE WITHOUT THE WRITTEN PERMISSION OF <INSERT COMPANY NAME HERE> IS PROHIBITED.
SWARM - MIT
TITLE:
Disk
ENGINEER:
LENNON RODGERS
REV
2
SCALE: 1:1
WEIGHT:
SHEET 1 OF 1
5
4
3
2
1

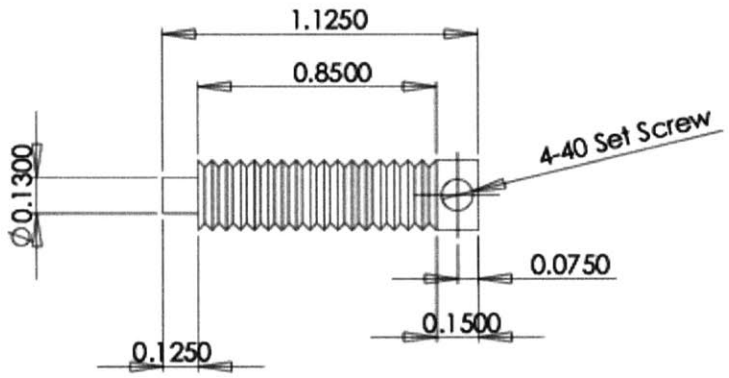

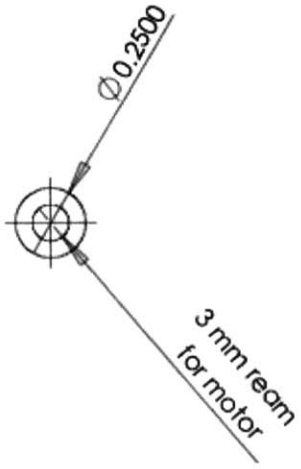

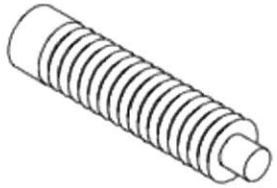

Manufacturing Note:
1. Turn down to .25 OD, length ~1.25
2. Create shoulder
3. Creat threads
4. Cut off with length 1.125 (as specified)
5. Put reamed hole in end

		UNLESS OTHERWISE SPECIFIED:		NAME	DATE
		DIMENSIONS ARE IN INCHES TOLERANCES: FRACTIONAL ± ANGULAR: MACH ± BEND ± TWO PLACE DECIMAL ± THREE PLACE DECIMAL ±	DRAWN	LPR	1/16/05
			CHECKED		
			ENG APPR.		
			MFG APPR.		
		INTERPRET GEOMETRIC TOLERANCING PER:	Q.A.		
		MATERIAL: Steel	COMMENTS:		
NEXT ASSY	USED ON	FINISH: NONE			
APPLICATION		DO NOT SCALE DRAWING			

SWARM - MIT

TITLE:
Motor Shaft

ENGINEER: LENNON RODGERS

REV 4

SCALE: 2:1 | WEIGHT: | SHEET 1 OF 1

5 4 3 2 1

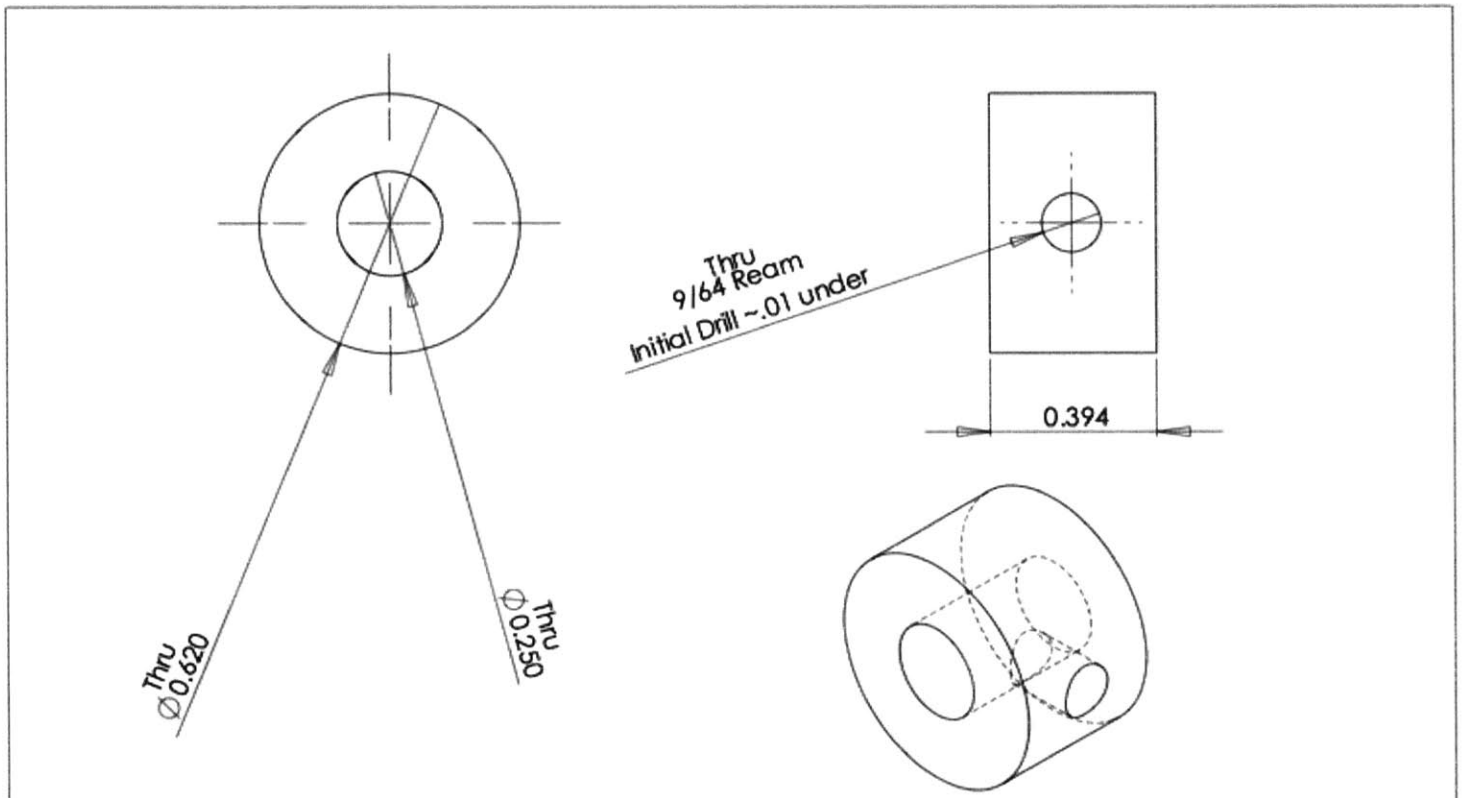

		UNLESS OTHERWISE SPECIFIED:		NAME	DATE
		DIMENSIONS ARE IN INCHES TOLERANCES: FRACTIONAL ± ANGULAR: MACH ± BEND ± TWO PLACE DECIMAL ± THREE PLACE DECIMAL ±	DRAWN	LPR	1/16/05
			CHECKED		
			ENG APPR.		
			MFG APPR.		
		INTERPRET GEOMETRIC TOLERANCING PER:	Q.A.		
		MATERIAL: Aluminum	COMMENTS:		
NEXT ASSY	USED ON	FINISH: NONE			
APPLICATION		DO NOT SCALE DRAWING			

SWARM - MIT

TITLE:
Spacer

ENGINEER:
LENNON RODGERS

REV
3

SCALE: 3:1 | WEIGHT: | SHEET 1 OF 1

5 4 3 2 1

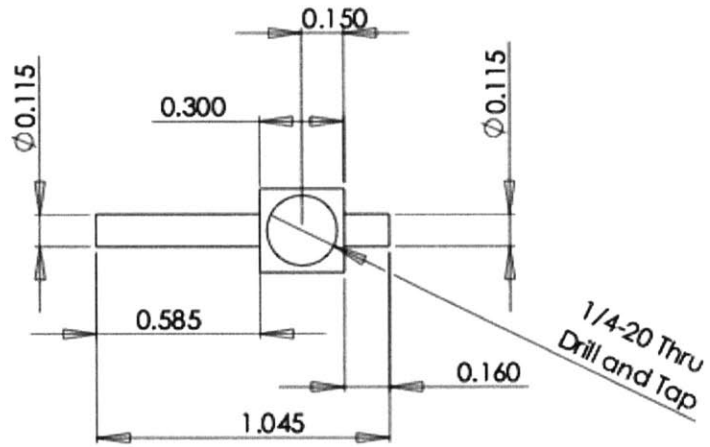

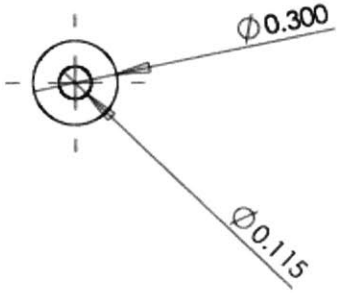

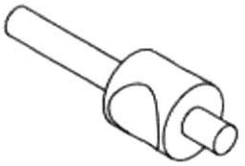

		UNLESS OTHERWISE SPECIFIED:		NAME	DATE
		DIMENSIONS ARE IN INCHES TOLERANCES: FRACTIONAL ± ANGULAR: MACH ± BEND ± TWO PLACE DECIMAL ± THREE PLACE DECIMAL ±	DRAWN	LPR	1/16/05
			CHECKED		
			ENG APPR.		
			MFG APPR.		
		INTERPRET GEOMETRIC TOLERANCING PER:	Q.A.		
		MATERIAL: Steel	COMMENTS:		
NEXT ASSY	USED ON	FINISH: NONE			
APPLICATION		DO NOT SCALE DRAWING			

SWARM - MIT

TITLE:
Pin

ENGINEER:
LENNON RODGERS

REV
5

SCALE: 2:1 | WEIGHT: | SHEET 1 OF 1

5 4 3 2 1

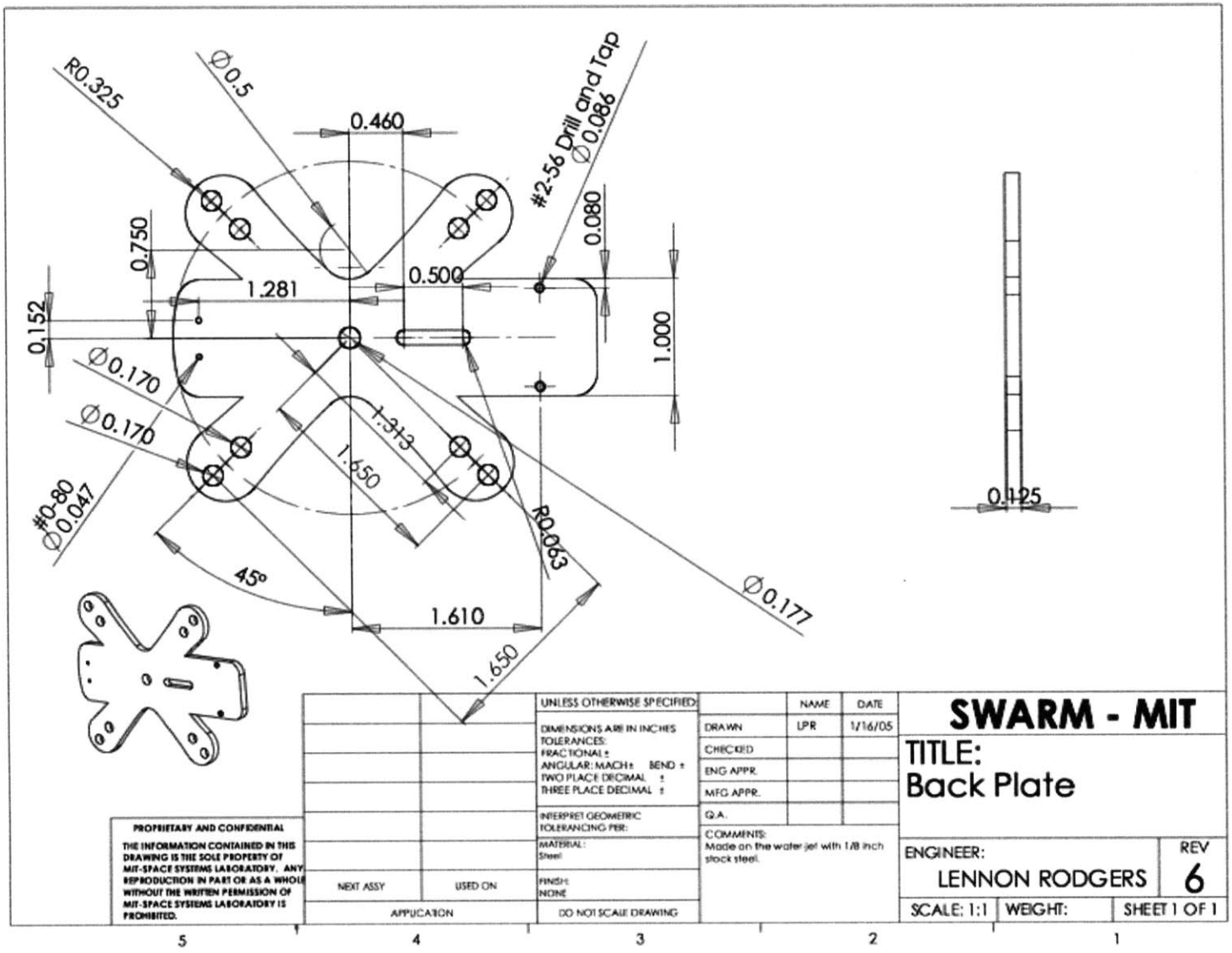
R0.325
Ø0.5
0.460
#2-56 Drill and Tap
Ø0.086
0.080
0.750
1.281
0.500
0.152
1.000
Ø0.170
Ø0.170
1.313
1.650
#0-80
Ø0.047
R0.063
45°
Ø0.177
1.610
1.650
0.125
UNLESS OTHERWISE SPECIFIED:
DIMENSIONS ARE IN INCHES
TOLERANCES:
FRACTIONAL ±
ANGULAR: MACH ± BEND ±
TWO PLACE DECIMAL ±
THREE PLACE DECIMAL ±
INTERPRET GEOMETRIC TOLERANCING PER:
MATERIAL: Steel
FINISH: NONE
DO NOT SCALE DRAWING
NAME
DATE
DRAWN
UPR
1/16/05
CHECKED
ENG APPR.
MFG APPR.
Q.A.
COMMENTS: Made on the water jet with 1/8 inch stock steel.
NEXT ASSY
USED ON
APPLICATION
PROPRIETARY AND CONFIDENTIAL
THE INFORMATION CONTAINED IN THIS DRAWING IS THE SOLE PROPERTY OF MIT-SPACE SYSTEMS LABORATORY. ANY REPRODUCTION IN PART OR AS A WHOLE WITHOUT THE WRITTEN PERMISSION OF MIT-SPACE SYSTEMS LABORATORY IS PROHIBITED.
SWARM - MIT
TITLE:
Back Plate
ENGINEER:
LENNON RODGERS
REV
6
SCALE: 1:1
WEIGHT:
SHEET 1 OF 1
5
4
3
2
1

Appendix B. The "Rocket Equation"

Newton's Second Law states:

$$F = \frac{d(M \cdot v)}{dt} \qquad \text{B-1}$$

where F is the sum of all external forces acting on the tug and v is the velocity of the tug. The variable M is defined as:

$$M = m_d + m_{pt} \qquad \text{B-2}$$

where m_d and m_{pt} are the masses of the tug and propellant, respectively.

Thus Equation B-1 states that all external forces acting on the tug equals the change in momentum of the tug. Since there are no external forces acting on the tug, Equation B-1 becomes:

$$\frac{d(M \cdot v)}{dt} = 0 \qquad \text{B-3}$$

which can be expanded and written as the final minus the initial momentum:

$$d(m \cdot v)_{detector} = \left[M \cdot (v + dv) + (v - v_e) \cdot dm\right] - (M + dm) \cdot v = 0 \qquad \text{B-4}$$

where v_e and dm are the exit velocity and differential change of the propellant mass, respectively, and dv is the differential change in the velocity of the tug. Multiplying out Equation B-4, and recognizing that $dm = -dM$, yields:

$$M \cdot dv = -v_e \cdot dM \qquad \text{B-5}$$

Integrating both sides results in:

$$-\frac{1}{v_e} \cdot \int_{vi}^{v_f} dv = \int_{m_i}^{m_f} \frac{1}{M} dM \qquad \text{B-6}$$

Integration yields a relationship for "Delta V:"

$$\Delta V = v_f - v_i = v_e \cdot \ln(1 + \frac{m_{pt}}{m_d}) \qquad \text{B-7}$$

This can be re-arranged to solve for the propellant mass:

$$m_{pt} = m_d \cdot \left(e^{\frac{\Delta V_{total}}{I_{sp} \cdot g}} - 1 \right) \qquad \text{B-8}$$

where

$$I_{sp} = \frac{v_e}{g} \qquad \text{B-9}$$

and where g is the gravitational constant at sea-level. Equation B-8 is often referred to as the "Rocket Equation." The Rocket Equation yields the mass of the propellant required for a given Delta V maneuver.

Appendix C. The Attitude Matrix and Quaternions

The attitude matrix, A_q, is used to convert vectors between coordinate frames [33]. Thus, if $\boldsymbol{X_T}$ is a vector written in the chase coordinate frame, the same vector expressed in the target coordinate frame, $\boldsymbol{X_C}$, can be written as:

$$\boldsymbol{X_c = A_q X_T} \tag{5-3}$$

Also, the reverse can be done:

$$\boldsymbol{X_T = A_q^t X_c} \tag{5-4}$$

where $\boldsymbol{A_q^t}$ is the transpose of $\boldsymbol{A_q}$. The matrix $\boldsymbol{A_q}$ can be written as:

$$\boldsymbol{A_q} = \begin{bmatrix} q_1^2 - q_2^2 - q_3^2 + q_4^2 & 2\cdot(q_1\cdot q_2 + q_3\cdot q_4) & 2\cdot(q_1\cdot q_3 - q_2\cdot q_4) \\ 2\cdot(q_1\cdot q_2 - q_3\cdot q_4) & -q_1^2 + q_2^2 - q_3^2 + q_4^2 & 2\cdot(q_2\cdot q_3 + q_1\cdot q_4) \\ 2\cdot(q_1\cdot q_3 + q_2\cdot q_4) & 2\cdot(q_2\cdot q_3 - q_1\cdot q_4) & -q_1^2 - q_2^2 + q_3^2 q_4^2 \end{bmatrix} \tag{5-5}$$

where q_i are the quaternions of the chase vehicle, which will be discussed below.

The matrix A_q has at least one eigenvector with an eigenvalue equal to one. That is, there exists a vector $\hat{\boldsymbol{e}}$ such that:

$$\boldsymbol{A_q \hat{e} = \hat{e}} \tag{5-6}$$

This implies that $\hat{\boldsymbol{e}}$ is unchanged by the rotation applied by the attitude matrix. The existence of $\hat{\boldsymbol{e}}$ demonstrates Euler's theorem: "The most general displacement of a rigid body with one point fixed is a rotation about some axis." The axis of rotation is specified by $\hat{\boldsymbol{e}}$, and the rotation about that axis is specified by a scalar, $\boldsymbol{\theta}$ (Figure C-1).

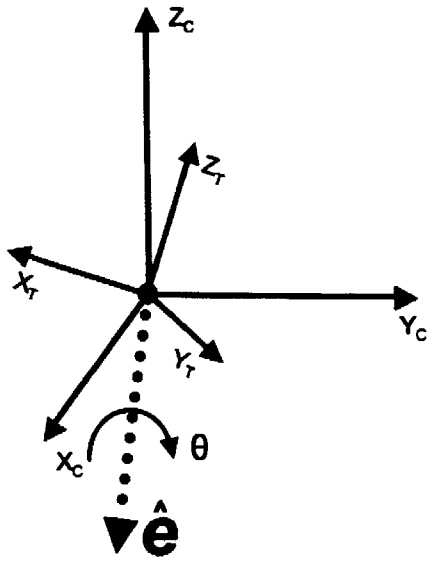

Figure C-1: The most general way to specify a rotation of a body in frame T relative to a reference frame C.

A quaternion vector, $\boldsymbol{q}$, is a superior way to represent the orientation since it does not have singularities as do the Euler angles. The quaternion vector is defined as:

$$\boldsymbol{q} \equiv \begin{bmatrix} e_x \sin(\frac{\theta}{2}) \\ e_y \sin(\frac{\theta}{2}) \\ e_z \sin(\frac{\theta}{2}) \\ \cos(\frac{\theta}{2}) \end{bmatrix} \qquad 5\text{-}7$$

where e_j is the scalar component of the eigenvector ($\hat{\boldsymbol{e}}$) along the j-axis.

Appendix D. Bibliography

[1] Bartlett, R. O., "NASA standard Multimission Modular Spacecraft for future space exploration," American Astronautical Society and Deutsche Gesellschaft fuer Luft- und Raumfahrt, Goddard Memorial Symposium, 16th, Washington, D.C., Mar. 8-10, 1978, AAS.

[2] "Computers in Spaceflight: The NASA Experience" http://www.hq.nasa.gov/office/pao/History/computers/Ch6-4.html

[3] Moynahan and Touhy, "Development of a Modular On-orbit Serviceable Satellite Architecture," DARPA research grant, 2001.

[4] AeroAstro website: www.aeroastro.com

[5] Nakasuka, Nakamura, Eishima and Kobayashi, "Panel Extension Satellite (PETSAT) - Low Cost Multi-Purpose Micro-satellite Consisting of Modular, Functional and Plug-in Panels," Submitted to IAC, 2004.

[6] Kong, E. M. C., Otero, A. S., Nolet S., Berkovitz, D. S., Miller, D. W., and Sell, S. W., "SPHERES as a Formation Flight Algorithm Development and Validation Testbed: Current Progress and Beyond," Proc. of the 2nd International Symposium on Formation Flying Missions and Technologies, Washington DC, September 2004.

[7] Massachusetts Institute of Technology, "SWARM Design Document, Revision 3.2." http://spacestation.mit.edu/SPHEREs/swarm/documents.html

[8] Blueradios website: http://www.blueradios.com/

[9] The official Bluetooth website: http://www.bluetooth.com/

[10] Enright, Jilla, Miller, "Modularity and Spacecraft Cost," Journal of Reducing Space Mission Cost, 1998.

[11] DARPA's Large Aperture Space Surveillance - Optical (LASO) program: http://www.darpa.mil/baa/baa04-36.htm

[12] Kwon, Daniel, "Electromagnetic Formation Flight of Satellite Arrays," Masters Thesis, Massachusetts Institute of Technology, Department of Aeronautics and Astronautics, January 2005.

[13] Larson, Wiley J. and Wertz, James R., "Space Mission Analysis and Design," Third Edition, 2003.

[14] Ahsun, Umair, Miller, David W, "Dynamics and Control of Electromagnetic Satellite Formations," American Control Conference, 2006.

[15] Meyer, P.H., "Gemini/Agena Docking Mechanism", First Aerospace Mechanisms Symposium, University of Santa Clara, Santa Clara, California, May 19-20, 1966.

[16] Fehse, Wigbert, "Automated Rendezvous and Docking of Spacecraft," Cambridge Aerospace Series, 2003.

[17] Bloom, K.A. and Campbell, G.E., "The Apollo Docking System", Proceedings of the Fifth Aerospace Mechanisms Symposium, NASA-GSFC, Greenbelt, Maryland, June 15-16, 1970.

[18] Schliesing, J.A., "Dynamic Analysis of Apollo-Salyut/Soyuz Docking", Seventh Aerospace Mechanisms Symposium, NASA-JSC, Houston, Texas, September 7-8, 1972.

[19] Swan, W.L., Jr., "Apollo-Soyuz Test Project Docking System", Tenth Aerospace Mechanisms Symposium, NASA-JPL, Pasadena, California, April 22-23, 1976.

[20] Shuttle Press Kit for STS 71, "Orbiter Docking Mechanism," Chapter 2.23: http://www.shuttlepresskit.com/scom/223.pdf

[21] McLaughlin, Richard J. and Warr William H., "The Common Berthing Mechanism (CBM) for International Space Station," Society of Automotive Engineers, 2001, 2001-01-2435.

[22] DARPA's Orbital Express Website: http://www.darpa.mil/tto/programs/oe.htm

[23] Lewis, J.L. and Carroll, M.B., "Prototype Low Impact Docking System", Proceedings of the AIAA International Space Station Service Vehicle Conference, Houston, Texas, April 25-28, 1999.

[24] Tchoryk, Hays, Pavlich, Ritter, Wassick, Nardell, Sypitkowski, "Autonomous Satellite Docking System," AJAA Space 2001 Conference, Albuquerque, NM, August 28 - 30, 2001.

[25] Schneider, W.C., Nagy, K., and Schliesing, J.A., "Magnetic Docking Aid for Orbiter to ISS Docking", 30th Aerospace Mechanisms Symposium, NASA-HQ, Hampton, Virginia, May 15-17, 1996.

[26] Tietz, J.C., "Development of an Autonomous Video Rendezvous and Docking System," Martin Marietta Corporation, Contract No. NAS8-34679, Phase Three, January 1984.

[27] Howard, R.T. and Dabney, R.W., "Development of a Video-Based Automatic Rendezvous and Docking System," SME Robotics and Space Manufacturing Conference, January 1988.

[28] Howard, R., Bryan, T., Book, M. and Jackson, J, "Active Sensor System for Automatic Rendezvous and Docking", Proceedings of SPIE Laser Radar Technology and Applications II, pp. 106-115, 1997.

[29] Wolfe, William, Mathis, Donald, Sklair, Cheryl, Magee, Michael, "The Perspective View of Three Points," IEEE Transactions of Pattern Analysis and Machine Intelligence, Vol. 13, No.1, January 1991.

[30] Hilstad, Mark "A Multi-Vehicle Testbed and Interface Framework for the Development and Verification of Separated Spacecraft Control Algorithms." Masters Thesis, Massachusetts Institute of Technology, Department of Aeronautics and Astronautics, June 2002.

[31] Nolet, Simon, "Autonomous Docking Algorithm Development and Experimentation using the SPHERES Testbed," SPIE, April 2004.

[32] Nolet, Simon, "Design of an Algorithm for Autonomous Docking With a Freely Tumbling Target," SPIE, March 05, 2005.

[33] Wertz, James R., "Spacecraft Attitude Determination and Control," volume 73 of Astrophysics and Space Science Library, 1978.

[34] Syromiatnikov, V.S., "Docking of Spacecrafts and Modules in the Mir Orbital Station Program", in "Mir-1 Space Station: A Technical Overview, Edition 2", ed. Gary A. Girain, NPO Energia Ltd, 1995.

[35] Syromyatnikov, V.S., "Docking Systems of Androgynous and Peripheral Type", Seventh Aerospace Mechanisms Symposium, NASA-JSC, Houston, Texas, September 7-8, 1972.

[36] Daniell, R.G. and Sachdev, S.S., "The Design and Development of an End Effector for the Shuttle Remote Manipulator System", 16th Aerospace Mechanisms Symposium, NASA-KSC, Kennedy Space Center, Florida, May 13-14, 1982.

[37] Dorland, W.D., "Dynamic Testing of Docking System Hardware", Seventh Aerospace Mechanisms Symposium, NASA-JSC, Houston, Texas, September 7-8, 1972.

[38] Gampe, F., Priesett, K., and Bentall, R.H., "A Modular Docking Mechanism for In-Orbit Assembly and Spacecraft Servicing", 19th Aerospace Mechanisms Symposium, NASA-ARC, Moffett Field, California, May 1-3, 1985.

[39] McLaughlin, R.J. and Warr, W.H., "The Common Berthing Mechanism (CBM) for International Space Station", Proceedings of the SAE International Conference on Environmental Systems, 2001.

[40] Gonzalez-Vallejo, J.J., Fehse, W., and Tobias, A., "A Multipurpose Model of Hermes-Columbus Docking Mechanism", 26th Aerospace Mechanisms Symposium, NASA-GSFC, Greenbelt, Maryland, May 13-15, 1992.

[41] Hays, A.B., et al., "Advancements in KC-135 Microgravity Testing of an Autonomous Satellite Docking System", Proceedings of SPIE Volume 5419 Spacecraft Platforms and Infrastructure, Bellingham, Washington, 2004.

[42] Hays, A.B., et al., "Advancements in the Design of an Autonomous Satellite Docking System", Proceedings of SPIE Volume 5419 Spacecraft Platforms and Infrastructure, Bellingham, Washington, 2004.

[43] Hirzinger, G. et al., "Advances in Orbital Robotics", Proceedings of the IEEE International Conference on Robotics and Automation, San Francisco, California, April, 2000.

[44] Illi, E., "Space Station Freedom Common Berthing Mechanism", 26th Aerospace Mechanisms Symposium, NASA-GSFC, Greenbelt, Maryland, May 13-15, 1992.

[45] Inaba, N. and Oda, M., "Autonomous Satellite Capture by a Space Robot", Proceedings of the IEEE International Conference on Robotics and Automation, San Francisco, California, April, 2000.

[46] International Space Station Structures and Mechanisms Training Manual, NASA-JSC Internal Document (ISS S&M TM 21002C).

[47] Jackson, S.W., and Gallo, F.G., "The Resupply Interface Mechanism RMS Compatibility Test", 24th Aerospace Mechanisms Symposium, NASA-KSC, Kennedy Space Center, Florida, April 18-20, 1990.

[48] Johnston, A.S. and Tyler, T.R., "Testing of the Automated Fluid Interface System", Proceedings of the 32nd Aerospace Mechanisms Symposium, NASA-KSC, Cocoa Beach, Florida, May 13-15, 1998.

[49] Jones, J.C., "Neuter Docking-Mechanism Study", Sixth Aerospace Mechanisms Symposium, NASA-ARC, Moffett Field, California, September 9-10, 1971.

[50] Langley, R.D., "The Apollo 14 Docking Anomaly", Proceedings of the Seventh Aerospace Mechanisms Symposium, NASA-JSC, Houston, Texas, September 7-8, 1972.

[51] Mandvi, A., "Umbilical Mechanisms Assembly for the International Space Station", 30th Aerospace Mechanisms Symposium, NASA-HQ, Hampton, Virginia, May 15-17, 1996.

[52] Milton, M.E. and Tyler, T.R., "Development and Testing of the Automated Fluid Interface System", Proceedings of the 27th Aerospace Mechanisms Symposium, NASA-ARC, Moffett Field, California , May 12-14, 1993.

[53] Oda, M., "Experiences and Lessons Learned from the ETS-VII Robot Satellite", Proceedings of the IEEE International Conference on Robotics and Automation, San Francisco, California, April, 2000.

[54] Oda, M., "Space Robot Experiments on NASDA's ETS-VII Satellite", Proceedings of the IEEE International Conference on Robotics and Automation, Detroit, Michigan, May, 1999.

[55] Oda, M., Kibe, K., and Yamagata, Y., "ETS-VII, Space Robot In-Orbit Experiment Satellite", Proceedings of the IEEE International Conference on Robotics and Automation, Minneapolis, Minnesota, April, 1996.

[56] Oda, M. et al., "ETS-7, A Rendezvous Docking and Space Robot Technology Experiment Satellite", Proceedings of SICE '95, Sapporo, Japan, July 26-28, 1995.

[57] Silverman, M.C., et al., "Staying Alive: A Docking Station for Autonomous Robot Recharging", Proceedings of the IEEE International Conference on Robotics and Automation, Washington, DC, May, 2002.

[58] Walker, B. and Vandersluis, R., "Design, Testing and Evaluation of Latching End Effector", 29th Aerospace Mechanisms Symposium, NASA-JSC, League City, Texas, May 17-19, 1995.

[59] Yoshida, K., Hashizume, K., and Abiko, S., "Zero Reaction Maneuver: Flight Validation with ETS-VII Space Robot and Extension to Kinematically Redundant Arm", Proceedings of the IEEE International Conference on Robotics and Automation, 2001.